Physical Mechanisms for the Emergence of Order in Biological Systems

Charlotte Strandkvist

A thesis presented for the degree of
Doctor of Philosophy

Supervised by:
Prof Buzz Baum and Dr Alexandre Kabla

University College London
2016

I, Charlotte Strandkvist, confirm that the work presented in this thesis is my own. Where information has been derived from other sources, I confirm that this has been indicated in the thesis.

Signed .....

Abstract

How biological order emerges in a robust manner during development is an important question, as the functionality of many tissues depends on the correct spatial arrangement of cells. In this thesis, I consider two examples of ordering, cell sorting and hexagonal packing.

In several developing tissues, cells of different type spontaneously self-assemble into domains that are homogenous with respect to cell type both in vitro and in vivo. Current models of sorting assume asymmetry in the physical properties of cell types - either in adhesion, cortical tension or motility. I present a minimal model demonstrating that segregation does not require such asymmetry, but can arise solely from cell motility when this is modelled as a dynamic quantity that changes in response to the composition of the local environment of a cell.

Over the course of pupal development, cells in the *Drosophila* notum rearrange to form a hexagonally packed tissue. How does the tissue transition from disorder to order in an effective and robust way? In particular, how do stochastic fluctuations in junction length contribute to the ordering process? I address these questions by analysing data from live-imaging of the notum using a custom software package I developed. I demonstrate that neighbour exchange events are a consequence of junction fluctuations, rather than being an explicitly regulated and stereotyped process, and I present a mathematical model for how such fluctuations are generated by the stochastic turnover of myosin. I quantify the frequency of neighbour exchange events in embryos with a reduction/overexpression of Myosin II activity and establish that actomyosin is not required for neighbour exchange. In fact, the frequency of neighbour exchange events is inversely proportional to Myosin II levels. The results suggest that the gradual increase in actomyosin during development drives a process akin to annealing that aids tissue ordering.

Contents

List of Figures **1**

1 Kinetics of Cell Sorting **4**

1.1 Introduction 4

1.1.1 Computational models of cell sorting 5

1.1.2 The Schelling model 7

1.2 The model 8

1.3 Differential velocity and differential persistence both give rise to segregation 12

1.4 Segregation increases according to a power law until a steady state level is reached 12

1.5 Volume exclusion effects, system size, and initial conditions do not affect the results 15

1.6 Discussion 18

1.7 Conclusion 19

2 Introduction **21**

2.1 Examples of epithelial ordering 21

2.2 Junction remodelling 22

2.3 Models of epithial ordering 25

2.4 Thesis outline 28

3 Methods **29**

3.1 Experimental methods 29

3.2 Image Processing and Data Analysis 30

3.2.1 Detecting neighbour exchange events 33

3.3 Fluorescence Intensity Measurements 35

4 Properties of neighbour exchange events in the notum 38

4.1 Neighbour exchange events are not associated with large-scale morphogenetic changes . . . 39

4.2 Neighbour exchange events vary in orientation and occur with no apparent spatial pattern . . . 41

4.3 Neighbour exchange events do not cause local tissue deformation 44

4.4 Neighbour exchange events are associated with a redistribution of apical area . . . 47

4.5 Neighbour exchange events are temporally random . . . 49

4.6 Neighbour exchange events are reversible . . . 51

4.7 Total junction length is unchanged during neighbour exchange events 54

4.8 Discussion . . . 56

5 Stochastic Fluctuations of Junctions 58

5.1 Junction length fluctuations resemble a random walk process . . . 58

5.2 The mean squre displacement curve for junction fluctuations shows subdiffusive behaviour . . . 62

5.3 There is no significant difference between the persistence length distributions of T1 and non-T1 junctions . . . 65

5.4 Contraction and expansion is symmetric in neighbour exchange . 71

5.5 Discussion . . . 73

6 Ordering over the course of pupal development 74

6.1 Tissue order increases over the course of development . . . 75

6.2 Steady increase in order over several hours is driven entirely by neighbour exchange . . . 77

6.3 Discussion . . . 81

7 The role of myosin in regulating junction fluctuations 83

7.1 There is no polarization of junctional Myosin II within the tissue . 84

7.2 Myosin II on individual junctions fluctuates over time . . . 86

7.3 The autocorrelation for Myosin II fluorescence intensity decays exponentially . . . 88

7.4 Changes in Myosin II precede changes in junction length . . . 89

7.5 Stochastic Model of Junction Fluctuations Driven by Turnover of Myosin . . . 92
7.6 Discussion . . . 99

8 The role of Myosin II in neighbour exchange events 101
8.1 The frequency of neighbour exchange events is inversely proportional to Myosin II levels . . . 102
8.2 A reduction in Myosin II makes neighbour exchange events more reversible . . . 104
8.3 Regulation of the frequency of neighbour exchange events . . . 106
8.3.1 The variation of junction lengths is similar in Control, Rok^{RNAi}, and Rok^{CAT} . . . 106
8.3.2 The mean square displacement curves are similar for Control and mutants . . . 107
8.3.3 Myosin II slightly reduces the diffusion coefficient of junction fluctuations . . . 110
8.3.4 Junction fluctuations are mean-reverting, but the degree does not depend on Myosin II . . . 113
8.4 The frequency of neighbour exchange events can be explained by the probability of successful junction remodelling once at a four-way vertex . . . 115
8.5 Myosin II regulates neighbour exchange events late in development 116
8.6 Discussion . . . 119

9 Spatial correlations in the tissue 122
9.1 The effect of junction fluctuations does not spread beyond first neighbours . . . 122
9.2 The angle-dependence of cross-correlations can be explained by a simple analytical model . . . 125

10 Conclusion 129

Bibliography 133

List of Figures

1.1 **Schematic for cell sorting models** 9

1.2 **Time course of segregation** 13

1.3 **Time course of segregation as quantified by the interface index γ** . . 14

1.4 **Steady state level of segregation** 15

1.5 **Finite size effects and initial conditions** 17

2.1 **Example of a neighbour exchange event** 23

2.2 **Junction remodelling in germ-band extension** 23

3.1 **Segmentation of time-lapse images** 31

3.2 **Class definition for 'junction' objects** 32

3.3 **Junction length calculation** 32

3.4 **Class definition for 'cell' objects** 34

3.5 **Fluorescence intensity for Myosin II and Bazooka** 36

4.1 **Tissue area and aspect ratio** 40

4.2 **Spatial properties of T1 events in the tissue** 43

4.3 **Internal and external aspect ratio of four-cell clusters in T1 events** . 46

4.4 **Change in cell area and number of edges during T1 events** 48

4.5 **Temporal distribution of T1 events in the tissue** 50

4.6 **Reversibility of neighbour exchange events** 53

4.7 **Junction length changes during T1 events** 55

5.1 **Junction length time series for T1 and non-T1** 60

5.2 **Distribution for persistence length** 61

5.3 **Schematic for mean square displacement** 63

5.4 **Ensemble-averaged mean sqaure displacement curve for junction fluctuations** . . . 64
5.5 **Filtering of junction length time series** . . . 68
5.6 **Persistence lengths** . . . 69
5.7 **Persistence lengths, time, and ballistic velocity** . . . 72

6.1 **Ordering over the course of pupal development** . . . 76
6.2 **Disruptive effect of bristle cells** . . . 79
6.3 **Ordering of polygons** . . . 80
6.4 **Ordering of junction variation, global and local** . . . 81

7.1 **Properties of Myosin and Bazooka in the tissue** . . . 85
7.2 **Time traces for junction length and Bazooka and Myosin intensities.** 87
7.3 **Myosin autocorrelation** . . . 89
7.4 **Crosscorrelation functions for Myosin II and Bazooka intensity against junction length** . . . 91
7.5 **Myosin model** . . . 96
7.6 **Myosin model, crosscorrelation minimum** . . . 98

8.1 **Frequency of neighbour exchange events** . . . 103
8.2 **Reversibility of neighbour exchange events** . . . 105
8.3 **Standard deviation of junctions** . . . 107
8.4 **Mean square displacement curves** . . . 109
8.5 **Diffusion coefficients estimated from MSD curves** . . . 111
8.6 **Mean reversion of junction length fluctuations** . . . 114
8.7 **Frequency of attempted neighbour exchange events** . . . 116
8.8 **Results for Control 25h** . . . 118

9.1 **Crosscorrelation for neighbouring junctions** . . . 123
9.2 **Crosscorrelations across the tissue** . . . 124
9.3 **Schematic for crosscorrelation as a function of angle** . . . 126
9.4 **Crosscorrelation as a function of angle** . . . 127

Acknowledgements

I would like to thank Buzz Baum for all his help and for his enthusiasm and patience. I am also grateful to Alexandre Kabla. His kindness, initiative and support made completing this PhD possible. And not least, I am thankful for Tom Duke, who was an inspiration.

My primary collaborator Scott Curran has been brilliant throughout and understanding during the tough spots. I also want to thank the other members of the Baum lab.

I have been lucky enough to collaborate with many great people: Guillaume Salbreux, Jasper Bathmann, Marc de Genne, Kristian Moss Bendtsen. I also want to thank Fintan Nagle for patiently talking me through image processing in Matlab.

I am grateful for the support I have received from CoMPLEX throughout my PhD. In particular, Gemma Ludbrook has been fantastic.

I am grateful to Johan Paulsson and everyone in the Paulsson lab, in particular Rishi Jajoo, for an amazing six months. I learnt so much.

I am thankful for the Cambridge Writing Group and everyone in it who where there with humour, support and tea at a crucial time, in particular Sheila Guymer. I am thankful to Michael and Andrew. And I am grateful for Hannah Price, whose friendship and support has carried me through.

I am deeply grateful to Tom Hiscock, whose kindness and joyfulness has lifted me up this past year. I also want to thank Moira and Henry.

Finally, I want to thank Jeppe Juul, my best friend and the best teacher I have ever had. Jeppe has been involved in everything I have ever done. Without his tireless patience and constant support, I could not have completed this PhD. I am very grateful.

Chapter 1

Kinetics of Cell Sorting

1.1 Introduction

An essential part of embryonic development is the sorting of different cell types into distinct domains to form tissues and organs [1]. Cell sorting processes *in vivo* can be reproduced *in vitro* using cells from dissociated embryonic tissue. When neural retinal and pigmented epithelial cells from chick embryos are thoroughly intermingled and allowed to reaggregate, they spontaneously self-assemble into homotypic domains [2]. The same phenomenon occurs in heterotypic mixtures of ectoderm, mesoderm and endoderm progenitor cells from zebrafish embryos [3]. In addition, cell sorting has been observed for dissociated *Hydra* cells, co-cultures of cells not in contact during normal development, and mixtures of cells extracted from different species [4, 5, 6, 7, 8].

Understanding how segregation emerges and is maintained, is also important for studying tissue homeostasis and cancer invasion. When cancer becomes metastatic, tumor cells invade adjacent tissue. As cancer cells become miscible with healthy cells, the tissue is no longer able to maintain sharp compartment boundaries. Consequently, it has been argued that malignant invasion may be regarded as a process of cell sorting in reverse [9].

In this part of the thesis, I study the kinetics of cell sorting. I use mathematical modelling to investigate the role of cell motility in sorting and suggest a novel mechanism for how segregation can emerge in a population of motile cells. The work in this part of the thesis has been published in the paper "A kinetic mechanism for cell sorting based on local variations in cell motility" [10]. Additional work, not described here, was published in the paper "Schelling model of cell segregation based only on local information" [11].

1.1.1 Computational models of cell sorting

The segregation of cells into homotypic domains is phenomenologically similar to the phase separation of fluids [12, 2]. This analogy underlies the differential adhesion hypothesis (DAH), developed by Steinberg in the 1960s, which posits that the adhesive interactions between cells give rise to surface tension and that the equilibrium configurations of the tissue are those that minimize the surface energy [13, 14, 12, 15]. The differential adhesion hypothesis has since been studied extensively using the cellular Potts model, also known as the Graner and Glazier model [16, 17]. It has been succesful in reproducing a range of cell sorting phenomena [18, 19, 20, 21, 22], including the envelopment of more adhesive cells by less adhesive ones observed in sorting experiments with embryonic tissue from chicks [6] and zebrafish [23].

However, the cellular Potts model is principally an equilibrium model. The equilibrium configuration of the system is given by the minimum of the Hamiltonian, which contains terms that capture different aspects of tissue mechanics. The kinetics, on the other hand, are determined by an auxiliary dynamics - typically a Markov chain Monte Carlo method - used to relax the system to the equilibrium configuration [24]. Indeed differences in the choice of Monte Carlo algorithm could account for the discrepancies in the scaling behaviour reported for different computational implementations of the DAH. Specifically, the paper by Nakajima et al. [22] reported that the average domain size grows according to a power law, whereas previous studies [17, 18] observe slow logarithmic growth.[1] Recent work has demonstrated that the cellular Potts model can be applied as a kinetic model if the Hamiltonian and Monte Carlo algorithm are modified appropriately [24, 20].

Other computational models have been developed to investigate the time course of segregation and, in particular, the role of cell motility in sorting. The models by Belmonte et al. [25] and Beatrici et al. [26] both describe a binary system of self-propelled particles that have a tendency to align their motion with that of neighbouring cells. Belmonte et al. simulate the effect of differential

[1] Nakajima et al. [22] use a standard Metropolis algorithm for their dynamics, whereas the Monte Carlo simulations in [17] employ a modified Metropolis algorithm resembling that of the Voter model.

adhesion in a motile population of cells. The two cell types have the same intrinsic motility properties, but the interaction strengths differ between cells of the same type and cells of different type. They argue that even weak coherent motility speeds up segregation relative to what has been reported for cellular Potts model implementations of the DAH. By contrast, Beatrici et al. consider a system of cells with homogenous adhesion forces, but with speeds of constant modulus v_0 and v_1. They demonstrate that differences in the intrinsic motility properties of cells, along with a tendency for cells to align their motion, can drive cell sorting. Spontaneous segregation has also been demonstrated for dense mixtures of self-propelled and passive particles using Brownian dynamics simulations [27]. Including motility properties in the cellular Potts model, with motile and non-motile cells in equal proportion, also leads to segregation with large clusters of non-motile cells surrounded by streams of motile cells [28].

What these models have in common is their focus on *intrinsic* motility properties. Motility is assumed to be an inherent property of the cell, rather than a function of the local environment. By contrast, experimental work has shown that in tissues or compact aggregates of cells, each cell interacts strongly with its neighbours and factors including adhesion, cortical tension, the viscoelastic properties of cells, and collective motion all affect motility [29, 30, 31]. In particular, Rieu et al. studied the two-dimensional trajectories of single endodermal *Hydra* cells in aggregates comprised of either endodermal or ectodermal cells. In both environments, endodermal cells perform a persistent random walk, with persistence dominating at small time scales. Interestingly, diffusion is more than two times faster for endodermal cells in an ectodermal environment, with reported diffusion constants of $D_{endo-ecto} = 1.05 \pm 0.4 \mu m^2/min$ and $D_{endo-endo} = 0.45 \pm 0.2 \mu m^2/min$. Despite these experimental observations, it is not known to what extent local variation in cell motility contributes to sorting.

In this chapter, I present a minimal model where the diffusion of cells depends on the composition of the local environment. A key property of the model is that the two cell types are symmetric with respect to their *intrinsic* motility properties. Instead, differences in motility arise solely from the interaction between a cell and its neighbours. This allows us to test whether asymmetry is a prerequisite

for cell sorting.

1.1.2 The Schelling model

Around the same time that Steinberg was developing the differential adhesion hypothesis [13, 14, 12, 15], Schelling was investigating segregation phenomena at the at the scale of societies [32, 33, 34]. Schelling showed how slight preferences in neighbourhood composition can lead to residential separation of ethnic groups within cities. The Schelling model describes a system in which interacting agents, belonging to one of two groups, move on a square grid according to a utility function defined by their current environment and the environment they have the option of moving to. For each agent, the utility of a site on the grid is determined by the fraction of agents of their own group within the local neighbourhood. If an agent is surrounded by agents of the other group, utility is low and relocation is desirable. Strikingly, Schelling found that even weak individual preferences for homophily, resulted in strong segregation.

This type of model has since been studied on networks, in continous-space models, and analytically [35, 36, 37, 38]. In addition, it has been applied in the context of phase separation kinetics in physics and efforts have been made to map it to the Ising spin model [39, 40]. However, its relevance for biological systems has not previously been explored.

Conceptually, the model presented here is related to the Schelling model and was in fact inspired by it. The key assumption of our model is that the diffusion of cells depends on the fraction of cells of the same type in the local environment, which is analogous to the utility function for agents in the Schelling model. However, to apply the Schelling idea to the study of cell sorting, it has to be modified to make the dynamics entirely local. Previous versions of the Schelling model are non-local in the sense that agents have information about, and access to, non-adjacent residence sites when evaluting whether to move. This is a reasonable assumption for people in cities, but not for populations of cells.

1.2 The model

The aim of this chapter is to investigate whether *intrinsic* differences in motility are necessary for cell sorting. To do this, we consider a model of sorting where differences in cell motility arise solely from how cells interact with their surroundings. The model is inherently a kinetic model and the steady state configurations emerge from the local interactions of cells rather than being specified *a priori*.

The model describes the diffusion of a binary mixture of cells that are symmetric with respect to their motility properties. For each cell, the effective diffusion depends on the composition of the local environment, specifically the proportion of neighbouring cells of the opposite type. The cells diffuse on a square continuous-space plane with side lengths L and periodic boundary conditions. Each cell has a position $\vec{x}_i$, and moves according to

$$\vec{x}_i(t + \Delta t) = \vec{x}_i(t) + \vec{v}_i \Delta t, \tag{1.1}$$

where we without loss of generality set $\Delta t = 1$. The total number of cells is $N = L^2$, which in the case of hexagonal packing would give an equilibrium distance between neighbouring cells of $R_e = \sqrt{2/\sqrt{3}} \approx 1.07$. To account for volume exclusion, we introduce a radial contact force f_{ij} between cells, as given by 1.2. The contact force is nonzero when the separation r_{ij} between two cells i and j is smaller than the threshold r_0, at which cells can sense their neighbours. It is repelling if cells are closer than their equilibrium distance r_e and attractive otherwise.

$$f_{ij} = \begin{cases} 1 - \frac{r_{ij}}{R_e} & \text{for } r_{ij} < r_0 \\ 0 & \text{for } r_{ij} \geq r_0 \end{cases} \tag{1.2}$$

The radial contact force ensures that cells are evenly distributed within the plane. Note that volume exclusion is not necessary for the segregation behaviour observed in the model, as we will see in Figure 1.5.

In the model, the motion of each cell is random. Except for contact forces, motion is purely diffusive with no orientational bias. However, the speed of

diffusion changes depending on the local environment of the cell, which we characterize by the fraction γ_i of neighbouring cells of the opposite type.

$$\gamma_i = \frac{n_{\neq}}{n_{=} + n_{\neq}}. \tag{1.3}$$

Here $n_{=}$ is the number of cells of the same type as i and $n_{\neq}$ is the number of cells of opposite type, within a distance r_0. A common measure for the degree of segregation in a system is the interface index γ [25, 26, 22, 8], which is given by the average of γ_i for all cells in the system. When $\gamma \approx 0$ the two cell types are completely segregated.

How the diffusive component of the velocity depends on γ_i can be formulated in two distinct ways, which I will refer to as the differential velocity model and the differential persistence model, respectively. The two models are summarized in Figure 1.1. In the following, I describe both models and show analytically that for any spatial arrangement of cells, the two models yield the same diffusion constants.

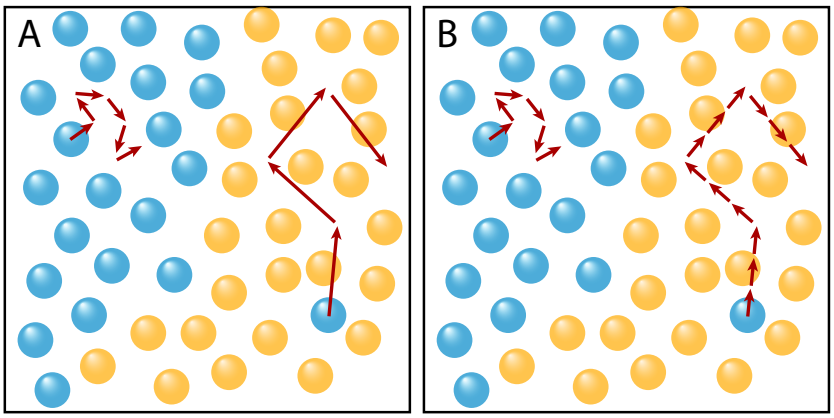

Figure 1.1: Schematic for cell sorting models

Illustration of the two cell sorting models. **a)** In the velocity model all cells perform random walks with a step length that depends on the local environment; cells that are surrounded by cells of the opposite type diffuse fast. The step length is given by equation 1.7 **b)** In the persistence model the step length of the random walk is equal for all cells. However, cells continue in the same direction during a persistence time given by equation 1.5. These two models yield the same diffusion coeffcients for any distribution of cells, when the effect of volume exlusion is ignored.

In the differential persistence model, the step length is the the same for all cells, but how frequently a cell changes direction depends on the composition of

its local environment. As stated, the velocity of a cell contains two components - random motion and contact inhibition. The velocity of a cell i is given by

$$\vec{v}_i = \frac{\alpha}{\sqrt{k}}\vec{u}_i + \beta \sum_j f_{ij}\vec{u}_{ij}, \tag{1.4}$$

where $\vec{u}_i$ is a unit vector of random orientation, $\vec{u}_{ij}$ is a unit vector pointing from cell j to cell i, β is the strength of the contact force, α is the diffusion speed of a cell that is surrounded only by cells of opposite type ($\gamma_i = 1$), and k determines how much faster cells diffuse when they are surrounded by cells of opposite type as opposed to the same type. This form of the velocity was chosen in order for the parameters to be straightforward to interpret in terms of experimentally measurable quantities. In particular, as we will see in equation 1.9, the parameter k may be related directly to the experiments of Rieu et al. [29] and the prefactor for the random motion was chosen to to that end.

Between each random change in orientation, cells continue with the same direction and velocity for a number of time steps T_i. This persistence time is given by

$$T_i = 1 + \gamma_i(k-1). \tag{1.5}$$

Hence, when a cell is surrrounded entirely by its own type ($\gamma_i = 0$), it has $T_i = 1$ and only continues in the same direction for a single time step. By contrast, when all neighbouring cells are of the opposite type ($\gamma_i = 1$), the cell has $T_i = k$. A longer persistence time corresponds to less frequent changes in direction and gives a higher speed of diffusion. Effectively, the motion of a cell can be described as a random walk where each step is of length $v_i T_i$ and takes a duration T_i (see Fig. 1.1). Using this observation and equation 1.4, we can derive the diffusion coefficent of a cell as a function of γ_i, when the effect of volume exclusion is omitted. Note that $\vec{u}_i \cdot \vec{u}_i = |\vec{u}_i|^2 = 1$, since it is a unit vector.

$$D(\gamma_i) \equiv \frac{(\Delta x)^2}{\Delta t} = \langle v_i^2 T_i \rangle = \frac{\alpha^2}{k}\left(1 + \gamma_i(k-1)\right). \tag{1.6}$$

In the differential velocity model, the persistence time is constant, but the step length depends on the local environment of the cell. The velocity of a cell i is given by

$$\vec{v}_i = \alpha\sqrt{\gamma_i + \frac{1-\gamma_i}{k}}\vec{u}_i + \beta\sum_j f_{ij}\vec{u}_{ij}, \tag{1.7}$$

where $\vec{u}_i$, $\vec{u}_{ij}$, α, β, and k are the same as in the differential persistence model. From (1.7) we can find the diffusion coefficient of a cell as a function of γ_i, again omitting the term for the radial contact force. Unlike in the differential persistence model, the persistence time is constant $T_i = 1$

$$D(\gamma_i) \equiv \frac{(\Delta x)^2}{\Delta t} = \langle v_i^2 T_i\rangle = \alpha^2\left(\gamma_i + \frac{1-\gamma_i}{k}\right). \tag{1.8}$$

Note that equation 1.6 and 1.8 are equivalent, demonstrating that the differential velocity and differential persistence model give the same diffusion coefficients for cells in the same environment. They can therefore also be expected to have the same dynamical properties.

We can calculate the ratio between the diffusion contants of cells that are surrounded by opposite or like cells, respectively, to verify the definition of the parameter k.

$$\frac{D(\gamma_i = 1)}{D(\gamma_i = 0)} = \frac{\alpha^2}{\alpha^2/k} = k. \tag{1.9}$$

In the following, I quantify the segregation behaviour in terms of the parameter k, as this may be directly related to the cell sorting experiments of Rieu et al. [29].

A distinguishing feature of the model is that there are no differences in the *intrinsic* motility properties of cells. The physical properties of the two cell types are completely symmetric and differences in motility arise only from the heterogeneity of the local environment they find themselves in.

1.3 Differential velocity and differential persistence both give rise to segregation

Figure 1.2 shows how a binary system of cells evolves when motility is given by differential persistence and differential velocity, respectively. The system is initiated from a completely mixed state $\gamma = 0.5$ and spontaneously orders over time. Ordering proceeds, via the formation of homotypic domains, to a steady state where the two cell types are largely segregated with $\gamma \simeq 0.1$. Interestingly, the steady state is a dynamic equilibrium where the macroscopic configuration changes continually even though the value of γ remains stable.

The simulations demonstrate that segregation can emerge in a binary system where the two cell types are symmetric with respect to their *intrinsic* motility properties. Hence, asymmetry is not a prerequisite for cell sorting.

1.4 Segregation increases according to a power law until a steady state level is reached

We are interested in the time course of the segregation process. From published experimental data, the temporal dynamics of cell sorting follow a power law [8, 41]. I quantify the degree of segregation in the system using the interface index γ. Figure 1.3 shows that γ decreases according to a power law before saturating. The time course shown is for the differential persistence model. In the differential velocity model γ also follows an exponential decay before levelling off, but sorting proceeds more slowly.

There are a few things to note. First, the scaling exponent for the part of the curve that follows a power law, depends on k, and takes the values of 0.025 for $k = 8$ and 0.17 for $k = 64$, for the differential persistence model. We defined k as the ratio of the diffusion constants for a cell surrounded by opposite ($\gamma_i = 1$) and like ($\gamma_i = 0$) cells, respectively. The scaling exponent defines the speed of segregation and is therefore expected to increase when the relative difference between diffusion coefficients is larger. For $k = 64$, the exponent is similar to the values reported in other computational studies of cell sorting kinetics [25, 26], but

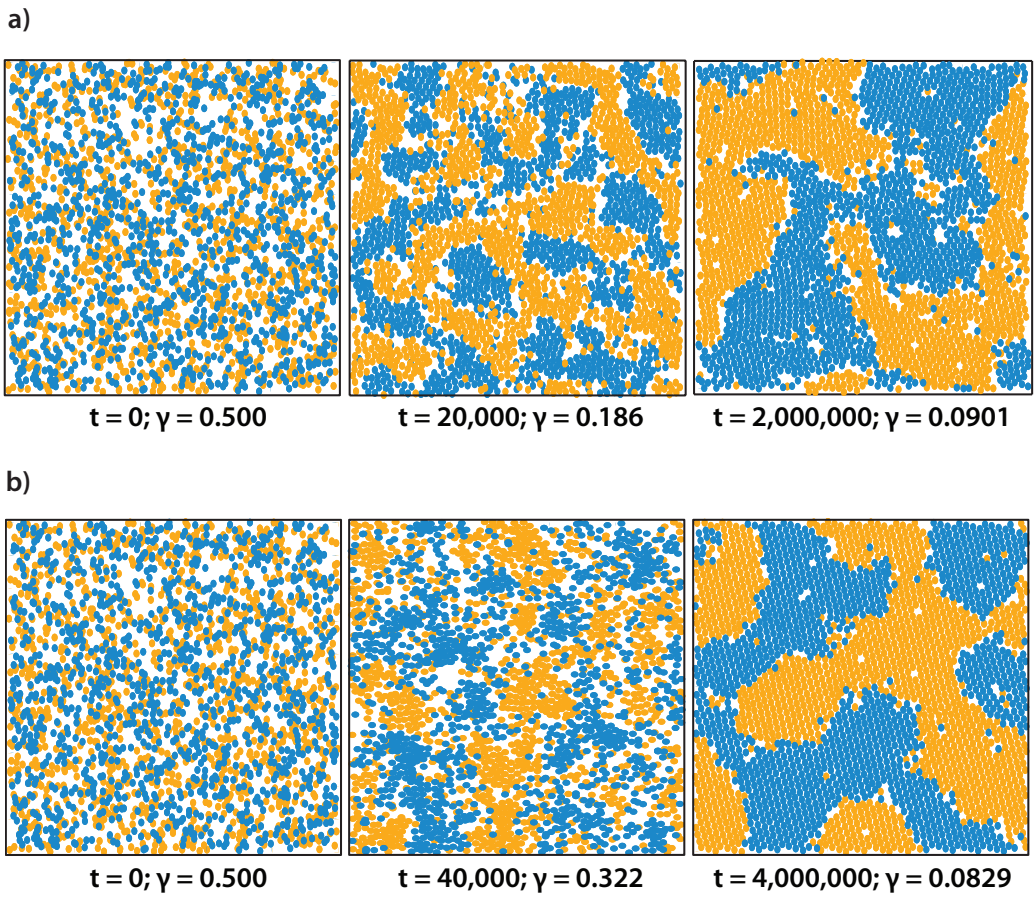

Figure 1.2: Time course of segregation

a) Time course of the segregation process for 2500 cells in the differential persistence model. As the cells gradually gather in larger clusters, the interface index γ decreases. The ratio of the diffusion constants is $k = 64$. **b)** Time course of the segregation process in the differential velocity model. Parameters are the same as for the differential persistence model. Sorting proceeds more slowly in the differential velocity model than in the differential persistence model. For this reason, the segregation process is shown for different time points in **a)** and **b)**.

lower than those reported experimentally [8]. Belmonte et al. [25] also quantify segregation using the interface index γ and report an exponent of around 0.18 for a binary system of cells with a mixture ratio of 1:3 (see their Figure 2). For sorting of mixtures of primary fish keratocytes and EPC keratocytes *in vitro*, Méhes et al. [8] report a scaling exponent of 0.32 for the decrease of the interface index and 0.74 for the growth of homotypic clusters[2].

Second, the degree of segregation at steady state also depends on the pa-

[2]If clusters are uniform with respect to their shape and size, the relationship between the interface index and the cluster size should be linear and their scaling behaviour should be characterized by the same exponent. However, *in vitro* clusters are not uniform, resulting in different exponent values [8].

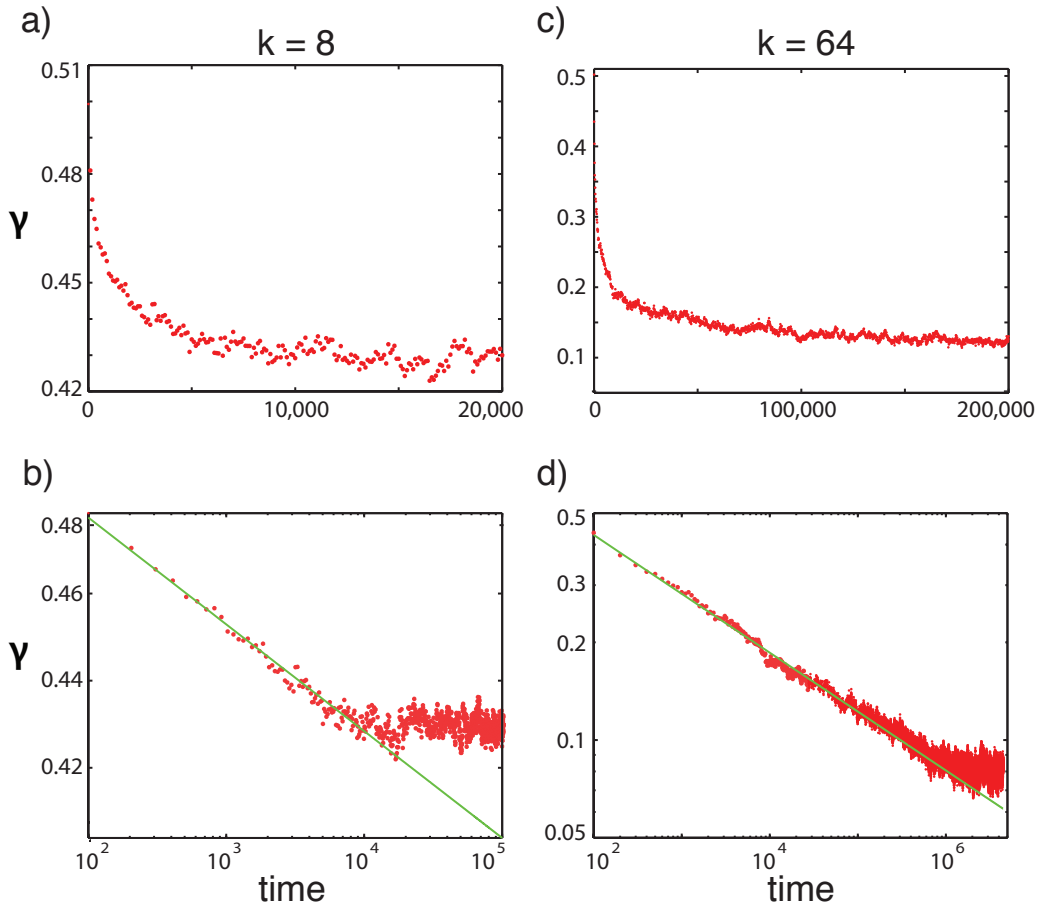

Figure 1.3: Time course of segregation as quantified by the interface index γ

a)-b) Development of the interface index γ as a function of time for $k = 8$ in the differential persistence model. The results are the average of 10 simulations and are shown on a linear and log–log scale. **c)-d)** The interface index γ over time for $k = 64$ on a linear and log-log scale. For high k, a more pronounced segregation is observed. The interface index is seen to decrease according to a power law until it saturates at an equilibrium value. The exponent, found as the slope of the straight line fit (green), increases with increasing k, and takes the values 0.025 for $k = 8$ and 0.17 for $k = 64$.

rameter k, with more pronounced segregation occuring for high values. Hence, fast diffusion in unalike and slow diffusion in like environments improves segregation. Figure 1.4 shows the steady state value of γ as a function of k. For $k = 1$, the diffusion constant of a cell is the same in an environment of opposite and like cells. The system therefore remains in a completely mixed state with $\gamma = 0.5$. Interestingly, for $k = 2$, which is the value reported by Rieu et al. [29] for endodermal and ectodermal *Hydra* cells, very little segregation occurs. In addition, the interface index plateaus at $\gamma \sim 0.1$ and complete segregation is not achieved even for high values of k. This is in fact in agreement with the work by

Méhes et al. [8], where they report that the interface index tends not to decrease below 0.1 as segregation slows to a halt. However, other *in vitro* experiments do observe that sorting proceeds until complete segregation is reached [2, 3].

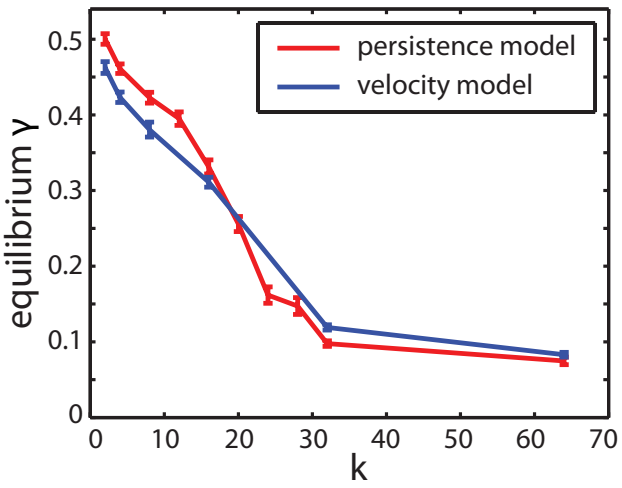

Figure 1.4: Steady state level of segregation

Value of the interface index γ, at which the system saturates, as a function of k. The parameter k is the ratio of the diffusion constant of cells surrounded by opposite or like cell types, respectively. For large k, the system reaches a more segregated configuration. The equilibrium interface indices are calculated as averages over 105 time steps after the equilibrium is reached, and averaged over 10 simulations. The errorbars indicate the standard error of the mean across simulations. (red) Differential persistence model. (blue) Differential velocity model.

1.5 Volume exclusion effects, system size, and initial conditions do not affect the results

Having established the segregation behaviour of the two models, I want to briefly touch upon potential sources of artifacts in the results.

First, I included a radial contact force in the model to account for volume exclusion and ensure that cells are evenly distributed within the plane. However, the specific form of the contact force does not affect whether cells segregate. In fact, even when volume exclusion effects are omitted ($\beta = 0$), the model gives segregation, just with cells unevenly dispersed. In addition, the time course of the segregation process still follows a power law. This is shown in Figure 1.5.

Second, the simulations were carried out for a system size of $N = 2500$ cells with periodic boundary conditions. Figure 1.5 shows how the segregation be-

haviour depends on system size. When the domain size (cluster correlation length) is much smaller than the system, finite size effects are negligible. Therefore, the scaling behaviour for the initial part of the curve, when the system is mixed and heterotypic domains are small, does not depend on system size, except for very small systems. As sorting proceeds towards segregation, domains grow and finite size effects start to play a role. Consequently, the value of γ at which the system saturates depends on N. However, for system sizes of $N > 1000$, the effect is insignificant. The size dependence is qualitatively the same as what was reported by Belmonte et al. [25] (Fig. 3). That paper also showed that the time course of segregation may be rescaled to remove the effect of system size.

Third, throughout this chapter, the system has been initiated from a random mixed configuration with $\gamma = 0.5$. However, the eventual steady state configuration does not depend on this initial condition. Figure 1.5 shows how the system evolves over time when iniated from a random and ordered configuration, respectively. When the two cell types are initially separated, the border between them is not maintained. Instead, the cells slowly mix, and the value of γ increases until it reaches the same equilibrium value as if starting from a random configuration.

In summary, the results presented in the previous sections are robust to omitting the effect of volume exclusion and changing the size and initial configuration of the system.

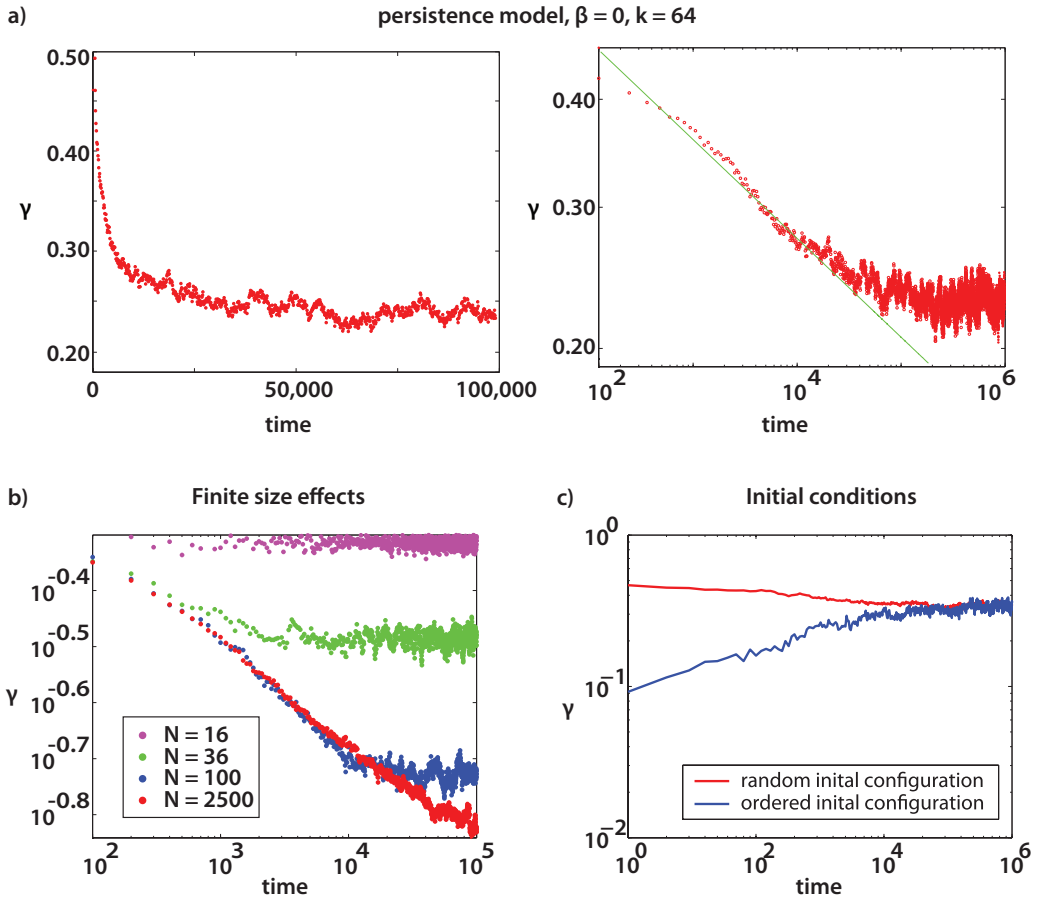

Figure 1.5: Finite size effects and initial conditions

a) Development of the interface index as a function of time for $k = 64$ for the differential persistence model with $\beta = 0$, on (left) a linear scale and (right) a log-log scale. As when volume exclusion effects are included, the segregation process follows a power-law. **b)** The figure shows how the interface index, γ, evolves over time for systems with different number of cells, N. All simulations are for $k = 64$. The results are shown on a log-log plot. When the domain size (cluster correlation length) is much smaller than the system, finite size effects are negligible. Hence, the initial scaling behaviour will not depend on system size. As sorting proceeds towards maximum segregation, finite size effects start to play a role and the value of γ at which the system saturates depends on N. The size dependence shown here is qualitatively the same as that in Figure 3 in [25]. **c)** The figure shows how γ evolves over time for random and ordered initial conditions, respectively, with $k = 16$. This demonstrates that the steady state value of γ is the same whether the system is initialized from a random or a segregated initial configuration.

1.6 Discussion

The aim of this chapter was to investigate the role of motility in cell sorting. The results demonstrate that asymmetry in the physical properties of cells is not a prerequisite for sorting. In fact, segregation can emerge just from cell motility being a dynamic property that changes in response to the local environment of a cell.

In the model, the time course of segregation follows a power law before reaching a steady state level. This is consistent with the scaling reported by Méhes et al. [8, 41] for cell sorting in mixtures of keratocytes from different species. They report that for mixtures of primary fish keratocytes and EPC keratocytes, the decrease of the interface index γ and the growth of homotypic clusters are approximately linear on a log-log scale. It should be noted that they only show one decade of data, making it difficult to determine whether the data actually display power law scaling.

Despite displaying the correct scaling behaviour, a closer comparison of the results of the model with *in vitro* experimental data shows that it cannot be the only ordering mechanism driving cell sorting.

First, the value for k reported by Rieu et al. [29] for endodermal and ectodermal *Hydra* cells is around 2. In the model, the level of segregation increases with k and for $k = 2$ the system shows very little segregation. I tried implementing other functional forms for how the diffusion coefficient depends on the interface index, including a threshold instead of the linear dependence given by Eq. 1.6, and these did not significantly affect the segregation behaviour for low values of k.

Second, the model does not generate complete segregation, even for high values of k. By contrast, cell sorting *in vitro* often proceeds until the two cell types are completely segregated, with one phase enveloping the other. Computational implementations of the differential adhesion hypothesis are able to successfully reproduce this envelopment. In addition, it provides an explanation for the inside/outside order of the phases in terms of their relative surface tensions [6, 42]. The model presented here has no inbuilt asymmetry and would, therefore, not be expected to reproduce the enveloping behaviour without a mechanism for

breaking the symmetry.

The model could be expanded to include other aspects of cell dynamics to better reproduce the experimental observations. As measured by Rieu et al. [43], endodermal and ectodermal cells do in fact differ in their intrinsic motility properties and this would likely to promote segregation for lower values of k. In addition, collective motion has been shown to contribute to segregation [25, 26], with even a moderate tendency for cells to align their movement considerably speeding up the segregation process.

It is worth noting that, within the model, we have not specified the molecular mechanism(s) that determine the speed of diffusion of cells. In particular, we have not specified how the interaction between a cell and its local environment affects motility. It could be a response to external cues, such as morphogens or chemotactic substances, or result from cell-cell interactions, including the adhesive properties of cells [44, 31]. It has been shown experimentally, using human kidney cells transfected to express a protein that regulates cell-cell adhesion, that cell motility is anticorrelated with the strength of adhesion [31]. Strong adhesive interactions increase the effective viscosity of the local environment of the cell, which decreases overall cell motion. This suggests a possible molecular mechanism for the model presented here, where differences in the strength of cell-cell adhesion leads to local variation in cell motility, which in turn gives rise to the segregation behaviour observed macroscopically.

1.7 Conclusion

In embryonic development of several species, the segregation of cells into diverse tissues and organs is a fast process. Even though cell sorting has been studied extensively and many mechanisms have been proposed, the speed with which segregation occurs *in vitro* and *in vivo* is still not fully understood, suggesting that several mechanisms could be acting in concert to accelerate the process [8]. The model presented here describes a mechanism for segregation, based on local variation in the cell motility, that could contribute to cell sorting.

In the model, the two cell types are symmetric with respect to their *intrinsic*

motility properties, demonstrating that asymmetry is not a prerequisite for cell sorting. In fact, segregation can arise solely from cell motility being modelled as a dynamic quantity that changes depending on the local environment of the cell.

The model is able to reproduce the scaling behaviour for the time course of segregation observed experimentally, but not the envelopment behaviour observed *in vitro*. In addition, the parameter values reported from experiment do not lead to significant segregation within the model. Further work is needed to understand the relative contributions of locally varying cell motility, differences in intrinsic motility properties, and collective motion to the kinetics of cell sorting.

Chapter 2

Introduction

In several mature epithelia, cells are arranged in an ordered hexagonal array. This order emerges from an initially disordered state, without explicit genetic instruction [45, 46]. How does the tissue transition from disorder to order in an effective and robust way? To address this question, I examine the process of ordering in the *Drosophila* notum - a tissue that develops hexagonal order without undergoing substantial growth or directed morphogenesis.

2.1 Examples of epithelial ordering

Recent studies of patterning in *Drosophila*, demonstrate that a variety of mechanisms facilitate the ordering of epithelial tissue. In the *Drosophila* wing, epithelial cells rearrange from irregular to hexagonal packing shortly before hair formation [47]. At this point in development, the fraction of hexagons increases from around 45% to nearly 80% as a result of cell neighbour exchange. Classen et al. [47] showed that this hexagonal packing depends on the activity of the planar cell polarity proteins, which polarize along the proximal-distal axis in the prepupal wing prior to packing. They propose that these proteins polarize the trafficking of Cadherin during junction remodelling and that this regulates neighbour exchange events to move the system towards hexagonal packing.

The *Drosophila* retinal epithelium is made up of a hexagonal array of units called ommatidia that contain a cluster of photoreceptor cells surrounded by accessory cells, including four lens secreting cone cells. The quartet of cone cells express N-cadherin adhesion molecules and form an ellipsoid structure surrounded by cells not expressing N-cadherin. Work by Hayashi et al. [48], showed that this patterned expression of N-cadherin effectively selects for cell arrangements that minimize surface energy and precisely correlate with soap

bubble configurations.

Cohen et al. [49, 50] investigated the role of structured noise in the patterning of microchaete bristle cells on the *Drosophila* notum. They showed that bristle patterning depends on a population of filopodia that establish transient signalling contact between non-neighbouring cells. Interestingly, noise in filopodial signalling contributes to ordering and provides a self-organizing mechanism for the gradual refinement of bristle patterning.

Other studies have highlighted how stochastic fluctuations in processes at the molecular and cellular level are important in single cells [51, 52], but less is known about the role of noise in developing tissues. In this thesis, I quantify stochastic fluctuations in junction length and investigate to what extent they contribute to the emergence of hexagonal cell packing in the tissue. As in the *Drosophila* wing, ordering is driven by junction remodelling and largely occurs in the absence of cell division, apoptosis and delamination. The next section outlines our what is currently known about neighbour exchange events and their role in tissue ordering.

2.2 Junction remodelling

Several cellular events contribute to the shaping of a developing embryo. These include cell division, cell apoptosis and delamination, and cell neighbour exchange. Neighbour exchange events proceed with a junction contracting until four cells meet at a four-way vertex. This is followed by loss of contact between one pair of adjacent cells and the formation of a new junction between cells not previously in contact, thereby changing the cell-cell connectivity (see Figure 2.1). This process allows cells to gain or lose an edge and changes the polygon distribution in the tissue.

Whilst neighbour exchange is critical for hexagonal ordering of cell shapes, much of what we know about it comes from markedly different process: germband extension (GBE) in *Drosophila*. During germ-band extension, the length of the embryo more than doubles along the anterior-posterior (A-P) and the width along the dorsal-ventral (D-V) axis narrows accordingly. The process takes

approximately 1 h and is driven by a process of coordinated cell intercalation and neighbour exchange [53, 54].

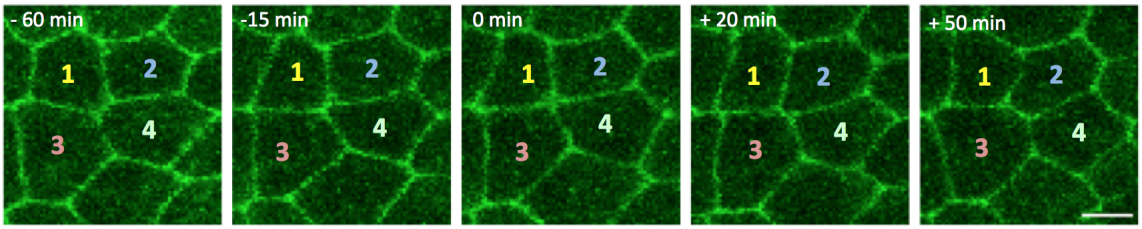

Figure 2.1: Example of a neighbour exchange event

Example of junction remodelling during a neighbour exchange event. A junction shrinks until four cells share a point of contact (a configuration referred to as a four-way vertex), followed by the formation of a new junction. Before the event, cells 1 and 4 were neighbours and cells 2 and 3 did not share a domain of contact. After the event, cells 1 and 4 are no longer in contact and cells 2 and 3 have become neighbours. Neighbour exchange events are also known as T1 transitions. From [Curran 2015].

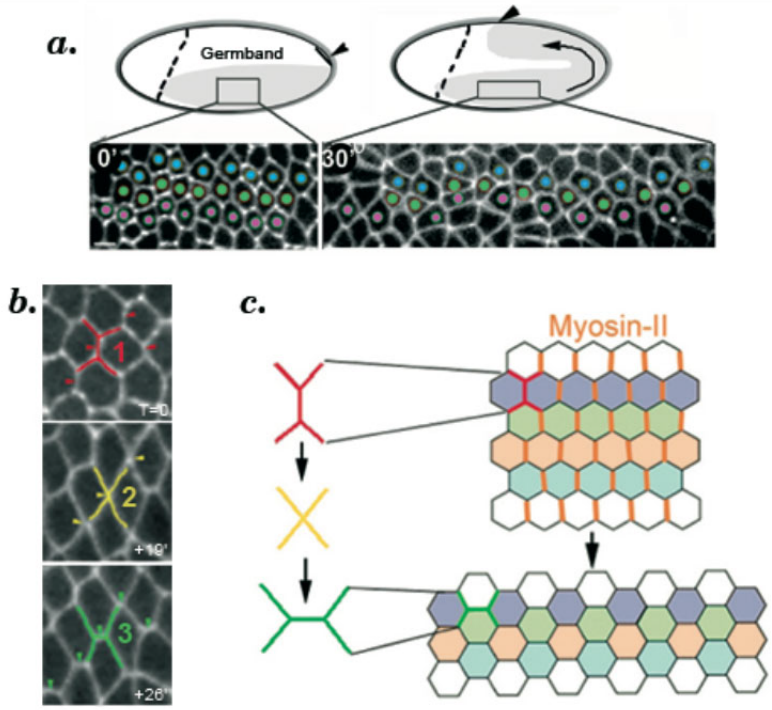

Figure 2.2: Junction remodelling in germ-band extension

a) Position of the germband within the developing embryo, before and after cell intercalation. Cell intercalation causes the germband to elongate and the increase in length is accomodated by dorsal extension. **b)** Example of a T1 event. **c)** Schematic of cell intercalation causing the tissue to elongate. Myosin-II is specifically enriched at junctions oriented along the D-V axis. These junctions shrink, followed by the formation of a new junction along the A-P axis. Adapted from [53]

Junctions parallel to the D-V axis shrink, leading to a four-way vertex configu-

ration, followed by the formation of a new junction oriented along the A-P axis. The result is a rearrangement of cell neighbours, with cells along the D-V axis intercalating between cells adjacent along the A-P axis, and an overall elongation of the tissue.

This planar remodelling of junctions is driven by local forces at cell interfaces [53]. Myosin II is specifically enriched at shrinking junctions oriented along the D-V axis and causes these junctions to shrink by increasing junctional tension [53, 55, 56].

It has been shown that this shrinkage is in fact caused by pulses of medial actomyosin flowing towards junctions, rather than the steady state distribution of Myosin II at these junctions [54]. Myosin II forms small clusters, which coalesce with actin in the medial region of the cell and flow towards D-V junctions [54]. Laser ablation and cross-correlation analysis of junction length and Myosin II intensity in the medial regions and at junctions indicated separate mechanical functions for the medial and junctional pools of myosin. Pulsed flow of medial Myosin II towards D-V junctions causes shrinkage and the subsequent accumulation of junctional Myosin II stabilizes the junction length.

The polarized localization and activity of Myosin II is critical for cell intercalation and tissue elongation. A reduction in Myosin II activity or a loss of the planar polarized localization in the tissue, disrupts junction remodelling and results in incomplete elongation of the germband [53, 54, 57]

In summary, during germ-band extension, neighbour exchange events are highly stereotyped and tightly coordinated to execute large-scale tissue morphogenesis. This is a very different process from the emergence of hexagonal order in epithelial tissue. In fact, it was shown by Zallen et al. [58] that cell intercalation in GBE is associated with an increase in epithelial disorder, as measured by the fraction of nonhexagonal cells and the variance of the polygon distribution.

However, homeostatic epithelia are ubiquitous in nature and understanding how such tissues are able to respond to local pertubations while maintaining tissue integrity is important for models of wound healing and cancer metastasis [59, 60]. In this thesis, we will develop an understanding of how neighbour

exchange events occur in static tissue and identify how this differs from what has been reported in GBE.

2.3 Models of epithial ordering

Various models have been developed to explain the hexagonal packing geometry observed in epithelial tissue, dating back to the early 1900s when D'Arcy Wentworth Thompson published "On Growth and Form" [61] advocating for the role of physical principles in determining the structure of living systems. Thompson remarked on the prevalence of hexagonal structures in the natural world - from epithelial cells in dragonfly wings, to soap bubbles, to the honeycomb of bees (see also [62] for more examples). He presented a detailed argument for how surface tensions, which tend to minimize the area of contact, can result in hexagonal packing of epithelial cells[1].

More recently, computational models have been used to study order in epithelial tissue. The cellular Potts model [16, 17] was first developed to simulate cell sorting based on differential adhesion, as mentioned in Chapter 1. It has subsequently been extended to address numerous questions relating to tissue mechanics, including cell patterning in the *Drosophila* retina [64] and tumour progression [65]. The model consists of a lattice, where each site (i, j) has a spin $\sigma(i, j)$. A cell is made up of a connected domain of sites with the same spin σ. A collection of N cells are described by a set of N degenerate spins $\sigma(i, j) = 1, 2..., N$. In addition, each cell has a cell type $\tau(\sigma)$, e.g. endodermal or ectodermal. The Hamiltonian for the system is given by Eq. 2.2 and includes terms accounting for cell-cell interactions and cell area elasticity.

$$H = \sum_{(i,j),(i',j') \text{ neighbours}} J[\tau(\sigma(i,j)), \tau(\sigma(i',j'))](1 - \delta_{\sigma(i,j),\sigma(i',j')}) \quad (2.1)$$

$$+\lambda \sum_{\text{spin types } \sigma} (a(\sigma) - A_{\tau(\sigma)})^2 \theta A_{\tau(\sigma)} \quad (2.2)$$

[1]The fascination with the geometric patterns observed in nature, of course, predates Thompson's modelling efforts. In "The Garden of Cyrus" (first published in 1658), Sir Thomas Browne recounts 'the sexangular cels in the honeycombs of bees' and the 'order in the egges of some butterflies and moths' which 'doth neatly declare how nature geometrizeth, and observeth order in all things' [63].

In the first term, the sum is over neighbouring sites (i, j) and (i', j') in the lattice, and J is the surface energy between spins of type τ and τ'. For the second term, λ is a Lagrange multiplier specifying the strength of the area constraint, $a(\sigma)$ is the area of the cell, and $A_{\tau(\sigma)}$ is the target area. The equilibrium configuration for the system is given by the minimum of the Hamiltonian and this configuration is found by relaxing the system using a Monte Carlo method.

An alternative modelling framework was developed by Farhardifar et al. [66]. In the vertex model, epithelial cells are described by a network of polygons, with the edges of the network representing interfaces between cells. Vertices in the network are subject to mechanical forces that can be derived from the energy function for the system.

$$E(\mathbf{R}_i) = \sum_\alpha \frac{K_\alpha}{2}\left(A_\alpha - A_\alpha^{(0)}\right)^2 + \sum_{<i,j>} \Lambda_{ij} l_{ij} + \sum_\alpha \frac{\Gamma_\alpha}{2} L_\alpha^2$$
$$\mathbf{F}_i = -\frac{\partial E}{\partial \mathbf{R}_i}$$

The first term represents an area elasticity with elastic coefficents K_α, where cells have an area A_α and a target area $A_\alpha^{(0)}$. The second term represents the line tension Λ_{ij} at an interface of length l_{ij} between two cells. This term incorporates both cell-cell adhesion, which reduces line tension, and actomyosin contractility, which increases it. The last term describes the contractility of the cell perimeter L_α with coefficent Γ_α. Equilibrium configurations of the network are those that minimize the energy functional. For such configurations, the total force F_i at each vertex vanishes. As in the cellular Potts model, the minima of the energy function are determined by relaxing the network using an auxiliary algorithm, in this case a conjugate gradient method. A key advantage of vertex models is that they include neighbour exchange events explicitly, making them suitable for studying epithelial morphogenesis. The same year as the paper by Farhardifar et al. came out, Hufnagel et al. [67] published a similar model to investigate mechanical feedback as a potential mechanism for controlling organ size. Vertex models have since been used to study germ-band extension [68], ventral furrow formation [69], and cell geometry in the retina [70], all in *Drosophila* (see also [71] for an exhuastive summary of applications).

The problem of computing the global minimum of an energy function is interesting and nontrivial, and is a field of research in itself. Depending on the shape of the energy landscape and the optimization method used, the system can become trapped in a local minimum. Farhadifar et al. [66] showed that certain disordered configurations, in proliferating epithelia, are local minima of the energy function and that this can prevent the tissue from reaching the hexagonal ground state. They suggest that annealing could be an effective mechanism for facilitating hexagonal packing in the tissue. In particular, they show that introducing fluctuations in line tension, in their simulations, is sufficient to drive ordering of the tissue.

In metallurgy and materials science, annealing is a heat process that removes defects in a material. When forging a sword, the steel is heated to a specific temperature and then allowed to cool slowly. This allows defects in the steel to be resolved and yields a more ordered crystalline structure. This concept is the basis for the simulated annealing heuristic, which is an effective technique for finding the global minimum of an energy function. In each step of simulated annealing, the system transitions from its current state e to a neighbouring state e' depending on a probability function $P(e, e', T)$. Changes in configuration that lower the energy of the system are always accepted, whereas the probability of accepting a worse configuration depends on the temperature T. The original formulation was an adaptation of the Metropolis-Hastings algorithm (a Monte Carlo method) [72]. In this implementation, the probability function is $\exp(-\Delta E/T)$, where ΔE is the difference in energy between states e' and e. Annealing is implemented by gradually lowering the temperature T. The algorithm starts with T set to a high value, which allows the system to explore a large search space and avoid getting trapped in local minima, and ends with $T = 0$ to restrict the system to the lowest energy configuation. More rigorously, it has been proved that, under suitable conditions, the simulated annealing algorithm converges to the global minimum of the system [73].

In summary, several models have been proposed to explain the configuration of a hexagonally packed tissue as the minimum of an energy functional that captures the main aspects of tissue mechanics. In simulations, there are many

different algorithms for performing this minimization, simulated annealing being one of these. What is not currently known, however, is what 'algorithm' is used *in vivo* to reach hexagonal order. What heuristic does epithelial tissue implement to evolve from a disordered to an ordered state? I address this question by examining the dynamics ordering in the *Drosophila* notum.

Unlike soap bubbles and foams, epithelial tissues are active systems. They are characterized by continual turnover of proteins and dissipation of energy. In particular, remodelling of the interfaces between epithelial cells requires the construction and disassembly of multiprotein complexes in a controlled fashion [47]. Hence, it is not clear to what extent the premise that ordering proceeds by relaxing the tissue to its equilibrium configuration is valid *in vivo* and we will keep this in mind when interpreting the data.

2.4 Thesis outline

In this second part of the thesis, I take a purely data-driven model-agnostic approach to investigate how ordering proceeds in the *Drosophila* notum. I use data from live imaging of wildtype and transgenic *Drosophila* strains expressing altered levels of active Myosin II. I developed a software package to process and analyse the live imaging data, as described in the next chapter. I characterize the properties of neighbour exchange events in the notum and contrast this with what has been reported in germ-band elongation. I then investigate how stochastic fluctuations in junction length contribute to neighbour exchange and the ordering process in the tissue. Based on an analysis of the dynamics of junction fluctuations and Myosin II intensity, I present a mathematical model for how fluctuations are generated by the stochastic turnover of myosin. Finally, I examine junction fluctuations and junction remodelling in embryos with a reduction/overexpression of Myosin II activity. Taken together, the results suggest a heuristic for how the *Drosophila* notum evolves from a disordered configuration to a hexagonally packed tissue. The work demonstrates how dynamics at the cell level can drive large scale changes in the organisation of the tissue. Furthermore, it provides an experimental grounding for the implementation of dynamics in current and future models of the epithelium.

Chapter 3

Methods

The work on ordering in epithelial tissue was done in collaboration with Scott Curran, another PhD student in the Baum lab. All the experimental work was done by Scott and is described in his PhD thesis [74]. To make it clear when I am refering to his thesis, it will be referenced as [Curran 2015] from now on. The work was an iterative process, with the results of data analysis informing the plan for subsequent experiments.

Here, I include a brief description of the experimental methods used to collect the data this part of the thesis is based on. However, most of the chapter is focused the software package I developed to extract and analyse data from time-lapse images of the notum.

3.1 Experimental methods

We use the *Drosophila* notum as our model system. The pupal case is removed and the pupae is set up for live imaging. Imaging was done at 11.5-13.5 hours and 20-30 hours after pupal (AP) formation. Time-lapse images were collected at either 5 s or 30 s intervals with a microscope resolution of 0.0896 μm/pixel. From the z-stacks, maximum projections of the most apical planes were selected for analysis.

Adherens junctions were labelled using endogenous expression of DE-cadherin-GFP [75]. In addition, reduction and overexpression of myosin were acheived using the UAS/GAL4 system [76]. Flies expressing the following constructs were used:

- *UAS-Rok*^{RNAi}. RNA-mediated interference was used to inhibit *Drosophila* Rho-kinase (Rok). Rok regulates the phosphorylation of the myosin regula-

tory light chain (MLRC) and therefore the activity of Myosin II in the tissue [77].

- *UAS-Rok*^{CAT}. A constitutively active version of Rok was expressed to increase Myosin II activity [78].

- *UAS-Sqh*^{AA}. The *Drosophila* spaghetti squash (sqh) gene encodes the myosin regulatory light chain (MLRC). Expression of a non-phosphorylatable, and therefore inactive, form of MLRC was used to reduce Myosin II activity [79].

- *UAS-Sqh*^{EE}. Expression of a phosphomimetic form of MRLC that is constitutively active was used to increase Myosin II activity [80].

For more details on fly stocks and experimental methods, please refer to [Curran 2015].

3.2 Image Processing and Data Analysis

In order to extract data for the behaviour of junctions and cells in a format amenable to the type of analysis I wanted to do, I developed a custom software package. The code is written in Matlab using class-based object oriented programming. It detects junctions and cells from the segmented images, corrects for drift, tracks junctions and cells between frames, and calculates connectivity within the tissue. This makes it possible to extract time series data for various properties, analyse spatial correlations, and detect when cells change neighbours.

The flow of data within the code is as follows:

- Input segmented time-lapse images.

- In case of microscope drift, generate set of stabilized images by subtracting net translation.

- Identify individual junctions in each image and store these as objects.

- Track junctions between frames and assign a unique ID to each junction.

- For each junction, find the IDs of neighbouring junctions.
- Detect individual cells in each image and store these as objects.
- Track cells between frames and assign a unique ID to each cell.

The input for the code are segmented time-lapse images of the *Drosophila* notum. Segmentation was performed using Packing Analyzer [81]; this was done by Scott Curran and is described in [Curran 2015]. As seen in Figure 3.1, segmentation results in skeletonized images where the width of junctions is 1 pixel.

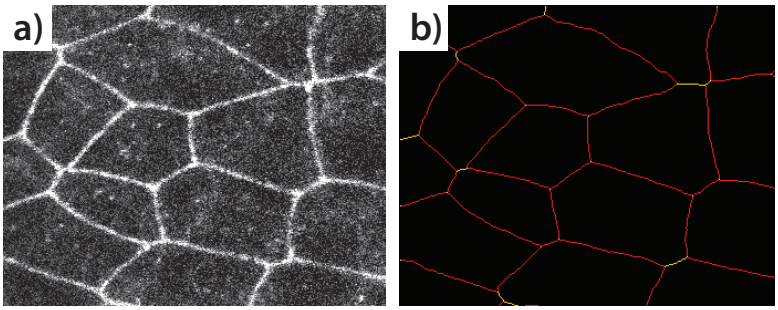

Figure 3.1: Segmentation of time-lapse images

a) Section of the notum with adherens junctions labelled with DE-cadherin:GFP. **b)** The skeletonized image following segmentation in Packing Analyzer. The width of junctions is 1 pixel.

In some cases, the microscope drifts relative to the tissue during imaging. The algorithm for tracking junctions and cells cannot deal with large-scale deformation or significant displacement of the tissue between frames. To deal with this, I used Optical Flow Analysis[1] to calculate the flow field for each consecutive pair of frames. Taking the average of the flow field gives the direction and magnitude of the net translation of the tissue. Mapping the images into a larger space, by subtracting the cumulative net translation for each time point, yields a set of stabilized images that can be input into the code.

The first part of the code identifies individual junctions in each image. Specifically, the code initiates a junction and 'walks' along the bright pixels in the image, storing the coordinates along the way, then terminating the junction when a

[1]Modified from the OFA algorithm available at: http://cs.brown.edu/people/black/code.html and described in [82]

vertex is reached. This is then repeated until all pixels in the image have been visited. Within the code, each junction is an object with associated properties. The properties of the 'junction' class is shown in Figure 3.2. At this stage, only the fields for the vertex coordinates and junction coordinates are filled.

```
junction

Properties:
            junctionID: []
               vertex1: []
               vertex2: []
  junctionCoordinates: []
        junctionLength: []
              midpoint: []
                 angle: []
          neighboursID: []
```

Figure 3.2: Class definition for 'junction' objects

The 'junction' object class the code is based on. The class properties include the junction and vertex coordinates, the length, midpoint, angle, a unique ID used to track the junction across frames, and the IDs of the 1st neighbour junctions.

The code then calculates various properties of junctions, as listed in the class definition. Since junctions can be curved, the vertex-vertex distance is not an accurate measure of junction length. In addition, discretization has the consequence that calculating the length by summing the distance between pixels along the segmented junction would slightly overestimate the length. Instead, junction length is calculated as the diagonal distance connecting consecutive blocks of pixels, as illustrated in Figure 3.3.

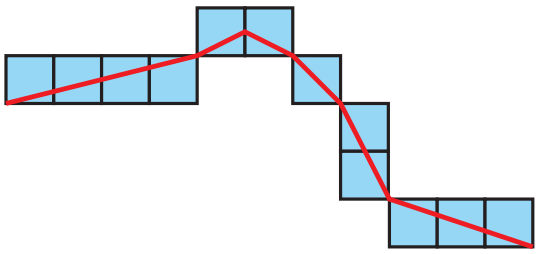

Figure 3.3: Junction length calculation

Illustration of how the length of junctions is calculated in the code. Because of discretization, taking the distance between each neighbouring pixel would slightly overestimate the actual length. Instead junction length is calculated as the diagonal distance connecting consecutive blocks of pixels.

The next step involves tracking junctions between frames and assigning a unique ID to each junction, to make it possible to extract time series for various properties and detect changes in connectivity. The tracking of junctions is done

by finding the midpoints of junctions and using these coordinates as the input for a particle tracking algorithm[2]. The tracking algorithm takes the coordinates of the midpoints at time t and considers all possible matches with the midpoints at time $t+1$ to choose the pairings that minimize the total squared displacement. This is then used to assign each junction a unique ID that identifies it across frames. The results were validated by visual inspection of the assigned IDs - specifically by creating a movie of junctions coloured according to their ID, making errors in continuity easy to spot. Having assigned a unique ID to each junction, the connectivity of the tissue is found and the IDs of neighbouring junctions are stored.

In addition to junctions, the code also detects and tracks cells in the time-lapse images and stores each as an object. The 'epicell' class[3] properties are shown in Figure 3.4 and include vertex coordinates and junction IDs. Cells are detected using the junction objects. Specifically, the code starts at one junction and moves to neighbouring junctions in a clockwise fashion until getting back to the first one, thereby identifying the junctions that make up a cell. This is repeated in a counterclockwise fashion for the same junction. To avoid storing the same cell multiple times, the code loops over junctions starting from $j = 1$ and requires that only neighbouring junctions with larger values of j can be traversed - if that is not available, the code breaks and starts from a different junction instead. Next, the area, perimeter length and midpoint of each cell is calculated. The midpoints are used to track cells between frames and assign unique IDs in the same way as described for junctions.

3.2.1 Detecting neighbour exchange events

One of the aims of this thesis is to study neighbour exchange events. These are difficult to detect manually. I therefore wrote an algorithm to detect neighbour exchange events and make it possible to extract quantitative data related to the junctions and cells involved. The code detects all junctions that contract to a four-

[2]The tracking algorithm is based on code available from the Mathworks repository, written by John C. Crocker. It is described in "Methods of Digital Video Microscopy for Colloidal Studies", John C. Crocker and David G. Grier, J. Colloid Interface Sci. 179, 298 (1996)

[3]'Cell' is not a valid name for a class, as it is in itself a data structure, hence the use of 'epicell', for epithelial cell, instead.

```
epicell

Properties:
       cellID: []
  junctionIDs: []
     midpoint: []
         area: []
    perimeter: []
     vertices: []
       angles: []
```

Figure 3.4: Class definition for 'cell' objects

The 'epicell' object class used in the code to quantify the properties of cells. The class properties include cell area, perimeter, midpoint, internal angles, vertex coordinates, the ID for junctions in the cell, and a unique ID used to track the cell across frames.

way vertex and expand back out, and determines whether they change neighbours in the process. In the fluorescent images, the diameter of four-way vertices is around 6 pixels, corresponding to 538 nm. Segmentation of very short junctions, and especially four-way vertices, is difficult and error-prone. In the segmented images short junctions tend to 'flip', changing orientation and neighbours, even though the fluorescent images show a stable configuration. If not corrected, such false neighbour exchange events would bias subsequent analysis. In particular, *Drosophila* tissues with overexpression of Myosin are harder to segment and display a higher frequency of false neighbour exchanges. To ensure the quality of the data that form the basis of a lot of the work in this thesis, I manually checked every computationally detected event by looking at the corresponding junction in the fluorescent time-lapse images. I used the criteria that the extension of a junction, coming from a four-way vertex configuration, should be stable for at least 5 min and the change in cell neighbours should be clearly visible in the fluorescent images. I made the deliberate decision to set the parameters of the detection algorithm to capture all events that might be neighbour exchanges, i.e. overdetecting events and excluding false positives by manual checking. This approach did result in a high rate of false positives, on average 55 % for wildtype tissue, but gave the highest data fidelity for subsequent analysis. It is worth noting that the fully manual detection carried out by Scott Curran gave the same qualitative results but with fewer events detected. In addition, I checked that the time point for the event, as identified by the algorithm, was consistent with when a four-way vertex was reached in the fluorescent images.

3.3 Fluorescence Intensity Measurements

We imaged myosin and junction dynamics using transgenic fly stocks expressing both Bazooka-mCherry and Sqh-GFP. Bazooka is a scaffold protein that localises to the apical junction and was used as an adherens juntion marker, instead of DE-cadherin [83]. Spaghetti-Squash (Sqh) encodes the myosin regulatory light chain (MRLC); it was fused to GFP and expressed in a Sqh null background in order to visualise total Myosin in the tissue [84]. It is possible to looks at phosporylated (active) Myosin II using fixed stains. However, the data included here is based on live-imaging of Sqh-GFP and we use this as a proxy for active Myosin II. As with the other experimental work, this was done by Scott Curran and is described in [Curran 2015].

To correlate Myosin II intensities with junction dynamics, I developed code to extract time series data for myosin on individual junctions. For each junction, I used the pixel coordinates from the segmented images to identify the junction in the fluorescent images. To include the fluorescence intensity across the width of the junction, I performed a morphological dilation to give each junction an average width of 5 pixels. This corresponds to a width of 500 nm, for the time-lapse imaging taken at 30 s intervals with a resolution of 0.1 μm/pixel, and a width of 430 nm for the time-lapse imaging taken at 5s intervals with a resolution of 0.086 μm/pixel. For comparison, Rauzi et al. used a width of 500 nm to quantify myosin intensity [54] [Supplementary material]. The fluorescent images, segmented images, and morpological dilation are shown for a single time point in Figure 3.5. The vertices tend to be the brightest regions in the image and including them would give rise to artefacts in the correlation functions - e.g. as junctions contract the vertices would make up a larger proportion of the junction resulting in an increase in the average intensity per pixel.

For each junction, I sum over the intensity of pixels within the region covered by the morphological dilation. There is a slight bleaching of the tissue over time, leading to a gradual decrease in intensity. I remove the trend associated with bleaching in the following way: for each time frame, I sum the total intensity for all pixels within the dilated junctions (I_{tot}) and calculate the total number of pixels p_{tot}. For each junction, the total intensity I_j, is normalized by I_{tot}/p_{tot}, such

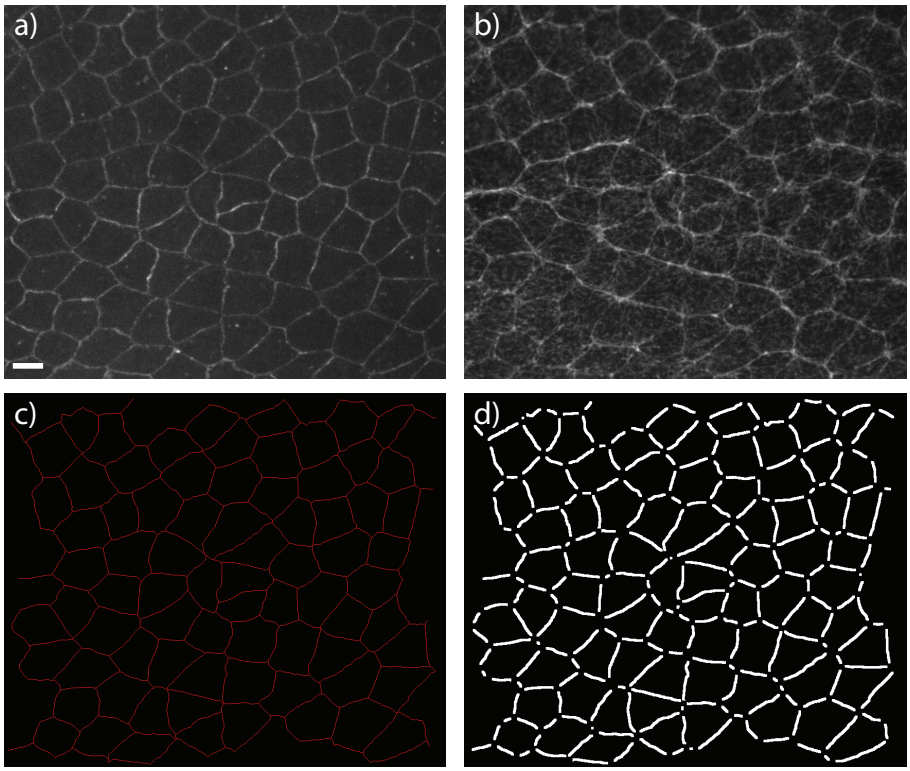

Figure 3.5: Fluorescence intensity for Myosin II and Bazooka

a) Notum imaged with Bazooka-mCherry, **b)** Notum imaged with Sqh-GFP to visualise the localisation of Myosin II in the tissue, **c)** Segmentated image, **d)** Morphological dilation of segmented junctions with vertices exclude. The resolution of the image is 0.085979 μm per pixel and the scale bar shown in panel a) is 5 μm long. Border junctions are excluded from the analysis of fluorescence intensities.

that the average intensity per pixel is one for every time frame $\sum_j I_j / \sum_j p_j = 1$. For each junction, I calculate the 'normalized average intensity' by taking the total intensity for a junction, normalizing it as described, then dividing by the number of pixels in the junction. Qualitatively, dividing by the number of pixels gives the same results as dividing by junction length.

For the analysis, myosin intensity is used as a proxy for myosin concentration. The relation between fluorescence intensity and concentration might be nonlinear and could depend on the properties of the microscope, including the resolution and light source. The 30 s interval Bazooka-mCherry and Sqh-GFP movie was imaged on a Zeiss 780 with a resolution of 0.1 μm/pixel, whereas the 5 s interval movie was imaged on a Carl Zeiss Axiovert 200 with a Yokogawa CSU-X confocal spinning disk unit and a resolution of 0.086 μm/pixel. The temporal dynamics of myosin (and bazooka) were consistent for the two movies, but the

mean and variance of the fluorescence intensity (prior to normalization) were significantly different. Hence, the absolute value of the fluorescence intensity is not a meaningful quantity in this context.

Chapter 4

Properties of neighbour exchange events in the notum

During development, cells in the *Drosophila* notum rearrange to form an ordered hexagonal array. We are interested in understanding how this order emerges from an initially disordered state in an effective and robust manner. Cell rearrangment in the notum is driven by junction remodelling and largely occurs in the absence of cell division, apoptosis and delamination. In this chapter, I characterize various properties of neighbour exhange events in order to investigate their role in the ordering process.

In the notum, there are two types of junction changes that contribute to ordering. First, the length of junctions fluctuate and gradually equalize, leading to cells with sides of equal length. Second, junction remodelling facilitates changes in cell neighbour configurations in the tissue. These neighbour exchange events proceed with a junction contracting to a four-way vertex, causing the contact between two neighbouring cells to be lost, followed by the formation of a new junction connecting two cells that were not previously adjacent [85, 86]. This allows cells to gain or lose an edge, which is essential for transitioning from a distribution of polygon shapes to a stereotyped set of hexagons. Our aim is to understand how these junctional changes are regulated and how they contribute to ordering in the tissue.

The current paradigm for studying junction remodelling and neighbour exchange events is germ-band extension, where neighbour exchange events are tightly coordinated to execute large-scale tissue morphogenesis [53, 56, 87, 88, 54]. By contrast the notum is static at the tissue level, but undergoes internal rearrangments as cell geometry and topology becomes more regular. We study

the notum at a point in developmental time, 12 h after pupariation (AP), where we do not observe cell divisions, cell delaminations or apoptosis - processes that may also contribute to ordering [89]. This allows us to isolate the effect of junction changes and investigate the stochastic nature of the tissue in the absence of force-generating events that bias the system. In this chapter, we demonstrate that neighbour exchange events are not associated with large-scale morphogenesis, unlike in germ-band extension. We observe that the junctions involved do not appear to be regulated in a stereotyped spatial or temporal manner. In fact, junction remodelling is frequenctly reversible. Taken together, the results give a detailed description of the properties of neighbour exchange events and sets the stage for exploring the role of stochastic fluctuations in the tissue.

4.1 Neighbour exchange events are not associated with large-scale morphogenetic changes

Firstly, we establish the premis that the region of the *Drosophila* notum we are studying is in fact static with respect to the size and shape of the tissue. Figure 4.1 shows a virtual clone at 12.0 h AP and again at 13.5 h AP. I tracked all cells within the clone to quantify changes in the total area and aspect ratio of that region of the tissue. The aspect ratio was found by calculating the horizontal distance between every point on the perimeter (excluding points less than one junction length from the bottom/top of the clone) and taking the mean to get a value for the length of the tissue (L), doing the same for the vertical distance to get the width (W), and then calculating the ratio of the length and width. The total area of the cells and the aspect ratio of the virtual clone are unchanged over a 90 min period. The data shown is for a single tissue, but the same analysis was carried out on four different nota and the observed behaviour was the same. In summary, our data show that no large-scale morphogenetic changes are occuring in the tissue.

However, from visual inspection of the tissue it is clear that junctions are dynamic and that remodelling of cell-cell connectivity occurs frequently. In the embryonic germ band, such junction remodelling drives tissue elongation in a

highly stereotyped manner. Why, then, does junction remodelling in the notum not give rise to tissue morphogenesis? In the following sections, we consider two hypotheses: (i) Neighbour exchange events cause local deformation of the tissue, but lack the spatial and orientational bias required for global morphogenesis; and (ii) Neighbour exchange events do not cause local deformation of the tissue.

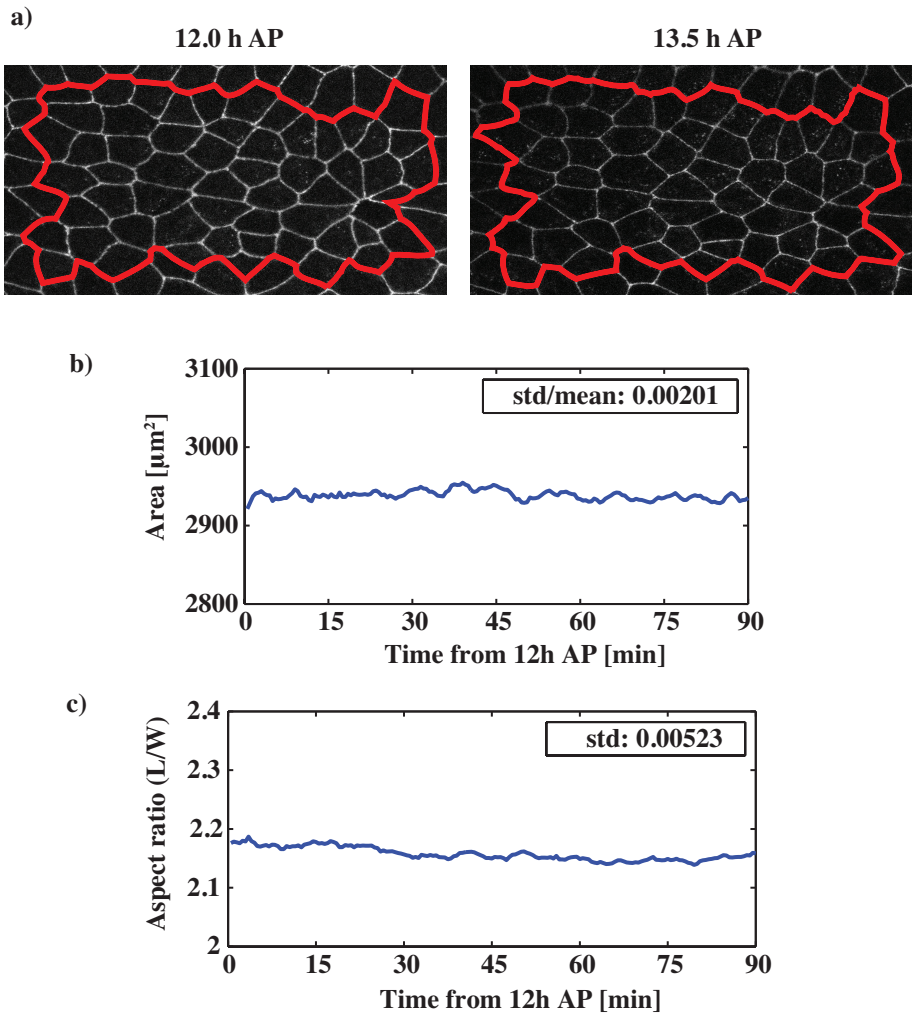

Figure 4.1: Tissue area and aspect ratio

a) Images of the fly notum at 12.0 h AP and 13.5 h AP. Red outlines show virtual clones of cells that remain in the frame over the 90 min period. No cell divisions, cell delaminations or apoptosis events occur. **b)** Total area for the cells within the red outline. The coefficient of variation (standard deviation over mean) is 0.00201. **c)** Aspect ratio, length divided by width, of the virtual clone. The data shown is for a single tissue, but is representative of the behaviour observed in four separate nota.

4.2 Neighbour exchange events vary in orientation and occur with no apparent spatial pattern

During germ-band elongation, junction remodelling is polarized and proceeds with junctions shrinking along the D-V axis and expanding along the A-P axis, causing the tissue to approximately double in length [53]. We are interested in whether such orientational bias is present for neighbour exhange events in the notum. The results are shown in Figure 4.2. Note that the number of T1 events included in each figure panel varies; some measurements require the junction to be observed before/after the event, thereby excluding events that occur at the start/end of the imaging period or in a part of the tissue that does not stay in the frame throughout.

I measured the angle of junctions undergoing neighbour exchange, defining the angle relative to the midline in the anti-clockwise direction. As junctions shrink down to a four-way vertex, angle measurements, whether taken from fluorescent images or segmented images, become unreliable and I therefore exclude the 5 min just before and after the neighbour exchange event from the analysis. Instead the mean angle is calculated for $t = [-15\ -5]$ min and $t = [5\ 15]$ min. The change in angle during a neighbour exchange event is narrowly distributed around 90 degrees (the mean is 87.9 ± 11.6 degrees), as expected.

For the histogram showing the orientation of junctions prior to neighbour exchange, the polarized junction remodelling in germ-band elongation would correspond to a peak around 90 degrees. Interestingly, in the notum, shrinking junctions appear to be predominantly oriented along one of the diagonals rather than the D-V axis. It is worth noting that for the tissue as a whole, the distribution of junction angles is not even and this is to be expected for polygon packing. In fact, in the case of hexagonal packing, only three junction angles would be represented: [30, 90, 150] or [0 60 120] depending on which of two possible packing configurations the cells are in. It is not clear what causes the observed distribution of the angle of T1 junctions (Fig. 4.2 d). Nonetheless, the results show that, in contrast to germ-band elongation, neighbour exchange events in the *Drosophila* notum are not polarized along a single orientation.

We also looked at how neighbour exchange events are spatially distributed in the tissue. Figure 4.2 a) shows an image of the tissue with all junctions that go through a neighbour exchange event (within a 90 min period) labelled by yellow arrows. The figure is representative of the four pupae imaged and shows that there is no apparent spatial pattern to the occurence of neighbour exchange events.

The lack of distinct orientational or spatial bias could explain why neighbour exchange events in the notum do not contribute to morphogenesis, as the cumulative effect of small local deformations could cancel out at the tissue level. It is also possible that neighbour exchange events do not actually cause local tissue deformation and we test this in the following sections.

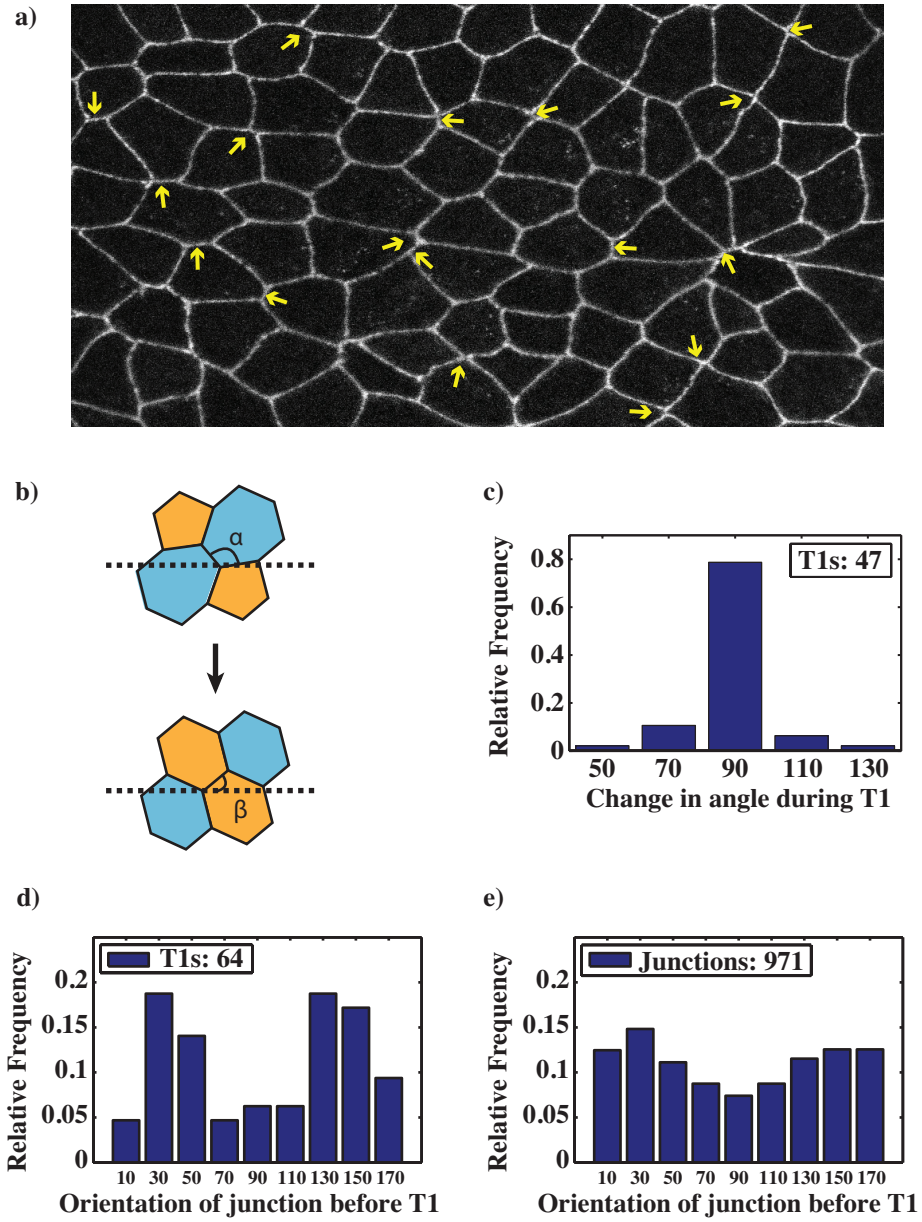

Figure 4.2: Spatial properties of T1 events in the tissue

a) Fly nota at 12.0 h AP, yellow arrows indicate junctions that undergo one or more T1 transitions in the following 90 min. **b)** Schematic showing the orientation of the junction undergoing a T1 event. The angle before the T1 event is α. The angle is measured relative to the midline in the anti-clockwise direction, i.e. 90 degrees is perpendicular to the midline. The change in angle for the junction shown in the schematic is $|\beta - \alpha|$. **c)** Histogram showing the change in angle during a T1 transition ($n = 47$ events). The mean is 87.9 ± 11.6 degrees. For each junction the angle is calculated from 15 min before the T1 event to 15 min after. The angle before is taken as the mean of the angle from $t = -15$ min to $t = -5$ min, and the angle after is taken as the mean from $t = 5$ min to $t = 15$ min, thereby excluding the 5 min before and after the junction shrinks to zero at the four-way vertex configuration. **d)** Distribution of angles for junctions undergoing a T1 transition ($n = 64$ events). The angle is taken as the mean from $t = -15$ min to $t = -5$ min. **e)** For comparison, the distribution of junction angles for all junctions in the tissue. The data is from four separate pupae.

4.3 Neighbour exchange events do not cause local tissue deformation

We want to directly test whether neighbour exchange events cause local deformation of the tissue. To do this, I measured the aspect ratio of the four-cell cluster involved in each event (Fig. 4.3). I compute the center of area (CoA) of each cell and define the internal aspect ratio as the distance between the CoA of cells losing an edge divided by that of the cells gaining an edge. For the external aspect ratio, I extend the axis between the CoAs to where it intersects with the perimeter.

$$\text{Internal AR} = \frac{\text{Distance between CoAs of cells losing an edge}}{\text{Distance between CoAs of cells gaining an edge}} \tag{4.1}$$

$$\text{External AR} = \frac{\text{Distance between perimeters of cells losing an edge}}{\text{Distance between perimeters of cells gaining an edge}} \tag{4.2}$$

This definition of the aspect ratio, means that an elongation of the four-cell cluster along the same axis as the expansion of the T1 junction, gives an increase in aspect ratio.

The internal aspect ratio shows the effect of junctional remodelling within the four-cell cluster. As shown in the left panels of Figure 4.3, the mean internal aspect ratio increases during a neighbour exchange event. The internal aspect ratios for individual clusters are compared, at -15 min and 15 min, using a paired t-test, giving $p < 0.0001$ (significant change). In fact, out of 33 clusters, only one shows a decrease in the internal aspect ratio. By contrast, there is no statistically significant change in the external aspect ratio ($p = 0.0502$). Hence, internal junction remodelling does not affect the perimeter of the four-cell cluster and does not induce local deformations in the tissue. Even if T1 events were oriented along the same axis, as is the case in germ-band elongation, the cumulative effect would not alter the shape of the tissue.

There are other methods for calculating the aspect ratio. Often one would fit an ellipse to the four-cell cluster and give the aspect ratio as the ratio of the major and minor axis. In our data, the proportion of clusters where the longest axis is aligned with the T1 junction, before remodelling, is 55%. These correspond to the

individual traces that start below 1 in the spaghetti plots in Figure 4.3. Therefore, this method would result in around half the ellipses being aligned with the T1 junction and around half being approximately perpendicular to it. Even if all clusters elongated along the axis of the T1 junction expansion, the change in aspect ratio could average to zero (it would be like inverting all the individual traces that start below zero in the spaghetti plot).

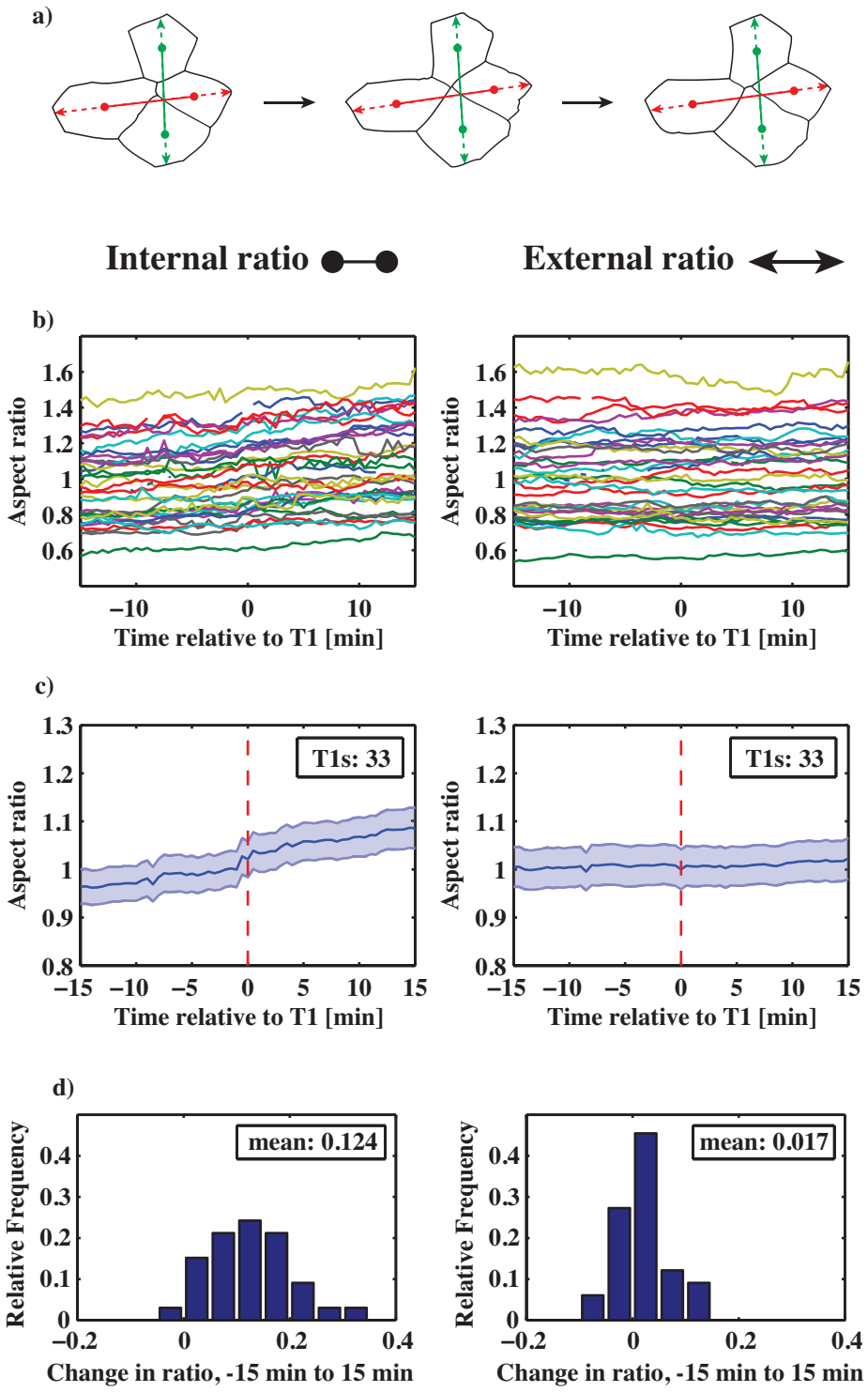

Figure 4.3: Internal and external aspect ratio of four-cell clusters in T1 events

a) Each T1 transition involves a four-cell cluster. The center of area of each cell (CoA, marked with a dot) is calculated. The internal aspect ratio is the distance between the CoAs of the cells losing a junction (red) divided by the distance between the CoAs of the cells gaining a junction (green). For the external aspect ratio, the axis between the CoAs is extended out and the distance between the perimeter intersections is calculated. For figures **b)-d)**, panels on the left are for the internal aspect ratio and panels on the right are for the external aspect ratio. **b)** Plots for the aspect ratio (left: internal, right: external) of each four-cell cluster undergoing a neighbour exchange event. **c)** Mean aspect ratio for 33 four-cell clusters. The errorbars shown are the standard error of the mean. **d)** Change in aspect ratio from $t = -15$ to $t = +15$. A paired t-test was used to compare the aspect ratios at $t = -15$ and $t = +15$. Internally, the aspect ratio changes during a T1 event ($p < 0.0001$). Externally, the change is not statistically significant ($p = 0.0502$). The data is from four separate pupae.

4.4 Neighbour exchange events are associated with a redistribution of apical area

Next, we investigate whether other geometrical properties of the cells involved in neighbour exchange events change in a stereotyped manner. Each neighbour exchange event involves a cluster of four cells and, for the analysis in Figure 4.4, the cells are grouped according to whether they gain or lose an edge during the event.

Following cells from 15 min before to 15 min after a neighbour exchange event, we observe an increase in apical area for cells losing an edge and a corresponding decrease for cells gaining an edge. However, the effect is small and it is worth noting that the cells gaining an edge do not, on average, start out smaller than the cells losing one. The redistribution of apical cell area observed during a neighbour exchange event (Fig. 4.4) is consistent with the results for the aspect ratio of four-cell clusters during the event. In order for the internal junction remodelling to occur without a concomittant change in the outer perimeter of the cluster, it must be associated with a redistribution of apical cell area.

For the polygon distributions of cells involved in neighbour exchange, we found that cells gaining an edge have, on average, one edge fewer than the cells losing one. In Chapter 6, I include a more detailed analysis of the ordering of polygons in the tissue.

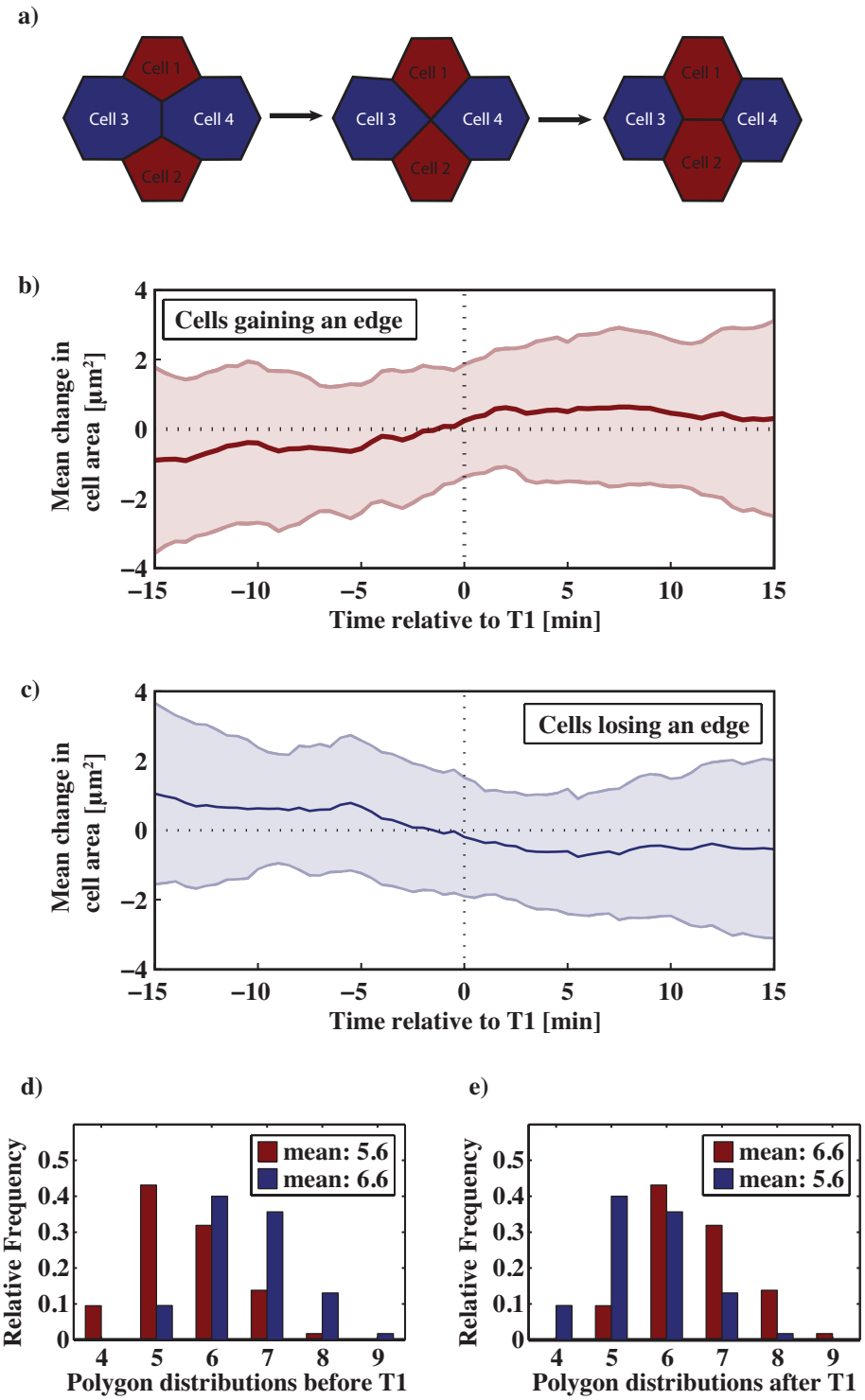

Figure 4.4: Change in cell area and number of edges during T1 events

a) Cells gaining an edge (Cell 1 and 2) are shown in red in the schematic and throughout the figure, cells losing and edge (Cell 3 and 4) are shown in blue throughout the figure. **b)** Mean cell area for cells gaining an edge ($n = 77$ cells) from 15 min before to 15 min after a T1 event. At $t = 0$, the configuration is that of a four-way vertex. For each cell, the mean cell area has been subtracted from the time series before the population mean was calculated. The errorbars shown are the standard deviations. **c)** As in b), but for cells losing an edge ($n = 77$ cells). **d)** Polygon distributions for cells gaining (red) and losing (blue) an edge 15 min before a T1 transition. **e)** Corresponding polygon distributions 15 min after a T1 transition. Cells on the border of the frame are not included in the analysis.

4.5 Neighbour exchange events are temporally random

In the previous section, we established that neighbour exchange events do not show any distinct spatial or orientational bias within the tissue, suggesting that the events could be random processes. To explore this further, we consider the temporal pattern of neighbour exchange events.

Figure 4.5 a) shows the cumulative T1 count, normalized by the number of junctions in the tissue, for each of the four nota. Interestingly, the cumulative count increases approximately linearly with time, indicating that the rate of neighbour exchange events is constant in time. In addition, the rate at which neighbour exchange events occur is consistent across different nota.

I extended this analysis to directly compare the temporal distribution of neighbour exchange events to a Poisson process. A Poisson process is a random process used to describe events that are stochastically independent and occur continously in time. Systems that can be modelled as a poisson process include the radioactive decay of atoms and the arrival of customers in a queue. The process is described by the parameter λ, which is the average rate of events per unit time (in t units of time, there are, on average, λt occurences). If λ is constant, the process is refered to as a stationary Poisson process.

The Poisson distribution, $P(n)$, gives the probability that n events occur in t units of time. It follows that the probability of no events occuring in a time t is $P(n = 0)$ and that this is equivalent to the probability that the time T until the first occurence is larger than t.

$$P(n) = \frac{e^{-\lambda t}(\lambda t)^n}{n!} \tag{4.3}$$

$$P(T > t) = P(n = 0) = e^{-\lambda t} \quad \Rightarrow \tag{4.4}$$

$$P(T \leq t) = 1 - P(n = 0) = 1 - e^{-\lambda t} \tag{4.5}$$

To compare the temporal pattern of neighbour exchange events to a Poisson process, I examined the time intervals between consecutive events in the tissue. For a Poisson process, the inter-event times $f(t)$ are exponentially distributed,

specifically:

$$f(t) = \lambda e^{-\lambda t} \quad \text{for} \quad t \geq 0 \tag{4.6}$$

Figure 4.5 b), shows the experimentally observed distribution of inter-event times, together with a fitted exponential function. The parameter λ is $1/5.9$ min^{-1}, i.e. in a tissue similar in size to the four nota studied here, there is, on average, one neighour exchange event every 5.9 min. Visually, the distribution of intervals resembles the probability density function of the exponential distribution. However, the Lilliefors statistical test gives $p = 0.0127$ when testing the hypothesis that the data is consistent with an exponential distribution, indicating that we cannot decisively accept or reject the hypothesis.

Overall, it appears that neighbour exchange events are occuring somewhat randomly within the tissue, both in time and space. This raises the interesting hypothesis that neighbour exchange events in the notum may not be highly regulated processes, the way they are in germ-band elongation, but could result from of an underlying stochastic process. We will return to this idea in the following chapter.

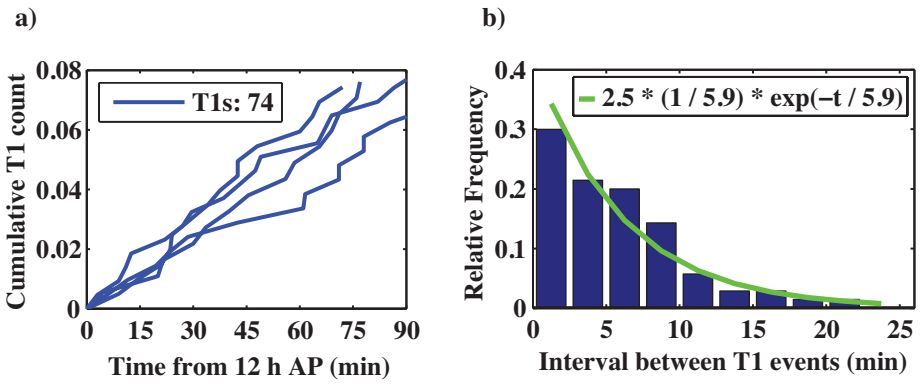

Figure 4.5: Temporal distribution of T1 events in the tissue

a) Cumulative T1 count, normalized by the number of junctions within the frame, for four different nota. In total 74 T1s were detected and analyzed. **b)** Histogram showing the relative frequency of the time interval between successive T1 events. An exponential distribution of the form $\lambda * \exp(-\lambda t)$, with $\lambda = 1/5.9$ min^{-1}, was fitted to the data - the green line shows the exponential scaled by a factor 2.5 (the binsize) to fit the histogram. The Lilliefors test returns $p = 0.0127$ for the hypothesis that the data for the interval times comes from an exponential distribution.

4.6 Neighbour exchange events are reversible

In germ-band elongation, neighbour exchange events have been found to be strictly irreversible [53]. Since neighbour exchange events in the notum appear to be stochastic, with no clear spatial or temporal pattern, we expect that they they might also be reversible. To test this, I directly calculated the reversibility of neighbour exchange event using our time-lapse imaging data.

When tracking junctions across frames, we assign a junction the same ID before and after junction remodelling. One could argue that neighbour exchange creates a new junction, yet this way of assigning IDs allows us to quantify to what extent the events are reversible. In four wildtype nota we observed a total of 74 neighbour exchange events. Out of 984 junctions, 61 went through at least one transitions. For 11 of these junctions we observed two or more transitions within the period of time we imaged for, demonstrating that in the *Drosophila* notum neighbour exchange events are reversible.

In order to estimate the probability of reversing, I use the Kaplan-Meier method to calculate survival functions for neighbour exchange events. In medical research [90], the Kaplan-Meier estimator is a common tool for quantifying survival times of patients following treatment. In this context, survival does not have to refer to life/death, but can be any event of interest. The strength of the method is that it takes into account if patients are lost to follow-up (e.g. if they drop out) or if a study ends before the event being studied has occured. In these cases, survival times are described as 'censored'. If no censoring is present in the data, the Kaplan-Meier curve is the complement of the empirical cumulative distribution function.

The Kaplan-Meier method is the right tool for analysing the reversibility of neighbour exchange events since it allows us to combine data from movies of different lengths and to take into account that a neighbour exchange event at the start of a movie is observed for longer than one occuring towards the end. Here, neighbour exchange events that have not reversed by the end of the movie are 'censored', as it is not possible to determine how long the cell neighbour configuration would have persisted if we had continued imaging. The survival

curve $S(t)$ is shown in Figure 4.6 b) and is defined as the probability that a neighbour exchange configuration persists, without reverting back, for at least a time t. In the figure, the time points at which events are censored are marked by black crosses. From the survival curve, the probability that a configuration persists for at least 150 min following junction remodelling, is 69%, and this number would likely be even lower if we imaged for longer. Hence, neighbour exchange events in the notum are highly reversible.

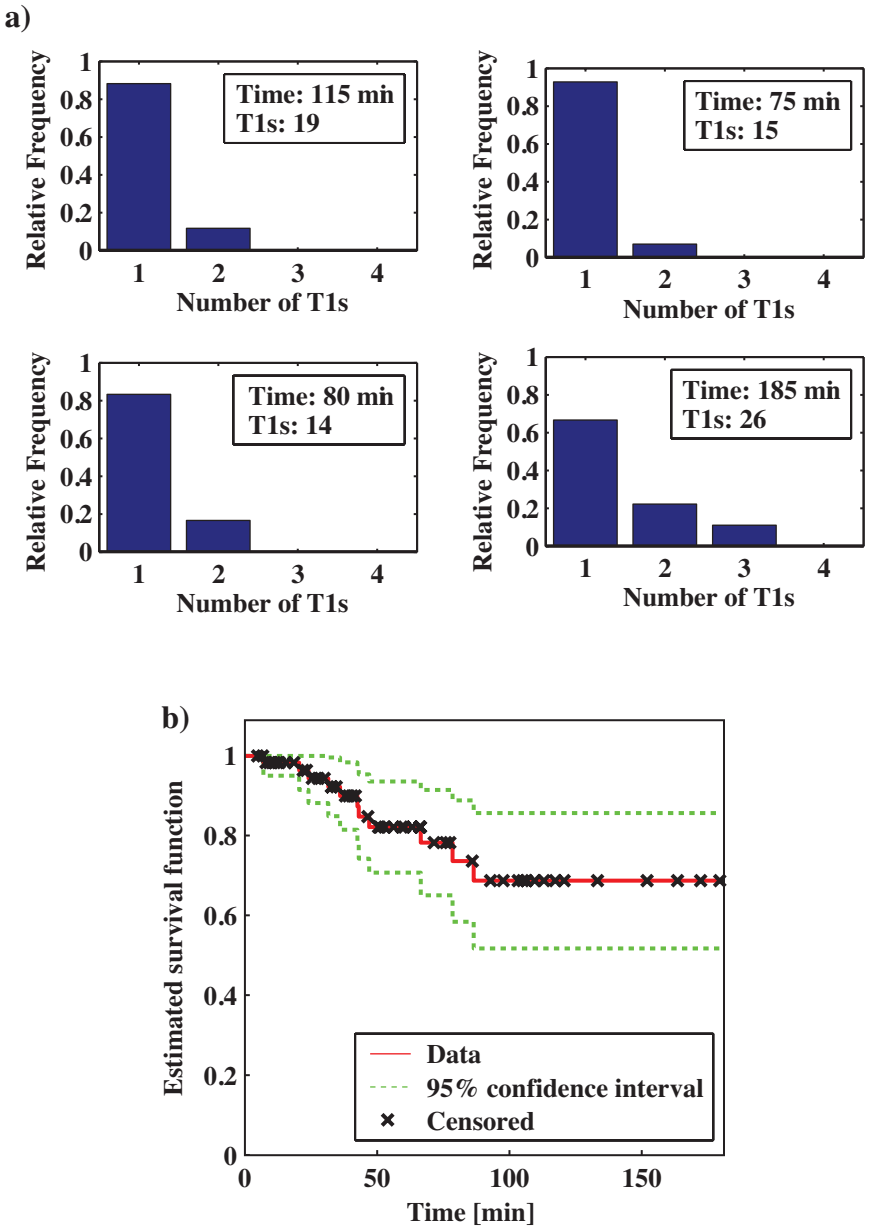

Figure 4.6: Reversibility of neighbour exchange events

a) Bar charts showing what proportion of junctions undergo unidirectional (one), bidirectional (two), and multidirectional (three) neighbour exchange events. The data is from time-lapse imaging of four wildtype nota over 115, 75, 80, and 185 min, respectively. **b)** Kaplan-Meier survival curve showing the probability that a neighbour exchange configuration persists for a given length of time. Events are 'censored' if the reverse transition has not occurred by the end of the movie. The 95% confidence intervals are estimated using Greenwood's Formula. The probability of a configuration persisting for at least 150 min, along with the 95% confidence interval, is: 0.687 [0.5175 0.8567].

4.7 Total junction length is unchanged during neighbour exchange events

We are interested in understanding the mechanics of junction remodelling, i.e. what happens to junctional material as cells change neighbours. Figure 4.7 shows that, on average, total junction length is constant during neighbour exchange. As the T1 junction contracts, the four neighbouring junctions expand, leaving the total length of the system unchanged. This leaves two possible models: (i) Neighbour exchange occurs without turnover of junctional material. Instead, contraction/expansion is acheived by vertices 'sliding' relative to the junction. (ii) Removal and addition of junctional material balances within the five junctions such that total junction length is conserved. We tested these models using a temperature sensitive *shibire* mutant line in which endocytosis of DE-cadherin is blocked [91]. We found that blocking endocytosis does not prevent junction remodelling, but does reduce the frequency of events. This shows that turnover of junctional material is not required for neighbour exchange, but does facilitate the junction remodelling involved (see [Curran 2015] for more details).

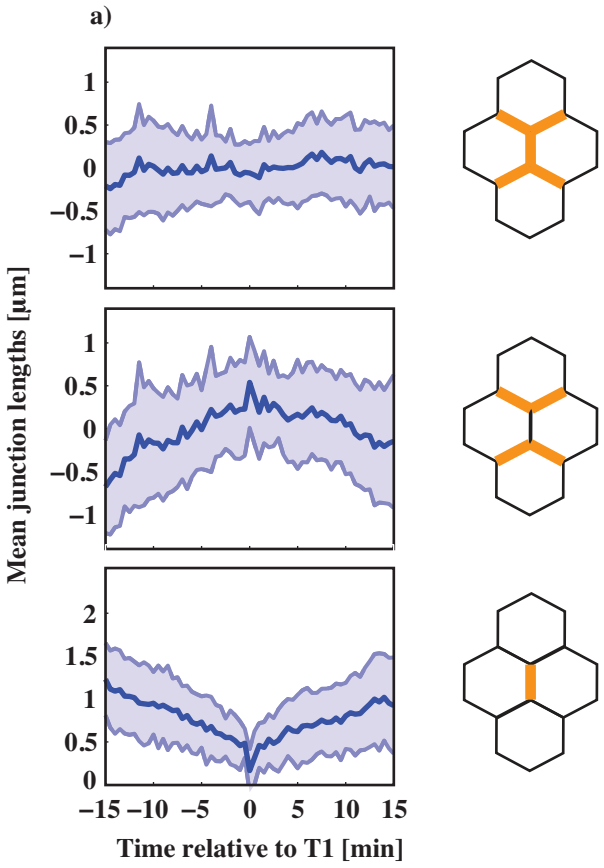

Figure 4.7: Junction length changes during T1 events

a) Average change in junction length during a T1 event ($n = 27$ events, from 4 nota) for wildtype tissue. The schematics on the right highlight which junctions are plotted in each panel, (top) all five junctions involved, (middle) the four neighbouring junctions, (bottom) the T1 junction. For each event, the junction length time series have been aligned with the four-way vertex configuration occuring at $t = 0$.

4.8 Discussion

Taken together, the results in this section demonstrate that neighbour exchange events in the *Drosophila* notum - a tissue that is not undergoing growth and directed morphogenesis - differ in several qualitative ways from what has been observed in germ-band elongation.

In germ-band elongation, neighbour exchange events are strictly irreversible [53] and proceed with a definite orientation, shrinking along the D-V axis and expanding along the A-P axis. By contrast, we observed that junction remodelling in the notum is often bidirectional, with the same junction undergoing several consecutive transitions. We also found that neighbour exchange events are distributed in a spatially random pattern within the tissue and shrinking junctions are not predominantly oriented along the D-V axis.

We investigated how neighbour exchange events can occur without giving rise to any large-scale deformation of the tissue. Junction remodelling does change the internal distances between centroids in the four cells involved and is associated with a redistribution of apical area. However, this does not affect the aspect ratio of the outer perimeter of the four-cell cluster. Hence, even if neighbour exchange events were all oriented along the same axis, as is the case in germ-band elongation, the cumulative effect would not reshape the tissue.

We also studied the temporal distribution of neighbour exchange events and found that the cumulative T1 count increases linearly, indicating that the rate of events is stable over time. The intervals between consecutive T1 events resemble an exponential distribution and we cannot reject the hypothesis that the data is consistent with an underlying Poisson process. This motivates a further exploration of the stochastic nature of junction fluctuations in general and junction remodelling in particular. And this will be our focus in the next section.

Studying junction remodelling in the absence of force-generating cellular events, such as division and delamination events, allows us to investigate the fundamental characteristics of neighbour exchange events. In that respect, junction remodelling in the presence of a polarized distribution of Myosin II may be considered to be a special case. In fact, neighbour exchange events in the

Drosophila notum has some similarities with the phenotype observed in the germ-band when the activity of the gap gene *Krüppel (Kr)* has been eliminated by RNA-mediated interference (RNAi). In Kr(RNAi) embryos, the planar polarized localization of Myosin II is lost, junction remodelling is reduced and transitions are no longer irreversible, resulting in incomplete elongation of the germ-band [53, 54]. *Kr* mutant embryos display the same defective polarized cell intercalation [92]. Hence, disruption of the polarized action of Myosin II results in neighbour exchange dynamics more similar to what we observe in the notum.

Chapter 5

Stochastic Fluctuations of Junctions

In the previous section we observed that the intervals between consecutive neighbour exchange events are similar to what would be expected if the data were generated by a Poisson process. This motivates a further study of the stochastic nature of junction fluctuations and how they relate to neighbour exchange events. Looking at the time series for junction lengths in the tissue, shown in Figure 5.1, two things are worth noting. Firstly, junctions are dynamic and display stochastic fluctuations in length. Secondly, the magnitude of such fluctuations is similar to the periods of contraction and expansion observed during neighbour exchange events. This anecdotal observation, motivated us to look carefully at junction fluctuations going into and coming out of the four-way vertex during neighbour exchange. In this chapter, I examine the hypothesis that contraction and expansion in junction remodelling is a consequence of the general stochastic fluctuations of junctions in the tissue, as opposed to being an explicitly regulated and stereotyped process.

5.1 Junction length fluctuations resemble a random walk process

In one dimension, a random walk consists of a succesion of uncorrelated steps. The direction of movement in each step is completely independent of the path history and the process is consequently Markovian with respect to position [93, 94]. Note, that by analysing junction lengths, the two-dimensional motion of vertices reduces down to one-dimensional length changes.

One metric for describing a random walk is the distribution of persistence lengths. Persistence length is defined as the distance travelled before switching direction - i.e. the change in junction length during each period of contraction and expansion. To extract this information from the data, the time series is filtered using a moving average Hanning window. This is a low-pass digital filter, defined by the window function $w(n)$, where N is the width in terms of time points (Eq. 5.1).

$$w(n) = 0.5\,(1 - \cos\,(2\pi n/(N-1))) \quad n \in [0, N-1] \tag{5.1}$$

Segment boundaries are placed where the first derivative of the filtered time series changes sign or is zero and takes opposite signs on either side. This is shown in the top panel in Figure 5.2. The calculation of the persistence lengths is based on the raw time series - the filter is only used to establish the position of segment boundaries.

In the case of a one-dimensional random walk, which is our starting hypothesis for the behaviour of junctions on short time scales, the persistence lengths follow an exponential distribution. Figure 5.2 shows the distribution of persistence lengths, from 60737 segments, along with an exponential function of the form $1/\tau \exp(-t/\tau)$. The parameter is $\tau = 0.197$ μm. There is reasonable agreement between the data and the fit. However, the distribution does skew left relative to the exponential and, with $p = 0.001$, the Lilliefors test confirms that the data is not consistent with a simple random walk. This suggest that the dynamics of junction fluctuations might be better described by a constrained random walk. Indeed, based on physical constraints (cells cannot become arbitrarily large), some form of mean-reverting behaviour would be expected.

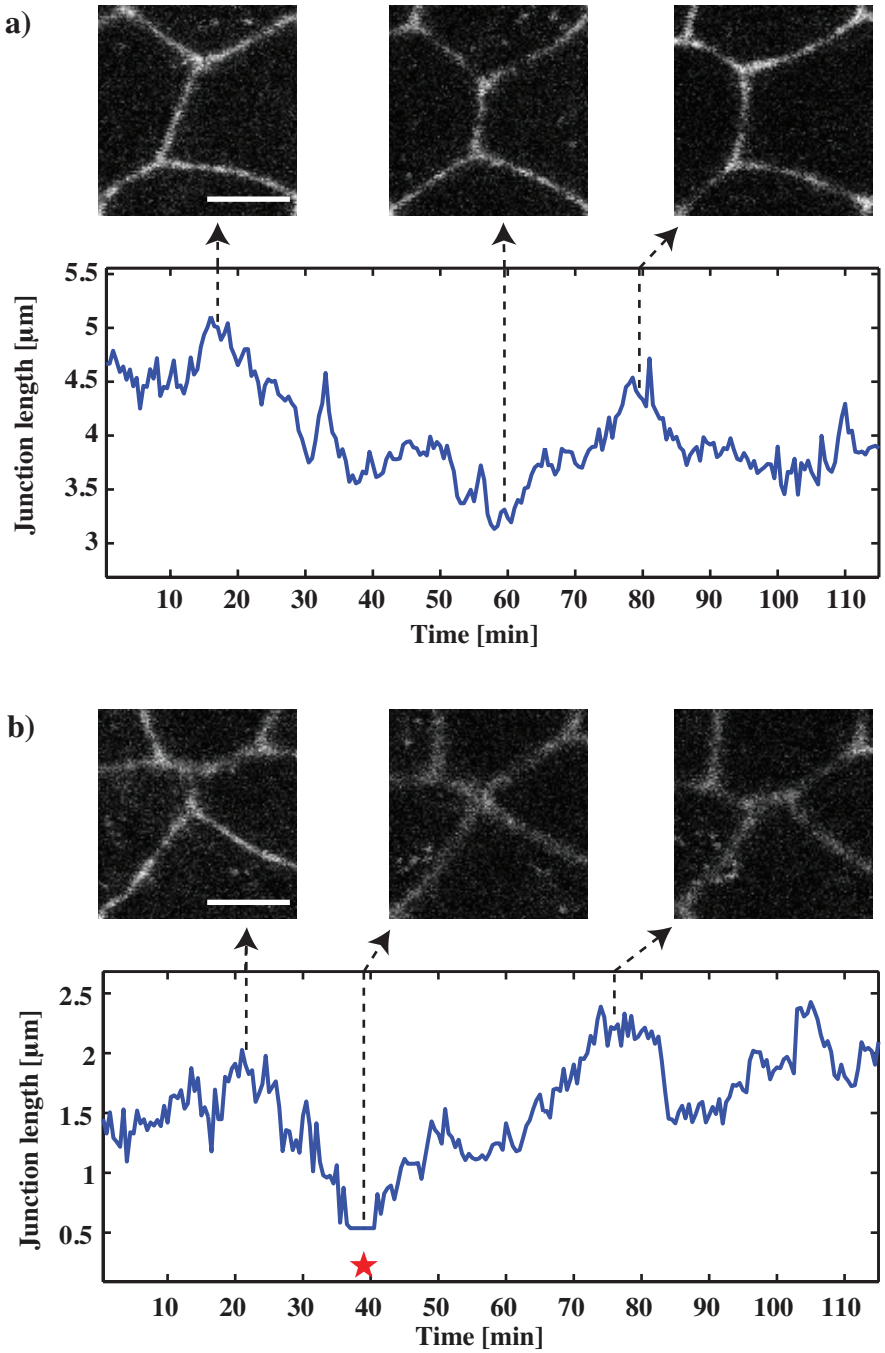

Figure 5.1: Junction length time series for T1 and non-T1

a) Time series for a junction not undergoing neighbour exchange. The corresponding fluorescent image of the junction is shown for three time points. Scale bar = 5 µm. **b)** Time series for a junction undergoing neighbour exchange. The point where a four-way vertex configuration is reached, is marked by a red star. The corresponding fluorescent image of the junction is shown for three time points. Scale bar = 5 µm. The scale on the y-axis is the same for both figures.

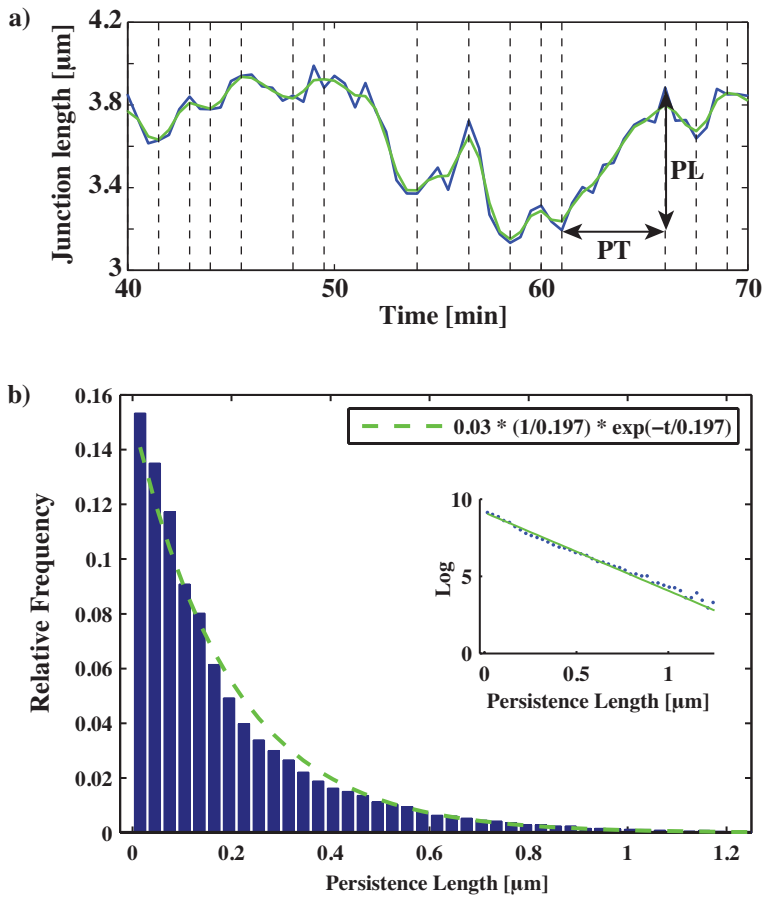

Figure 5.2: Distribution for persistence length

a) Time series for a junction length. The data have been filtered using a moving average Hanning window, with a filter setting of 5, and split into segments where the junction is contracting or expanding. The persistence time (PT) and persistence length (PL) are defined as the duration of a segment and the change in junction length, respectively. **b)** Histogram showing the relative frequency of persistence lengths for a filter setting of 5. $N = 60737$ segments, 4 nota. (green line) Best fit for an exponential function of the form $1/\tau \exp(-t/\tau)$. The parameter is $\tau = 0.197$ µm, with confidence bounds $[0.1958\ 0.1989]$. The function has been scaled by a factor 0.03 (the binsize) to fit the histogram. (inset) Number of segments in each bin of the histogram plotted on semi-log along with the exponetial fit.

5.2 The mean squre displacement curve for junction fluctuations shows subdiffusive behaviour

Another way of quantifying the dynamics of junction fluctuations is mean square displacement (MSD) analysis. This is a common method for characterizing stochastic processes, such as the diffusion of single molecules [95, 96, 97]. The mean square displacement $f(\tau)$ is a two-point correlation function and is given by:

$$f(\tau) = \langle (l(t+\tau) - l(t))^2 \rangle_t. \tag{5.2}$$

Here $l(t+\tau) - l(t)$ is the change in junction length (usually the displacement of the particle) between time t and $t+\tau$. The average is over the whole time series. Figure 5.3 shows how the mean square displacement curve is calculated for a single junction in the tissue.

In the case of pure diffusive motion, the mean square displacement scales linearly with the lag time τ and the diffusion coefficient may be read off the slope, with the prefactor depending on the dimensionality of the system. In one dimension:

$$f(\tau) = 2D\tau. \tag{5.3}$$

For different diffusion regimes, the MSD curve may exhibit more complicated behaviour. For subdiffusive and superdiffusive processes the MSD curves downwards/upwards and can be described by a powerlaw $\sim \tau^{\alpha}$.

Figure 5.4 shows the ensemble-averaged MSD curve, i.e. the average curve for all junctions in the four embryos we have data for. The behaviour is subdiffusive, in agreement with the results of the previous section. This suggests that junction fluctuations are constrained and mean-reverting.

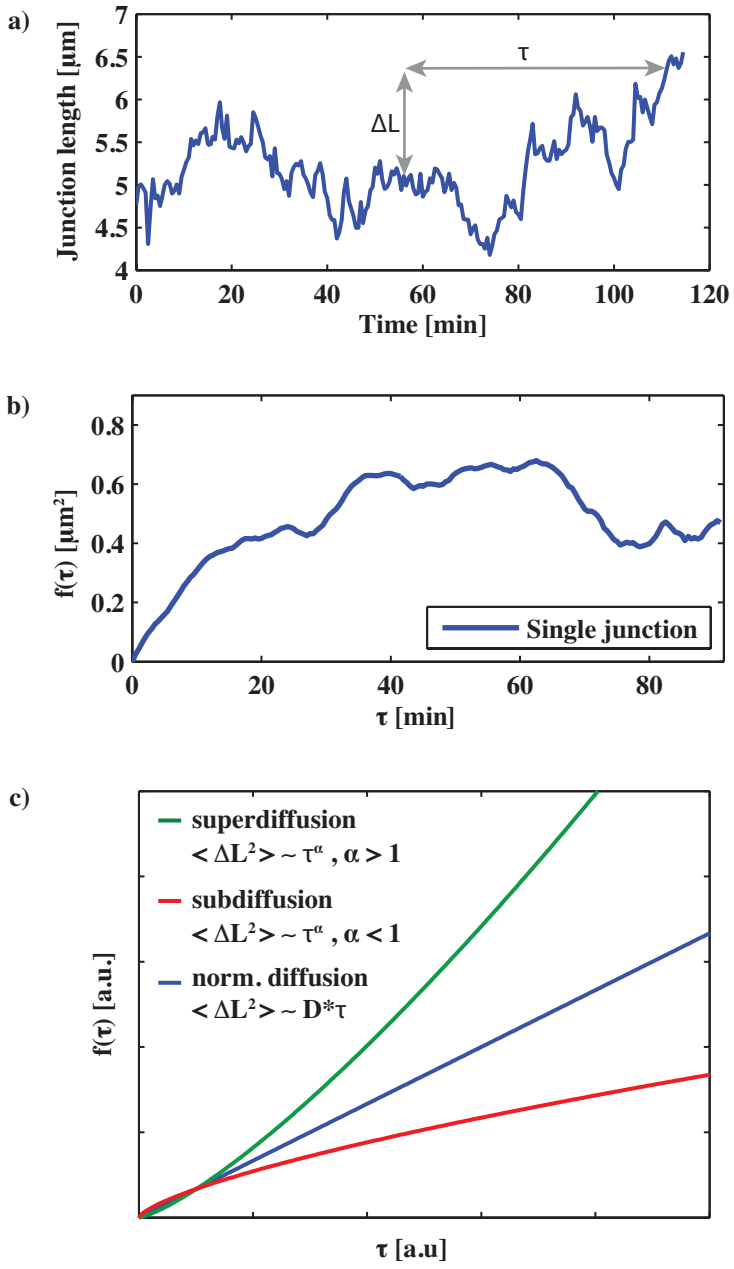

Figure 5.3: Schematic for mean square displacement

a) Time series for the junction length of a single junction in the notum at 12h. **b)** Mean square displacement for the junction shown above. The MSD for this junction saturates, but that is not representative of the range of behaviours observed. **c)** Plot of the MSD, in arbitrary units, for different diffusion regimes. For normal diffusion (blue), the MSD is a linear function of time, $\sim D * lag$, and the diffusion coefficient may be read off the slope (with a prefactor depending on dimensionality). For superdiffusive (green) and subdiffusive (red) processes, the MSD curves upwards/downwards and is described by a power-law $\sim lag^{\alpha}$.

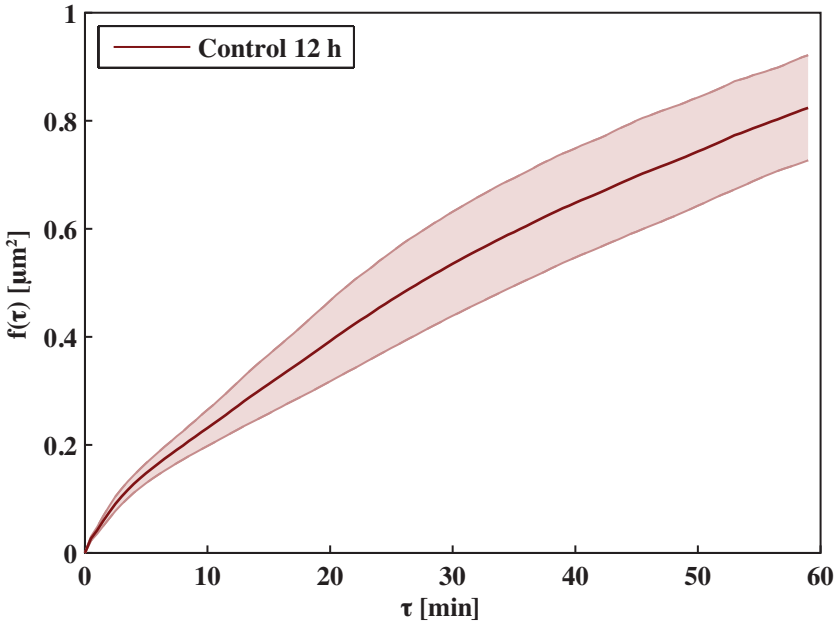

Figure 5.4: Ensemble-averaged mean sqaure displacement curve for junction fluctuations

Ensemble-averaged MSD curve ($N = 4$ nota). The ensemble-mean is calculated for each notum separately, then the average for each tissue type is calculated. The errorbars shown are the standard deviation of the ensemble-means for different nota.

5.3 There is no significant difference between the persistence length distributions of T1 and non-T1 junctions

Having established that junction fluctuations are stochastic, we are interested in what role such fluctuations play in neighbour exchange events. Anecdotal evidence, such as the time series of a T1 and non-T1 junction in Figure 5.1, suggests that junction fluctuations in the tissue display contraction and expansion events of a similar magnitude as those observed during junction remodelling. Our hypothesis, then, is that neighbour exchange events are a consequence of stochastic fluctuations that occasionally generate a four-way vertex configuration, as oppose to the scenario where junctions undergo directed contraction and expansion to perform neighbour exchange, even if they otherwise fluctuate randomly. In this section, I develop a rigourous method for testing this hypothesis.

The approach I take is to separate the time series for junction length fluctuations into segments where the junction is monotonically expanding or contracting, using the method described in the previous section. I then identify the segments associated with neighbour exchange events - these are the segments on either side of the time point at which the junction is at a four-way vertex and will be refered to as 'T1 segments'. This allows me to compare the properties of T1 and non-T1 segments in a rigourous way using appropriate statistical tests.

Figure 5.5 shows the time series for a junction going through a neighbour exchange event and reaching a four-way vertex around 40 min into the movie. The T1 event is marked by a red star and the T1 segments are demarcated by red dotted lines. Given the difficulty in determining a definite time for onset and completion of a T1 event, it is necessary to carry out the analysis and statistical tests for different levels of filtering. In Figure 5.2, the filter level was set such that it removed segmentation errors, but otherwise followed the raw time series closely. Applying that level of filtering for comparing T1 and non-T1 events, would not be a fair test. Even if T1 transitions are distinct events, contraction and expansion could occur in a stepwise fashion. In fact, in germ-band elongation the length change for junctions oriented along the D-V axis has been shown to

occur through successive steps of shrinkage and arrest [54]. Hence, a low level of filtering could underestimate the duration of neighbour exchange events.

Figure 5.6 shows the persistence length distributions for T1 and non-T1 junctions separately, using the same filter settings as shown in Figure 5.5. Note that, increasing the filter settings and introducing a minimal threshold for the size of segments, shifts the distribution of persistence lengths such that it displays a peak at a non-zero value. The number of segments included in each distribution are listed in Table 5.1. The first and last segment of each time series has been excluded from the analysis, since the actual duration cannot be determined. Higher levels of filtering results in longer, and therefore fewer, segments. Differences in the number of T1 segments come from T1 events occuring in the first or last segment and therefore being excluded from the analysis.

I use a two-sample Kolmogorov-Smirnov test to compare the distributions for T1 and non-T1 segments. It is a nonparametric hypothesis test and it does not assume that the data are from any particularly distribution (Gaussian or otherwise). It is, however, not valid if the underlying distribution is discrete. The test evaluates the difference between the cumulative distribution functions (CDFs) of the two samples and hence tests for any difference, including median, variance and shape of the distribution. The null hypothesis (H_0) is that the samples are drawn from the same underlying distribution and is rejected if $p < 0.05$. The analysis was carried out for a total of seven different levels of filtering, between 10 and 40, and the results are presented in Table 8.1. In every case the statistical test supports the null hypothesis, indicating that - at least in terms of persistence length - there is no difference between the contraction/expansion giving rise to neighbour exchange events and the ubiquitous stochastic fluctuations of junctions.

In addition to analyzing the persistence lengths, we can quantify the persistence time of junction fluctuations. As shown in Figure 5.2, the persistence time is given by the duration of each period of contraction or expansion. In the case of a random walk with constant step size, the persistence length is simply the persistence time multiplied by the step size. Note, that during neighbour exchange events, we often observe pausing in the four-way vertex configuration. The persistence length is robust to this phenomenon (since there is zero length

change during pausing), but it would lead us to overestimate the persistence time for these junctions. For this reason, the pause times have been detected computationally and subtracted from the persistence times for T1 segments.

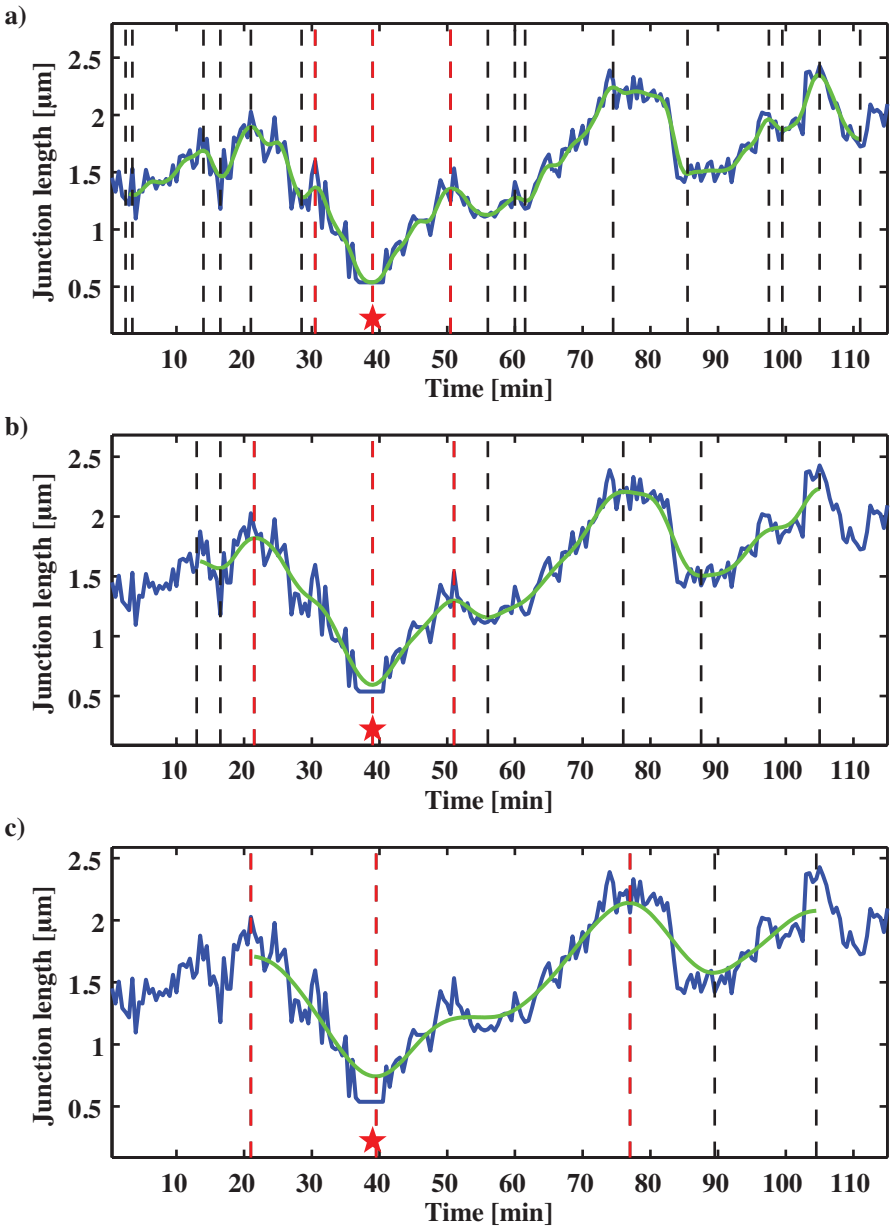

Figure 5.5: Filtering of junction length time series

The figure shows the junction length over time for a junction that undergoes at T1 event around 40 min into the movie (marked by a red star). The time series has been split into segments where the junction length is monotonically increasing or decreasing. This was done by filtering the data using a moving average Hanning window - if the first derivative changes sign or is zero with opposite signs on either side of that point, a segment boundary is placed. Using a higher setting for the filter, results in fewer segments. The filter settings used are a) 10, b) 20, c) 40. The analysis is done using the raw data - the filter is only used to establish the position of the segment boundaries. The segments on either side of the T1 event (marked with red dotted lines) are defined as T1-segments.

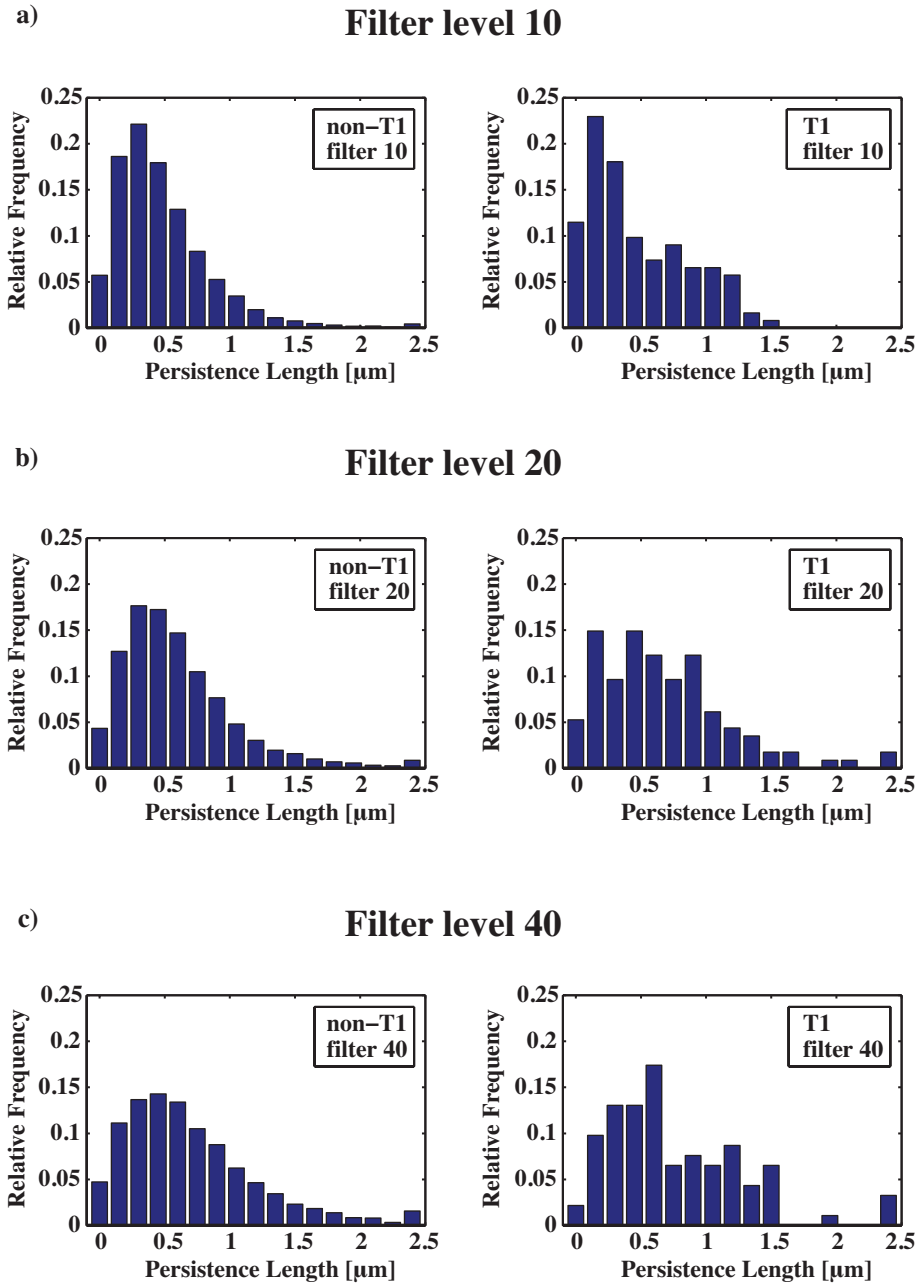

Figure 5.6: Persistence lengths

Persistence length distributions for (left) non-T1 and (right) T1 segments. The filter settings used are a) 10, b) 20, c) 40, as shown in Figure 5.5. The number of segments included in each histogram, are listed in Table 5.1. The distributions for T1 and non-T1 segments are compared used a two-sample Kolmogorov-Smirnov test. The p-values are listed in Table 8.1 and in every case the statistical test, at the 0.05 significance level, supports the null hypothesis that the samples are drawn from the same underlying distribution.

Filter level	segments non-T1	segments T1
10	22819	122
20	11377	114
40	4895	92

Table 5.1: Number of segments included in each of the persistence length distributions shown in Figure 5.6. Higher levels of filtering results in longer, and therefore fewer, segments. The first and last segment of each time series is excluded from the analysis, regardless of whether a T1 event occurs, therefore the number of T1 segments included can vary with filter level.

Filter level	p-value	Hypothesis
10	$p = 0.5142$	H_0
15	$p = 0.2727$	H_0
20	$p = 0.5294$	H_0
25	$p = 0.2569$	H_0
30	$p = 0.1081$	H_0
35	$p = 0.1881$	H_0
40	$p = 0.2572$	H_0

Table 5.2: The persistence length distributions for T1 and non-T1 segments are compared using a two-sample Kolmogorov-Smirnov test. The null hypothesis, H_0, is that the samples are drawn from the same underlying distribution. The analysis was carried out for seven different levels of filtering, between 10 and 40, and in every case the statistical test supports the null hypothesis at the 0.05 significance level. Note that, since we are testing a set of statistical inferences simultaneously, the appropriate significance level for the individual hypothesis tests is lower than the significance level for the set as a whole. Using the Bonferroni correction, we would get $\hat{\alpha} = \alpha/k = 0.05/7 = 0.007$. Since the p-values are all above 0.05, this is not something we need to worry about.

5.4 Contraction and expansion is symmetric in neighbour exchange

We have established that junction length changes during neighbour exchange events are indistinguishable from the general fluctuations of junctions in the tissue. As an additional test, we separate the contraction and expansion phases of junction remodelling. It is possible that, say, expansion is the result of junction fluctuations, while contraction occurs in a directed manner, and that grouping the processes together obscures this difference.

First, we consider the ballistic velocity of junction fluctuations - this is the persistence length divided by persistence time and gives the average rate of contraction/expansion for each segment. The results are presented as boxplots in Figure 5.7. The median contraction rate for T1 junctions is 0.81 ± 0.097 μm/min. Interestingly, this is consistent with the value of 0.83 μm/min reported for germ-band elongation [57]. According to the Kolmogorov-Smirnov test, there is no statistically significant difference between the ballistic velocities of T1 and non-T1 segments, in agreement with our results from the previous section.

I then repeated the analysis, but grouped segments according to whether the junction is contracting or expanding and analysed these separately. Based on the Kolmogorov-Smirnov test, there is no significant difference in the rate of contraction and expansion, both for non-T1 fluctuations and T1 events. Similarly, I found no significant difference in the persistence lengths of contracting and expanding segments, both for non-T1 fluctuations and T1 events.

The results show that, at least phenomenologically, neighbour exchange events are symmetric. In particular, the rate of contraction and expansion is the same, going into and coming out of a four-way vertex. This is in agreement with our previous result, in Figure 4.7, for the average change in junction length during neighbour exchange.

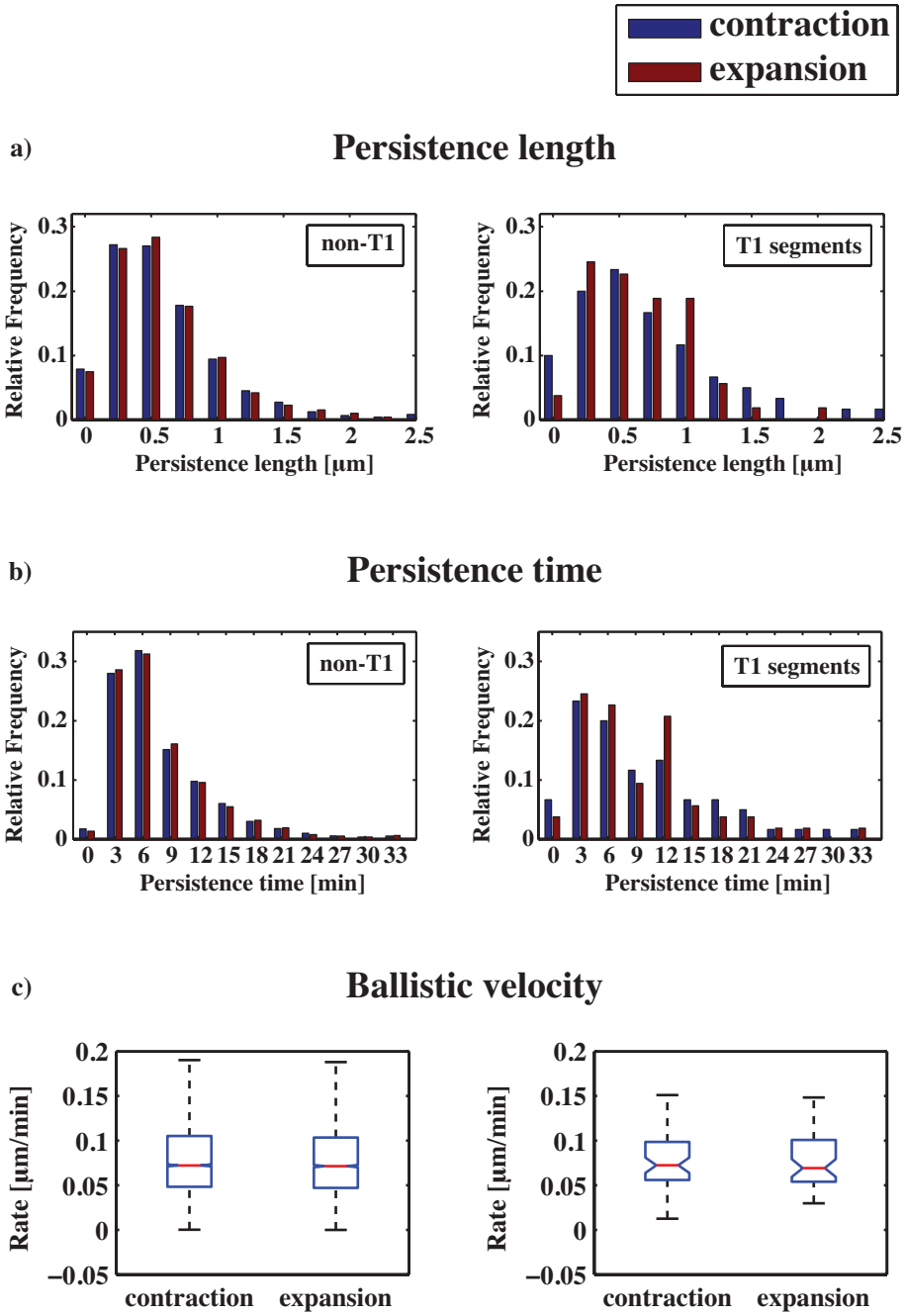

Figure 5.7: Persistence lengths, time, and ballistic velocity

a) Histograms for the persistence length of non-T1 (left) and T1 segments (right). Contracting (blue) and expanding (red) segments are shown separately. The p-values for a Kolmogorov-Smirnov test comparing the distributions are: contracting non-T1 vs expanding non-T1 $p = 0.5576$ (ns), contracting T1 vs expanding T1 $p = 0.7276$ (ns), all non-T1 vs all T1 $p = 0.5294$ (ns). **b)** Histograms for the persistence time of non-T1 and T1 segments. The Kolmogorov-Smirnov test is not valid for discrete distributions. **c)** Boxplots for the ballistic velocity (persistence length / persistence time) for non-T1 and T1 segments. The The p-values for a Kolmogorov-Smirnov test comparing the distributions are: contracting non-T1 vs expanding non-T1 $p = 0.1613$ (ns), contracting T1 vs expanding T1 $p = 0.9594$ (ns), all non-T1 vs all T1 $p = 0.3243$ (ns). The filter setting is 20. $N = 11377$ non-T1 segments and 114 T1 segments from 4 nota.

5.5 Discussion

The aim of this chapter was to investigate the hypothesis that the contraction and expansion events giving rise to neighbour exchange result from the ubiquitous stochastic fluctuations of junctions in the tissue. Interestingly, T1 events do not appear to have a well-defined time and length scale, which motivated carrying out the analysis and statistical tests for a wide range of filter settings. For every level of filtering, the statistical tests showed no difference between junction fluctuations and neighbour exchange. This supports viewing neighbour exchange events as an epiphenomenon of the stochastic fluctuations present in the tissue, rather than as directed singular processes.

We also found that neighbour exchange events are symmetric with respect to the rate of contraction and expansion, going into and coming out of a four-way vertex configuration. Interestingly, the rate of contraction is very similar to what has been reported for junction remodelling during germ-band elongation [57].

Two observations that will inform how we model junction dynamics later, are (i) that the distribution of persistence lengths skew left relative to the expectation for a simple random walk process, and (ii) that the mean square displacement curve shows subdiffusive behaviour. This suggests that junction fluctuations could be consistent with a constrained random walk and that will be our starting point for the modelling in Chapter 7.

However, we first establish the phenomenology of tissue ordering. Specifically, in the next chapter, we will consider different measures of order and quantify the time course of the ordering process.

Chapter 6

Ordering over the course of pupal development

The aim of this thesis is to understand how order emerges in the *Drosophila* notum and how neighbour exchange events contribute to that process. In this section I address the premise of this research question, namely that tissue packing does in fact become more regular over the course of pupal development and that this process is associated with neighbour exchange events. I quantify order in the tissue at different points in development and track a time course of the ordering process.

There are different measures of the degree of order in a tissue. From time-lapse imaging of the notum, we visually perceive an increase in the regularity of the cell array. In general, finding an objective proxy for our perception of spatial order, is non-trivial [98]. Here I will focus on the distribution of polygons and junction lengths. In the absence of cell division and cell extrusion, changes in polygon number are caused solely by neighbour exchange events. By contrast, ordering in terms of junction lengths is driven by tension in the system and does not rely on neighbour exhange. Hence, these two measures of order are complementary and are directly related to experimentally measurable quantities: neighbour exchange frequency and junction tension.

In the previous sections we studied junction dynamics in the absence of pertubing cellular events, such as division and extrusion, using time-lapse imaging at 12h AP. Around 13.5h AP there is an onset of cell division, with every cell in this part of the notum[1] dividing once. In addition, a small proportion of cells ($0.5 \pm 0.3\%$) delaminate from the tissue through a stochastic process of live cell

[1]The scutum, mesonotum

extrusion. [89]. This period of pupal development lasts until around 20h AP, after which the tissue resumes the process of refinement. Therefore, to track the ordering process over several hours, we image the notum post division.

6.1 Tissue order increases over the course of development

The distribution of polygons is an important measure of order in the tissue. Without cell division or cell extrusion, the only way a cell can change its number of edges is by going through a neighbour exchange event. Figure 6.1 shows histograms for the polygons at different developmental time points. The proportion of hexagons in the tissue increases over time and the standard deviation of the distribution decreases. In particular, there is a reduction in the number of cells with 4 or 8 edges. Hence cells in the tissue become more hexagonal over the course of development. The figure also shows histograms for the junction lengths. The first thing to notice is that post division, cells are smaller and junction lengths are shorter. I therefore use the coefficient of variation (std/mean) to compare the distributions. The coefficient of variation decreases over time, corresponding to junction lengths becoming more even in the tissue.

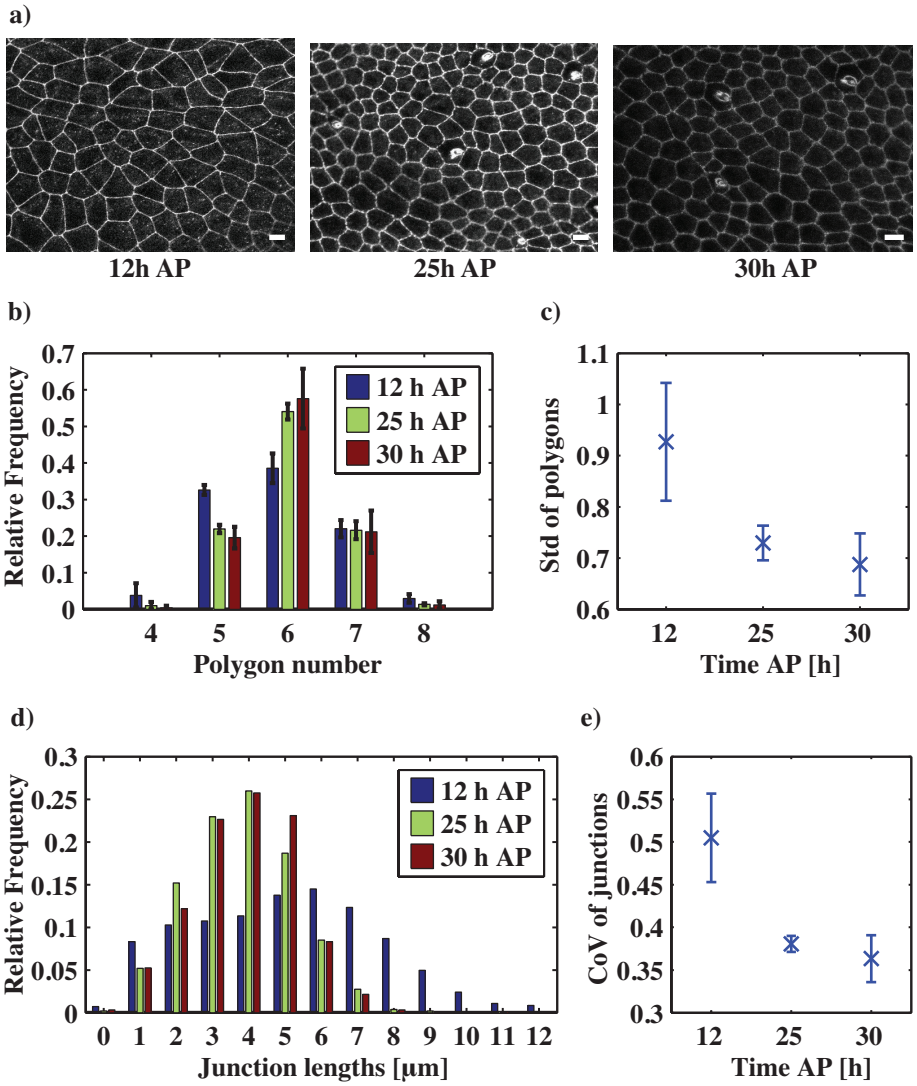

Figure 6.1: Ordering over the course of pupal development

a) Fluorescent images of *Drosophila* tissue at different developmental time points. The bright spots in the images at 25 h AP and 30 h AP, are microchaete bristle cells. Scale bar = 5 µm. **b)** Histogram of the polygon distribution at different developmental time points. $N = 236$ cells from 4 nota (12.5 h), 296 cells from 3 nota (25 h), 250 cells from 3 nota (30 h). Errorbars indicate the variation between nota, i.e. the standard deviation of the standard deviations for different nota. **c)** Standard deviation for the polygon distributions shown in b). Errorbars indicate the standard deviation between nota. The p-values for an F-test comparing the variances are: 12 h v 25 h $p < 0.0001$ (*), 12 h v 30 h $p < 0.0001$ (*), 25 h v 30 h $p = 0.3346$ (ns). **d)** Histogram of the junction length distribution at different developmental time points. $N = 828$ junctions from 4 nota (12.5 h), 1059 junctions from 3 nota (25 h), 936 junctions from 3 nota (30 h) **e)** Coeffcients of variation ($\sigma / \langle l \rangle$) for the junction length distributions shown in d). Errorbars indicate the standard deviation between nota. The p-values for an F-test comparing the variances are: 12 h v 25 h $p < 0.0001$ (*), 12 h v 30 h $p < 0.0001$ (*), 25 h v 30 h $p = 0.2624$ (ns). Bristle cells and cells adjacent to bristle cells have been excluded from the analysis.

6.2 Steady increase in order over several hours is driven entirely by neighbour exchange

The results in Figure 6.1 show that, both in terms of polygon distribution and junction lengths, tissue packing in the notum becomes more regular over developmental time. To investigate the time course of the ordering process, we follow the tissue over a period of several hours. Since, the onset of cell division around 13.5 h AP disrupts the ordering of the tissue, we study how packing proceeds post division. We imaged the nota from 20 h AP, at 10 min intervals. The tissue is stable in the sense that we do not observe cell division, delamination or apoptosis events. However, during this window of pupal development, a pattern of microchaete bristle cells emerges on the notum [50]. Bristle cells are external mechanosensory organs and are part of the *Drosophila* peripheral nervous system [99]. From around 25 h AP, the michochaetes grow in apical area and number of edges, triggering a slew of neighbour exchange events that perturb the surrounding tissue. As microchaetes grow, adjacent cells go through neighbour exchange to accomodate the increase in apical area and this, in turn, affects the neighbours of those cells.

Figure 6.2 shows the apical area and polygon number of michochaetes relative to other cells for a single notum. The time point at which microchaete bristle cells deviate by more than one standard deviation from non-bristle cells is marked, as is the time point at which the growth phase ends and the area and polygon number stabilizes.

During the growth phase, microchaetes perturb the surrounding tissue and disrupts polygon ordering. Even though development of the microchaete bristle pattern is an interesting problem (see [50, 100]), our focus here is the ordering process that happens in the absence of this pertubation. For this reason, bristle cells and cells adjacent to bristle cells are excluded from the analysis.

As shown in Figure 6.3, we observe a steady increase in order between 22h and 34h. The proportion of hexagons increases and the standard deviation of polygon type decreases, moving the system towards hexagonal packing. Interestingly, this increase in tissue order is driven entirely by neighbour exchange events.

The other measure of order we are using is the variance of junction lengths. Figure 6.4 shows that the coefficient of variation (std/mean) for junction lengths decreases steadily over time, leading to a more regular tissue architecture. The figure also shows the average coefficient of variation for junctions within individual cells and this follows a similar trajectory. Hence, both across the tissue and within cells, junction lengths even out over time. Unlike for polygon distributions, this ordering process is not necessarily driven by neighbour exchange, as networks under tension generally exhibit this type of behaviour.

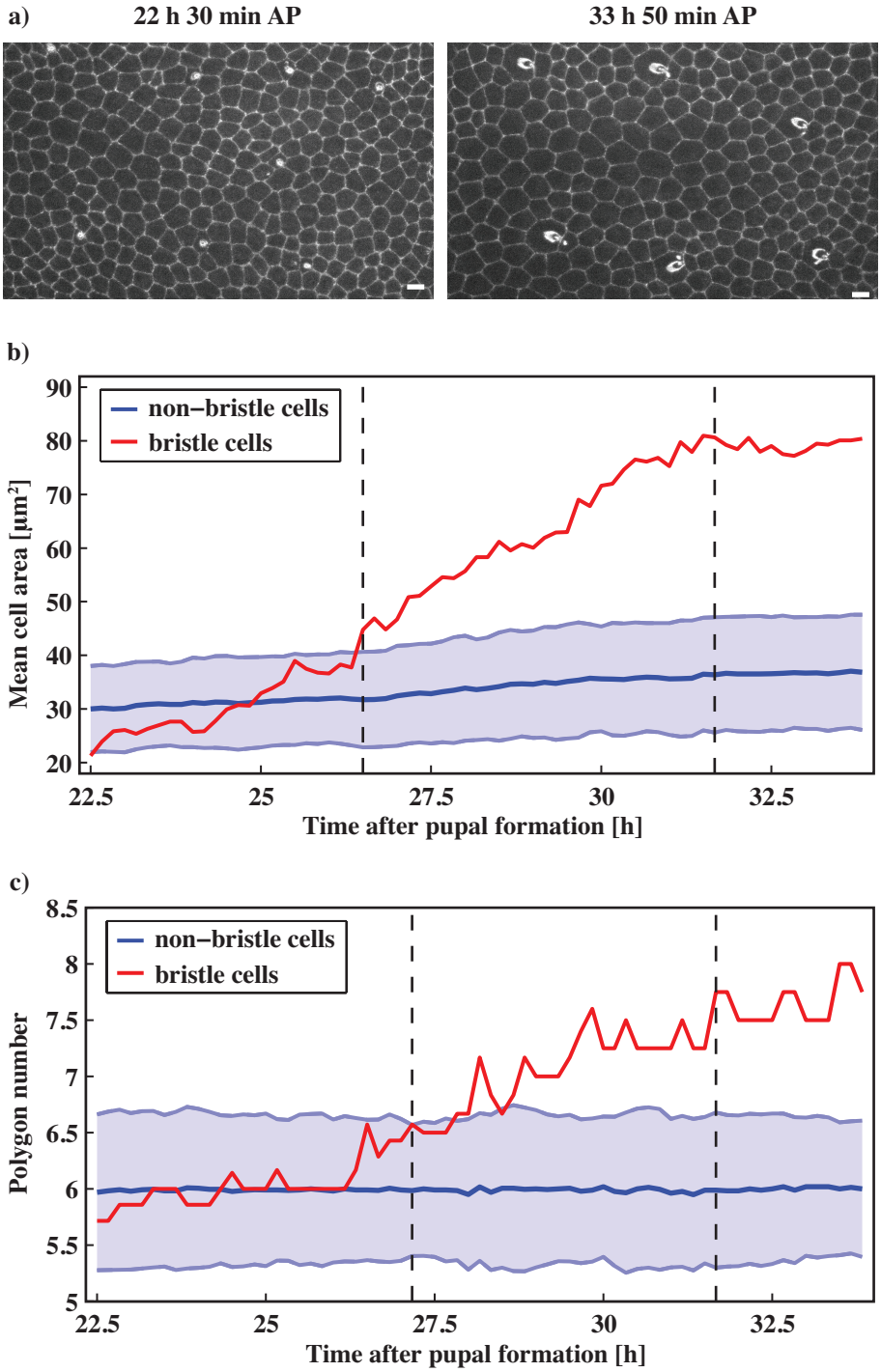

Figure 6.2: Disruptive effect of bristle cells

a) Tissue at different developmental time points. (left) 22 h 30 min AP and (right) 33 h 50 min AP. Scale bar = 10 µm. **b)** Mean cell area for bristle cells (red, $N = 8$) and non-bristle cells (blue, $N = 312$). The errorbars are the standard deviation for the cell areas of non-bristle cells. The dashed line at $t = 26.5$ h indicates where the mean cell area of bristle cells falls outside one σ of that of non-bristle cells. **c)** Mean polygon number for bristle cells (red, $N = 8$) and non-bristle cells (blue, $N = 312$). The errorbars are the standard deviation for the polygon distribution of non-bristle cells. The dashed line at $t = 27$ h 10 min indicates where the mean polygon number of bristle cells falls outside one σ of that of non-bristle cells. For b) and c), the dashed line at $t = 31$ h 40 min is placed by eye where the mean cell area and polygon number of the bristle cells appear to stabilize. Cells adjacent to a bristle cell are excluded from the analysis. Not all cells persist for the duration of the movie due to translation of the tissue relative to the microscope.

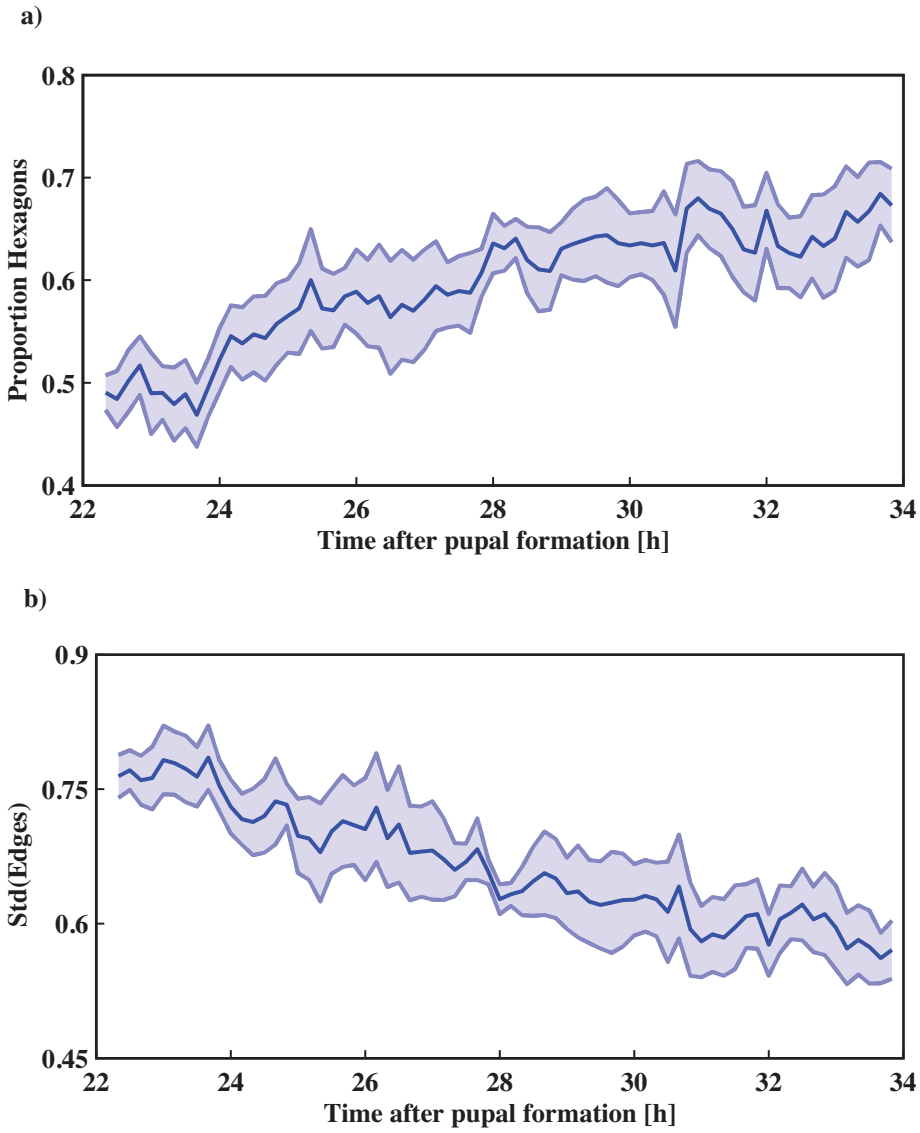

Figure 6.3: Ordering of polygons

a) Proportion of hexagonal cells in the tissue, tracked over a period of 12 hours. The figure shows the mean for 5 nota, with a combined 395 cells. The errorbars are the standard deviation on the mean. Bristle cells and cells adjacent to bristle cells are excluded from the analysis. **b)** Standard deviation for the polygon distribution of cells in the tissue, tracked over a period of 12 hours. The figure shows the mean for 5 nota, with a combined 395 cells. The errorbars show the variation between nota, i.e. they are the standard deviation on the mean for the standard deviation of the polygon distribution for the 5 nota. Bristle cells and cells adjacent to bristle cells are excluded from the analysis.

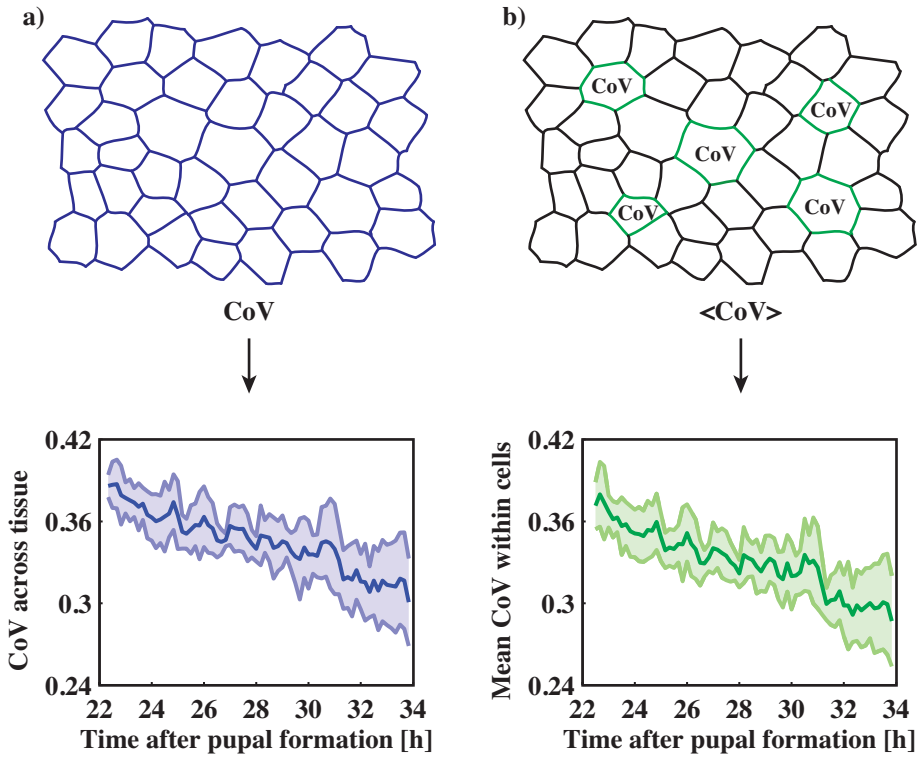

Figure 6.4: Ordering of junction variation, global and local

a) Schematic and plot for the coefficient of variation ($\sigma/\langle l \rangle$) for junction lengths in the tissue, tracked over a period of 12 hours. The figure shows the mean and standard deviation for 5 nota, it includes data from a total of 2427 junctions. **b)** Schematic and plot for the mean coefficient of variation ($\sigma/\langle l \rangle$) within cells, tracked over a period of 12 hours. For each cell, the CoV is calculated for junctions in that cell and the average is taken over all cells in the tissue. For the figure, the mean CoV has been calculated for 5 nota separately and the mean and standard deviation of these are taken. The figure includes data from a total of 395 cells. Not all junctions or cells persist for the duration of the movie. Bristle cells and cells adjacent to bristle cells are excluded from the analysis.

6.3 Discussion

The results in this section show that the notum orders over the course of pupal development. The proportion of hexagonal cells in the tissue increases and the variance in polygon type and junction length decreases, leading to a more regular tissue packing.

Tracking a time course for the ordering process, over a period of 12 hours post division, shows a steady increase in order driven entirely by neighbour exchange events. The proportion of hexagons increases and the standard deviation of polygon type decreases, moving the system towards hexagonal packing.

I also calculated the coefficient of variation for junction lengths over time. The variation in the length of junctions across the tissue and within cells are very similar and both show a clear decrease over the course of development. Interestingly, microchaete bristle cell growth appears to disrupt ordering in terms of polygons but not junction lengths (the disruption was visible in the graphs for individual nota, but averages out when data from several nota are combined). This could be related to Lewis Law, which dates back to the 1920's and states that apical cell areas increase linearly with the number of edges [101, 102]. As described in [Curran 2015], this relation holds almost perfectly for cells in the *Drosophila* notum, with the exception of microchaete bristle cells late in development. When microchates grow it disrupts the cell area and polygon ordering in the surrounding tissue. But, by Lewis Law, larger/smaller cells have more/fewer junctions and, as such, junction lengths do not depend on cell size and are therefore unaffected by the pertubation.

Taken together with the previous section, which showed that neighbour exchange events are stochastic, the results give rise to the question of how stochastic events can drive ordering. To answer this, we first investigate the source of stochasticity in the tissue and this will be the focus of the next section.

Chapter 7

The role of myosin in regulating junction fluctuations

Before attempting to answer how junction length fluctuations contribute to tissue ordering, we consider how such fluctuations arise within the tissue. In particular, we want to identify the underlying source of stochasticity in the tissue.

On a molecular level, junction tension is generated by the contractile action of actomyosin. Linking of the actomyosin cytoskeleton to adherens junctions converts the force generated, by the movement of Myosin II molecular motor proteins along actin filaments, into junction tension. The localisation of Myosin II changes over the course of pupal development. Around 12h AP, Myosin II is observed both at junctions and in a medial pool. As the tissue matures, Myosin II increases at junctions - forming dense cables - and is lost from the medial pool. This relocalisation of Myosin II correlates with an increase in line tension, as described in [Curran 2015]. In germ-band elongation, Myosin II is specifically enriched at shrinking junction oriented along the D-V axis and this polarized distribution has been shown to be necessary for successful elongation of the tissue [53]. Hence, Myosin II is a prime candidate for how stochastic junction fluctuations originate and are regulated within the tissue.

In this section, we describe the properties and dynamics of junctional Myosin II in the *Drosophila* notum. In particular, we identify similarities and differences with GBE to understand the components of stereotyped junction remodelling. Using a combination of experiment and modelling, we investigate how Myosin II contributes to stochasticity and what role it has in regulating junction dynamics.

7.1 There is no polarization of junctional Myosin II within the tissue

One aim of this section is to determine if there are any biases in how Myosin II is localised within the tissue. To this end, we use single time-point images at 12h AP to study the static distribution of Myosin II and Bazooka. The results are shown in Figure 7.1.

For Bazooka, the measured intensity is uncorrelated with junction length, whereas there is a slight negative correlation for Myosin II. Hence, relative to length, Myosin II intensity is higher for shorter junctions - the intensity per pixel[1] for a 2 μm junction is approximately 15% higher than for a 10 μm junction. There is no significant correlation between the intensity of Myosin II and Bazooka on individual junctions.

As is evident from the fluorescent images in Figure 3.5, Myosin II intensity varies more across the tissue than Bazooka. The figure shows the distribution of Myosin II and Bazooka for junctions in the tissue - the standard deviations are 0.11 and 0.077, respectively, demonstrating that Myosin II is more spatially heterogeneous. The most important result for the localization of Myosin II is that the intensity is uncorrelated with junction orientation, demonstrating that there is no polarization of Myosin II within the tissue. This is in contrast with GBE, where Myosin II is enriched in shrinking junctions oriented along the D-V axis.

[1] Normalizing by the number of pixels gives the same results as normalizing by junction length, but is more accurate.

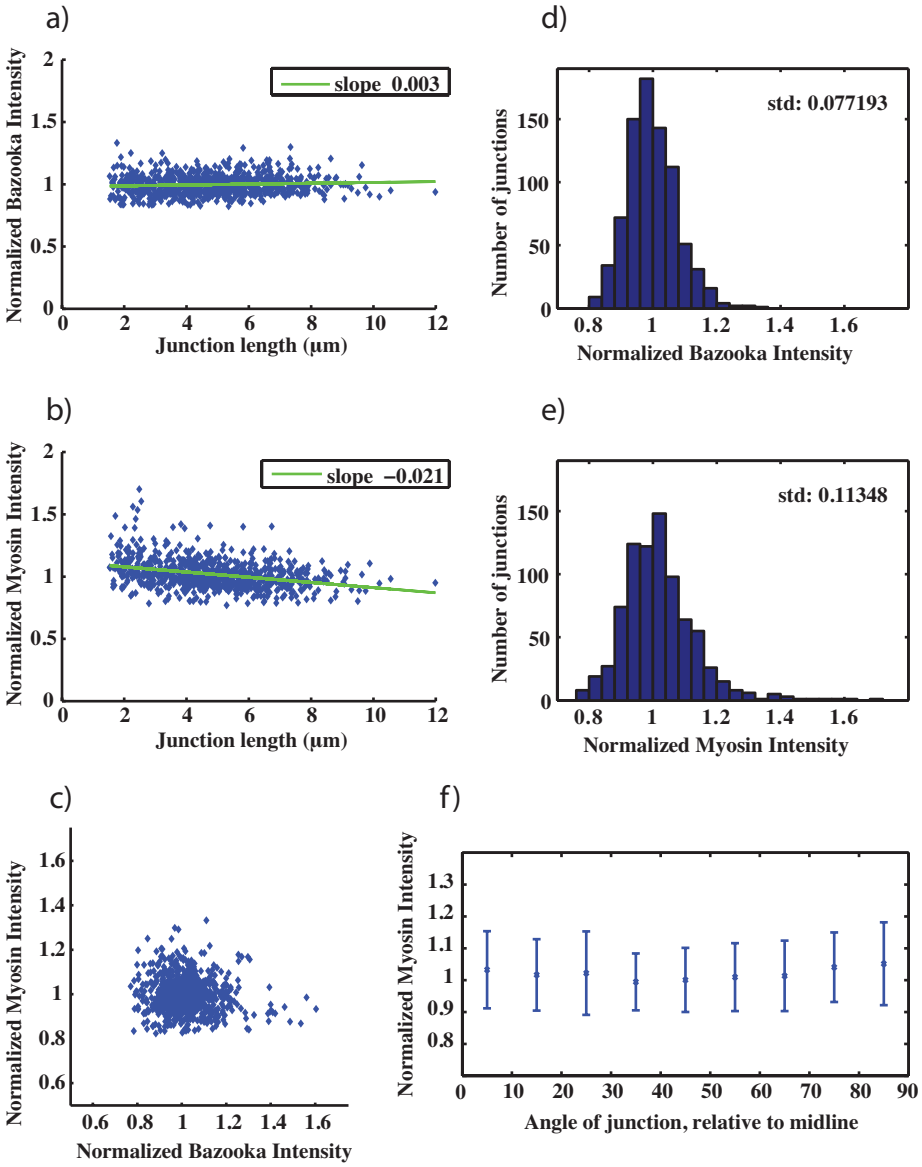

Figure 7.1: Properties of Myosin and Bazooka in the tissue

a) Normalized (average intensity per pixel) Bazooka intensity plotted against junction length. Each data point corresponds to one junction. **b)** Normalized Myosin intensity plotted against junction length. **c)** Normalized Myosin intensity vs normalized Bazooka intensity. The Pearson correlation coefficient is -0.097, indicating that there is no significant relation between the quantities. **d)** Distribution of the normalized Bazooka intensity of junctions, standard deviation $= 0.077$. **e)** Distribution of the normalized Myosin intensity of junctions, standard deviation $= 0.11$. **f)** Normalized Myosin intensity versus the angle of the corresponding junction. The angle is measured relative to the midline so junctions parallel with the midline have angle $= 0$. Each of the figures contain data from three movies, in total 809 junctions. In each case only the first time frame of the movie is used.

7.2 Myosin II on individual junctions fluctuates over time

The spatial heterogeneity of Myosin II in the tissue and the negative correlation with junction length, suggests that Myosin II could be involved in regulating junction dynamics. Combining the analysis of fluorescence intensity, described in the Methods chapter, with the tracking of junctions over time, allows us to compare the temporal behaviour of Myosin II with changes in junction length.

Figure 7.2 shows time traces for the intensity of Myosin II and Bazooka, along with junction length. Imaging was done at 5s and 30s intervals (on separate occasions), to both get a high temporal resolution and follow the dynamics on longer time scales. The examples shown are representative. Two things are worth noting. Firstly, Myosin II intensity varies significantly over time, whereas Bazooka intensity remains relatively stable. The spatial uniformity and temporal invariance of Bazooka, indicates that it is a suitable control in this system. Secondly, it appears that Myosin II and junction length are anti-correlated and this is corroborated by visual inspection of time traces for other junctions in the tissue. To make this observation more rigourous, we turn to correlation analysis.

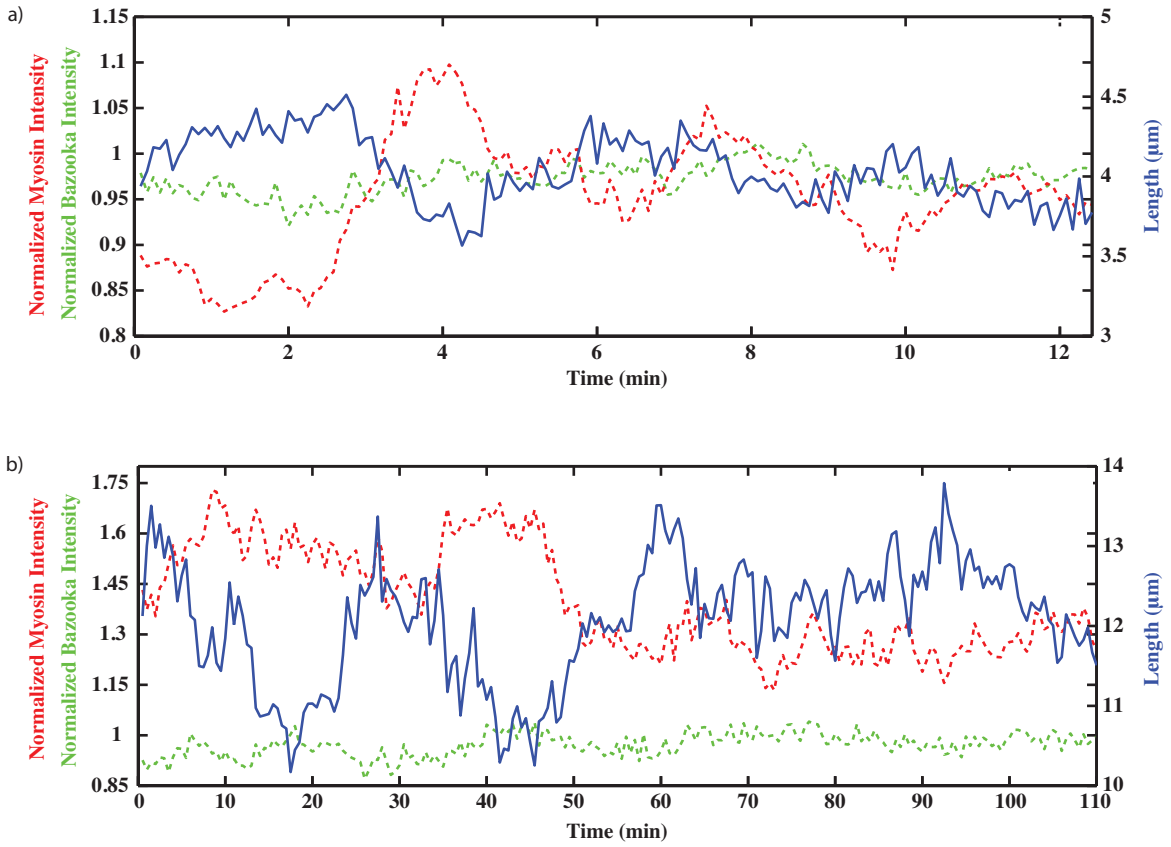

Figure 7.2: Time traces for junction length and Bazooka and Myosin intensities.

Time traces for junction length and Bazooka and Myosin intensities for individual junctions. **a)** Junction with ID 26 in the 5s SqhAx3-BazmCh 301014 movie. **b)** Junction with ID 109 in the 30s SqhAx3-BazmCh 060813 movie. The examples are representative of the dynamics observed for junctions in the tissue

7.3 The autocorrelation for Myosin II fluorescence intensity decays exponentially

The correlation function (unbiased) of two time series x_n and y_n of length N is given by

$$R_{xy}(m) = \frac{1}{N-|m|} \sum_{n=0}^{N-m-1} x_{n+m} y_n \tag{7.1}$$

Here m is the number of lags. The autocorrelation is commonly normalized by dividing by the variance σ^2, resulting in a value of $R_{xy} = 1$ at $m = 0$. Similarly, the crosscorrelation is normalized by the product of the standard deviation of each of the two processes $\sigma_x \sigma_y$. I calculate the mean of the correlation function for all junctions in the tissue as this captures the essential features of the process while reducing the effect of spurious correlations in the time series. The correlation function for each junction is normalized before the population mean is taken.

$$R_{xy}(m) = \frac{1}{J} \sum_{j=1}^{J} \frac{1}{\sigma_x^j \sigma_y^j (N-|m|)} \sum_{n=0}^{N-m-1} x_{n+m}^j y_n^j \tag{7.2}$$

Figure 7.3 shows the mean autocorrelation for Myosin II intensity calculated from 269 junctions in a tissue imaged at 30s intervals. The decay of the autocorrelation function is in good agreement with an exponential function of the form $\exp -t/\tau$ and this is consistent with the expectation for an Ornstein-Uhlenbeck process. The turnover time for the process is $\tau = 3.48 \pm 0.093$ min, which is similar to the value of 108 ± 66 s reported in [103] for dorsal closure in the *Drosophila* embryo.

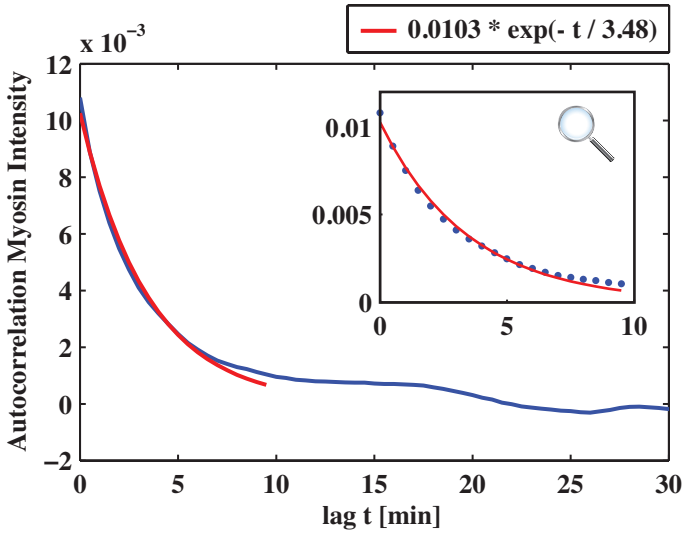

Figure 7.3: Myosin autocorrelation

(blue) The unnormalized autocorrelation for Myo-II intensity ($N = 269$ junctions, 1 notum). **(red)** The best fit for an exponential of the form $y = a * \exp(-t/\tau)$. The coefficients are: $a = 0.0103 \pm 0.00017$, $\tau = -3.48 \pm 0.093$ min. The standard deviation on the turnover time is calculated from the variance-covariance matrix for the fitted coefficients. **(inset)** A zoom of the first 10 min figure, showing the experimental data points.

7.4 Changes in Myosin II precede changes in junction length

To study the interaction between Myosin II and junction fluctuations, I calculate the crosscorrelation. Figure 7.4 shows the crosscorrelation function for both Myosin II and Bazooka intensity against junction length. The correlation function for Bazooka is symmetric with a negative correlation at lag 0. This is what you would see if the total Bazooka on a junction were conserved - as a junction contracts/expands the number of Bazooka molecules stays the same and therefore the concentration increases/decreases. Note that if junction length changes happened purely by vertices sliding, we would expect that the Bazooka concentration would remain constant and the crosscorrelation function would be flat. Combined with Figure 7.1 a), the result shows that Bazooka intensity is independent of junction length, but when the junction length fluctuates the Bazooka intensity transiently goes above or below its steady state level. Unlike Bazooka, the crosscorrelation function for Myosin II is distinctly asymmetric with a minimum at a lagtime of -35 s (7 frames), demonstrating that changes

in Myosin II intensity preceede changes in junction length. This result is highly non-trivial and suggests a causative role for Myosin in regulating junction length.

I first did this analysis using time-lapse imaging taken at 30 s intervals and observed a minimum at a negative lag of 1 frame, which motivated collecting data at a higher temporal resolution to be able to determine the position of the minimum more accurately.

Interestingly, the timescale for the interaction between junction length and Myosin II is in agreement with what has been reported in germband elongation. Collinet et al. [104] studied cell intercalation focusing on the extension of new junctions following neighbour exchange. They report that the crosscorrelation for the extension rate and the rate of change of junctional Myosin II intensity has a minimum at -40 s, with changes in junction length lagging[2].

[2]In Collinet et al. [104], the crosscorrelation function is given in Figure 4 (j), but they do not report the position of the minimum. This was instead found by taking a measurement from the figure.

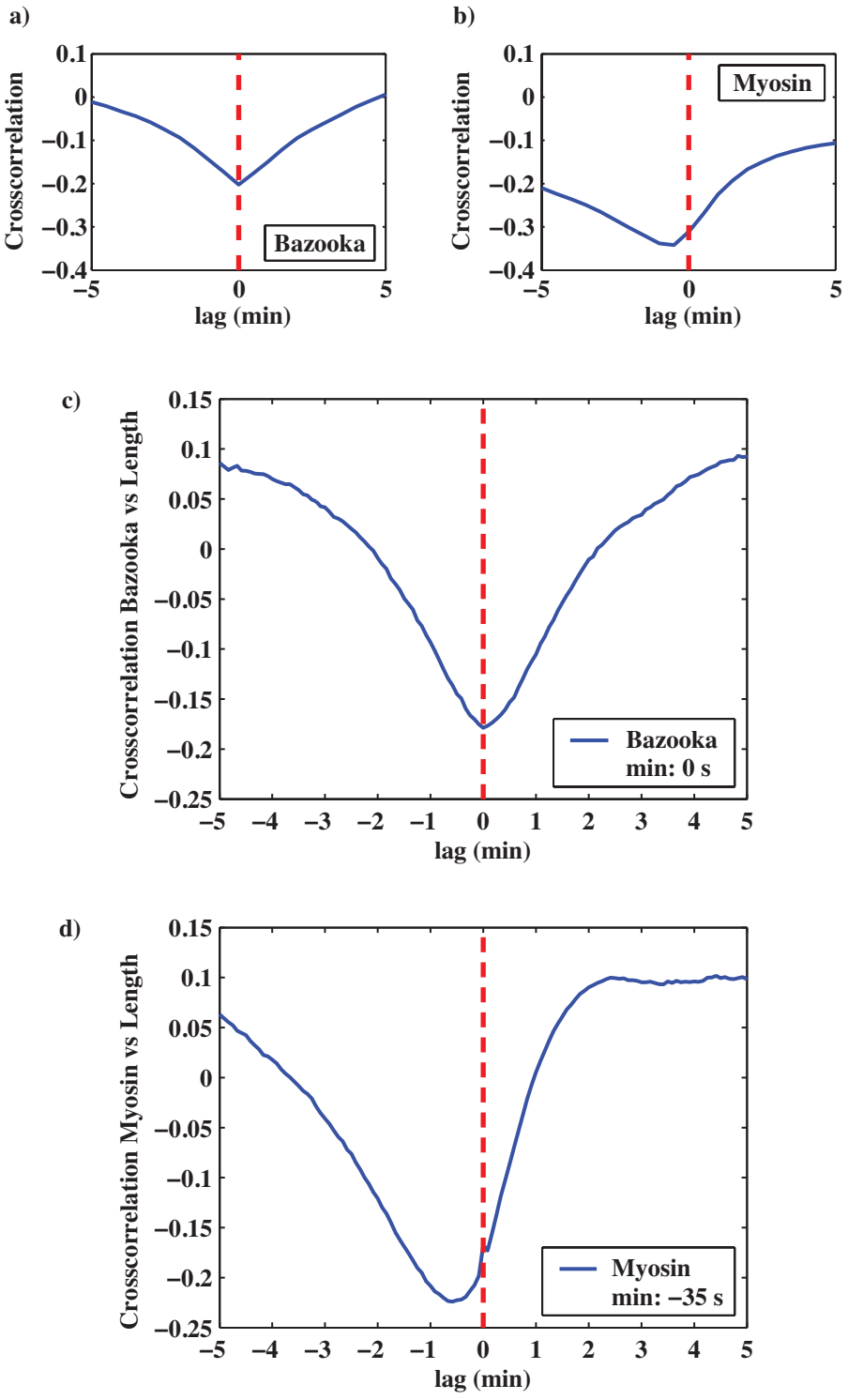

Figure 7.4: Crosscorrelation functions for Myosin II and Bazooka intensity against junction length

a) Mean crosscorrelation for Bazooka intensity and junction length ($N = 269$, 1 notum) for a notum imaged at 30 s intervals. The minimum for the crosscorrelation function occurs at $lag = 0$. **b)** Mean crosscorrelation for Myosin intensity and junction length, same notum as in a). The minimum for the crosscorrelation function occurs at $lag = -1$, corresponding to 30 s. **c)** Mean crosscorrelation for Bazooka intensity and junction length ($N = 747$, 3 nota) for nota imaged at 5 s intervals. The minimum for the crosscorrelation function occurs at $lag = 0$. **d)** Mean crosscorrelation for Myosin intensity and junction length, same nota as in c). The minimum for the crosscorrelation function occurs at $lag = -7$, corresponding to 35 s.

7.5 Stochastic Model of Junction Fluctuations Driven by Turnover of Myosin

To understand the role of Myosin II in regulating junction fluctuations, particularly the causality suggested by the crosscorrelation function in Figure 7.4, we turn to modelling. Our starting point is a recently published model for oscillatory behaviour in an elastic contractile material with a turnover of force-producing molecules [103]. In the paper, the model is applied to describe cellular oscillations in the *Drosophila* embryo during dorsal closure. During dorsal closure, the lateral epidermal sheets are pulled together, fusing along the midline, to close the hole in the dorsal epithelium left by germ band retraction [105]. It is the last major morphogenetic event before the window of pupal development that we are imaging. At 12 h AP, cells in the midline region have an anisotropic geometry and are under compression, but as the tissue matures - through a process of neighbour exchange and delamination - cells become isotropic and the midline becomes indistinguishable from the rest of the tissue [89].

The model, developed by Dierkes et al., consists of a set of coupled differential equations describing the dynamics of myosin concentration c (Eq. 7.3) and junction length l (Eq. 7.4).

$$\frac{dc}{dt} = -\frac{1}{\tau}(c - c_0) - \frac{c}{l}\frac{dl}{dt} \tag{7.3}$$

$$\mu\frac{dl}{dt} = T_e - T(c) - K(l) \tag{7.4}$$

$$T_e = T(c_0) + K(l_0) \tag{7.5}$$

$$T(c) = T(c_0) + t_1(c - c_0) \tag{7.6}$$

$$K(l) = K(l_0) + k_1(l - l_0) + k_3(l - l_0)^3 \quad \Rightarrow \tag{7.7}$$

$$\mu\frac{dl}{dt} = -t_1(c - c_0) - k_1(l - l_0) - k_3(l - l_0)^3 \tag{7.8}$$

Here, c_0 is the equilibrium concentration of myosin and l_0 is the equilibrium length. The first term in equation 7.3 comes from turnover of myosin with binding and unbinding rates $k_{on} = c_0/\tau$ and $k_{off} = c/\tau$, respectively. The second term is related to matter conservation and ensures that, in the absence of turnover,

cl is constant. Hence, changes in length affect the concentration, but not the total amount, of myosin on a junction.[3] Note that the third order term does not significantly affect the dynamics, but has been included here to maintain agreement with the model of Dierkes et al.

Within the model, a junction consists of a spring and dashpot in parallel with a contractile unit. The spring element has an elastic restoring force $K(l)$, the tension generated by the contractile unit is given by $T(c)$ and depends on the concentration of myosin, and the damping coefficient μ adds viscous dissipation to the system. In addition, there is an external tension T_e from neighbouring junctions. Since the whole network is under tension, T_e opposes contraction of the junction. In the paper, Dierkes et al. assume that the system is at steady state with the external and internal tension terms balancing. The terms $T(c)$ and $K(l)$ can then be expanded around the steady state, to give equation 7.8. As described in the paper, the system exhibits three types of behaviour, depending on the combination of parameters.

- Stability. After the transient has decayed, both c and l are constant and equal their equilibrium values c_0 and l_0.
- Oscillations. The system undergoes a Hopf bifurcation at $(t_1 c_0)/(k_1 l_0) = 1 + \mu/(k_1 \tau)$. The resulting limit cycle is stable with sustained oscillations around the equilibrium values c_0 and l_0.
- Collapse. A further increase of tension in the system causes the system to collapse to $l = 0$.

For our purposes, we are interested in the behaviour of the system in the presence of stochasticity and I therefore modify the model in Dierkes et al. to study this. It is known that binding and unbinding of myosin is a stochastic process [106, 107]. Although, we do see some evidence of binding cooperativity in how the variance of myosin intensity scales with the mean intensity on individual junctions (data not shown), for now we ignore mechanical coupling

[3] A quick calculation shows how this term keeps cl constant. $\frac{dc}{dt} = -\frac{c}{l}\frac{dl}{dt} \Leftrightarrow \frac{1}{c}\frac{dc}{dt} = -\frac{1}{l}\frac{dl}{dt}$ Use integration by parts. $1 + \int \frac{1}{c} dt = -1 - \int \frac{1}{l} dt \Leftrightarrow ln(c) + ln(l) = -2 \Leftrightarrow ln(cl) = -2$. Hence cl is constant.

between myosin molecules and introduce stochasticity in myosin turnover via an uncorrelated white noise term $\xi(t)$.

$$\langle \xi(t) \rangle = 0 \tag{7.9}$$

$$\langle \xi(t)\xi(t') \rangle = \delta(t - t') \tag{7.10}$$

First, we rewrite equations 7.3 and 7.8 in terms of the nondimensional variables for myosin concentration (x), length (y), and time (z). The white noise term has a prefactor $1/\sqrt{z}$ to make the equations invariant to changes in the size of the time step δz in the simulations.

$$x \equiv \frac{c}{c_0} \quad , \quad y = \frac{l}{l_0} \quad , \quad z \equiv \frac{t}{\mu} k_1 \tag{7.11}$$

$$\frac{k_1 c_0}{\mu}\frac{dx}{dz} = -\frac{c_0}{\tau}(x-1) - \frac{k_1 c_0}{\mu}\frac{x}{y}\frac{dy}{dz} + \frac{1}{\sqrt{z}}\xi(z) \quad \Leftrightarrow \tag{7.12}$$

$$\frac{dx}{dz} = -\frac{\mu}{k_1 \tau}(x-1) - \frac{x}{y}\frac{dy}{dz} + \frac{1}{\sqrt{z}}\xi(z) \tag{7.13}$$

$$k_1 l_0 \frac{dy}{dz} = -t_1 c_0 (x-1) - k_1 l_0 (y-1) - k_3 l_0^3 (y-1)^3 \tag{7.14}$$

$$\frac{dy}{dz} = -\frac{t_1 c_0}{l_0 k_1}(x-1) - (y-1) - \frac{k_3 l_0^2}{k_1}(y-1)^3 \tag{7.15}$$

The nondimensional parameters are given in 7.16, leaving us with the nondimensional equations governing the dynamics of the system 7.17.

$$\alpha \equiv \frac{\mu}{k_1 \tau} \quad , \quad \beta \equiv \frac{t_1 c_0}{l_0 k_1} \quad , \quad \gamma \equiv \frac{k_3 l_0^2}{k_1} \tag{7.16}$$

$$\begin{aligned} \frac{dx}{dz} &= -\alpha(x-1) - \frac{x}{y}\frac{dy}{dz} + \frac{1}{\sqrt{z}}\xi(z) \\ \frac{dy}{dz} &= -\beta(x-1) - (y-1) - \gamma(y-1)^3 \end{aligned} \tag{7.17}$$

To study the behaviour of the system, I use a discrete-time numerical simulation. The uncorrelated white noise is a random variable sampled from a uniform distribution in the interval $[-0.5, 0.5]$ scaled by the noise strength ξ. There are two things to note about the system. Firstly, changing the noise strength does not affect the parameter space of the model. However, noise blurs the border between adjacent basins of attraction, occasionally leading to collapse in regions of parameter space that are otherwise stable. Secondly, the parameter space does in general depend on the initial conditions. The initial conditions determine which basin of attraction the system starts in and therefore which solution it converges towards. Here, we assume the system is at steady state and therefore focus on fluctuations around equilibrium. Varying the initial conditions around the equilibrum values c_0 and l_0 does not change the behaviour of the system (data not shown).

Figure 7.5 shows simulated time traces for the fluctuations of myosin and junction length. The simulations are carried out using the nondimensional parameters and time. Fortuitously, the time is nondimensionalised in such a way that we only require the value of τ to translate it into experimental time.

$$z = \frac{t}{\mu}k_1 \quad \wedge \quad \alpha = \frac{\mu}{k_1\tau} \quad \Rightarrow \tag{7.18}$$

$$t = z\alpha\tau \tag{7.19}$$

This allows us to present the time traces and crosscorrelation function in units of minutes using $\tau = 3.48$ min from the autocorrelation in Figure 7.3. The standard deviation of the myosin time series depends on the noise strength and, for $\xi = 0.3$, is similar to the average experimental value. Our model does not include the fluctuations in junction length arising from mechanical coupling to other junctions and taking these into account would increase junction length variation. From the simulated time traces we can calculate the mean crosscorrelation in the same way as in Figure 7.4. Interestingly, this gives the same asymmetry as observed for the experimental data, with changes in myosin leading changes in junction length, at least for the set of parameters chosen here.

Several factors combine to cause the experimental crosscorrelation to be weaker

than in the model. The experimental data is for the fluorescence intensity of myosin rather than the actual concentration and the relation between those two quantities may be nonlinear. Measurement errors from segmentation and the finite resolution of the microscope would also weaken the correlation.

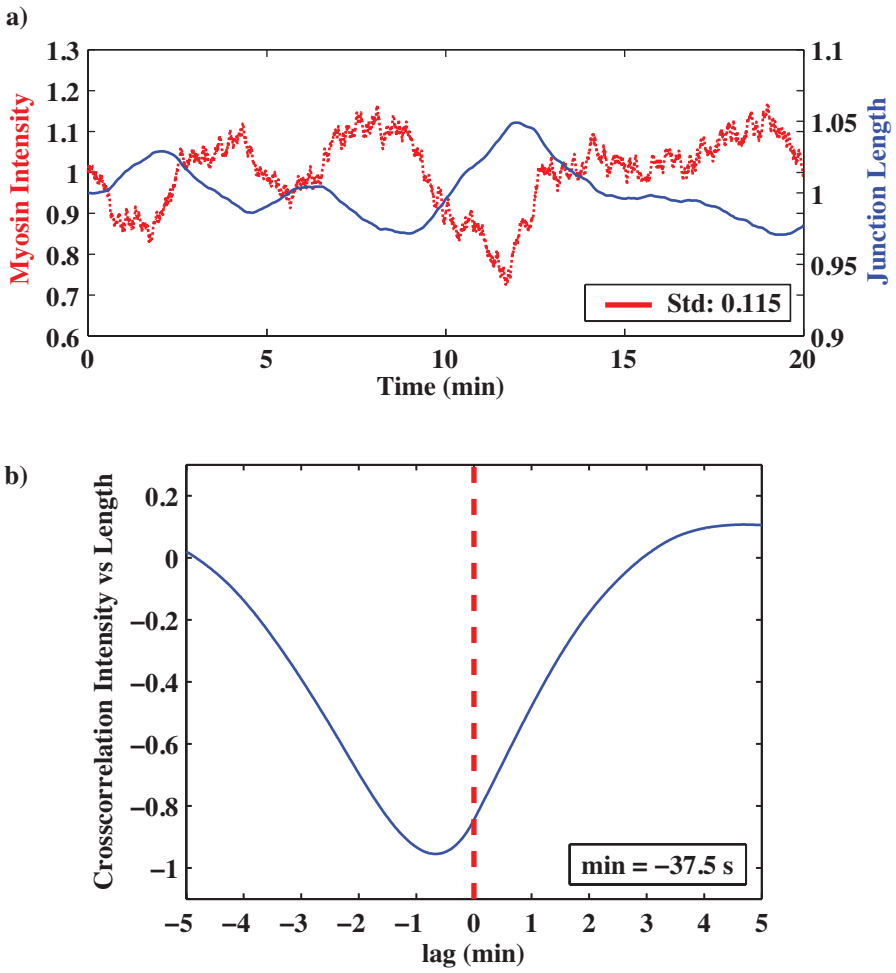

Figure 7.5: Myosin model

a) Simulated data for the fluctuation of myosin intensity and junction length from the system of equations in 7.17. **b)** Mean crosscorrelation for myosin intensity and junction length for 100 realizations of the system of equations in 7.17 with nondimensional parameters $\mu/(k_1 * \tau) = 0.28$ and $t_1 * c_0/(k_1 * l_0) = 0.3$. The noise level is set to $\xi = 0.3$. The nondimensional time is translated into minutes using the experimental value of $\tau = 3.48$ min for the turnover time of myosin. The minimum for the crosscorrelation function occurs at -37.5 min.

As shown in Figure 7.5, for at least one combination of parameters, the model is able to reproduce the Myosin II time traces and crosscorrelation function for the experimental data. Rather than attempt to fit the model parameters, we want to investigate which parameter regions give rise to the asymmetry in the crosscorrelation function. This is done by scanning over combinations of the nondimensional parameters α and β and calculate the position of the minimum in the mean crosscorrelation function. In Figure 7.6, the results are presented as a heatmap. The minimum is given in units of minutes using Eq. 7.19 and $\tau = 3.48$ min. The collapse of the system occurs for the same combination of parameters as reported in Dierkes et al. [103]. The position of the minimum is negative for all combinations of parameters, demonstrating that the asymmetry in the crosscorrelation function is a general qualitative feature of the model. This supports our interpretation of a causal role for Myosin II in regulating junction dynamics. In addition, it demonstrates that the observed interaction between Myosin II and junction length can be explained by stochastic turnover in conjunction with tension. The region of parameter space, where the model has the same position of the minimum as in experiment, is at $\mu/k_1\tau \sim 0.5$, corresponding to the viscous damping and elastic restoring force having the same order of magnitude.

As in Dierkes et al. [103], we observe oscillations in both myosin and junction length in the region above the Hopf bifurcation at $(t_1 c_0)/(k_1 l_0) = 1 + \mu/(k_1\tau)$. Whether these are visible as distinct oscillations or are obscured by the stochastic fluctuations of the system, depends on the noise strength. Hence, the appearance of oscillations in the system corresponds to high levels of myosin and low levels of noise.

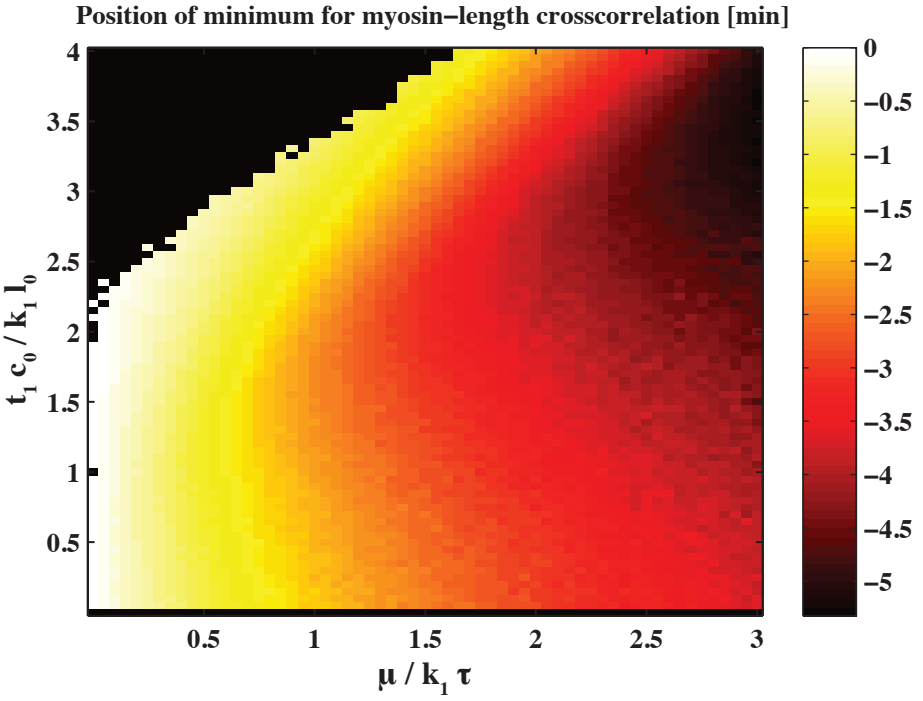

Figure 7.6: Myosin model, crosscorrelation minimum

For the system of equations in 7.17, the nondimensional parameters $\mu/(k_1 * \tau)$ and $t_1 * c_0/(k_1 * l_0)$ were varied and the mean crosscorrelation function (of 5 realizations) was calculated. The heatmap shows the position of the minimum for each combination of parameters. The noise level is set to $\xi = 0.1$. For the black region in parameter space (upper left corner), the systems collapses. The position of the minimum is negative for the range of parameters investigated. For the region of parameter space with $\mu/k_1\tau \sim 0.5$, the position of the minimum in the crosscorrelation function in the model is the same as in experiment.

7.6 Discussion

Our analysis showed that, in the *Drosophila* notum, the spatial distribution of Myosin II is unpolarized with respect to junction orientation. This is in contrast to the embryonic germ band, where a planar polarized distribution of Myosin II causes oriented cell intercalation, with junctions shrinking along the D-V axis and expanding along the A-P axis, leading to an overall elongation of the tissue. As discussed in section 4, disruption of the polarized action of Myosin II in the germ band results in neighbour exchange dynamics that resemble what we observe in the notum. In *Kr* mutant embryos and *Kr(RNAi)* embryos, neighbour exchange events are not polarized in the plane of the epithelium and junction remodelling is reversible[53, 54, 92]. This suggests that planar polarization of Myosin II introduces a bias into the system and may be considered a special case of a more general mechanism.

Tracking the fluorescence intensity on individual junctions over time allowed us to extract temporal information about Myosin II dynamics. We found that the decay of the fluorescence intensity autocorrelation is exponential, which is consistent with simple first order binding kinetics for Myosin II molecules to the actin network. So although we did see some evidence of binding cooperativity in how the standard deviation of Myosin II fluctuations scales with the mean amount of Myosin II on junctions, the results suggest that this can be ignored for the purposes of modelling. The turnover time for Myosin II was measured to be 3.48 ± 0.093 min, which is similar to the value of 108 ± 66 s reported in [103] for dorsal closure in the *Drosophila* embryo. The crosscorrelation function for Myosin II intensity and junction length is distinctly asymmetric with a minimum at -35 s, which shows that changes in Myosin II intensity preceede changes in junction length. Interestingly, the same asymmetry has been reported for junctional Myosin II intensity during the extension phase of junction remodelling in germ-band elongation with a lagtime of -40 s [104]. As a control, there was no asymmetry in the crosscorrelation function for Bazooka intensity and junction length. The result for Myosin II is non-trivial and suggests a causal role for Myosin II in regulating junction length fluctuations.

Based on a stochastic model, we were able to show that the asymmetry in

the crosscorrelation can be explained by stochastic turnover of Myosin II in conjunction with tension being a function of the concentration of Myosin II on a junction. This supports our interpretation of a causal role for Myosin II. Importantly, the asymmetry is a general qualitative feature of the system and does not depend on the choice of parameters. Looking more specifically at the position of the minimum points to a region of parameter space where $\mu/k_1\tau \sim 0.5$, indicating that the viscous damping and elastic restoring force are of the same order of magnitude.

Our question at the start of this chapter was: what is the source of stochasticity and how do junction fluctuations arise in the tissue? The model suggests that the stochastic behaviour of junctions, which we quantified in section 5, can be explained by stochasticity in the turnover of Myosin II. This prompts us to ask how changing the level of Myosin II in the tissue would affect junction fluctuations and neighbour exchange events. This will be the focus of the next section.

Since the model in this chapter was based on published work by Dierkes et al. describing dorsal closure [103] and the crosscorrelation timescale for our data agrees with what has been reported in germband extension[104], our results show that Myosin II dynamics in the notum are similar to what is observed in other processes in the *Drosophila* embryo. As we will see in the next section, the same behaviour of Myosin II on the molecular level can have very different effects at the tissue level depending on whether the spatial distribution is polarized or not.

Chapter 8

The role of Myosin II in neighbour exchange events

The previous section demonstrated that noisy junction length fluctuations can be explained by stochasticity in the turnover of Myosin II. We now turn to how Myosin II affects neighbour exchange events. The aim is that by perturbing Myosin II, we are able to elucidate how it contributes to ordering of the tissue over the course of pupal development. In particular we quantify the frequency of neighbour exchange events in mutants with altered levels of Myosin II and attempt to explain the differences we observe. In germ band elongation, planar polarized Myosin II drives neighbour exchange and a decrease in the level of Myosin II is associated with fewer neighbour exchange events [57]. It is unclear how altering the level of Myosin II would affect the rate of neighbour exchange in the notum given the isotropic spatial distribution of Myosin II.

Both reduction and overexpression of Myosin II were achieved in two different ways (see [Curran 2015] for additional details).

- *Drosophila* Rho-kinase (Rok) regulates the phosphorylation of the myosin regulatory light chain (MLRC) and thereby the activity of Myosin II. We used RNA-mediated interference to inhibit Rok (UAS-Rok^{RNAi}) and reduce Myosin II levels in the tissue. Conversely, a constitutively active version of Rok (UAS-Rok^{CAT}) was expressed to increase Myosin II levels.

- The *Drosophila* spaghetti squash (sqh) gene encodes the myosin regulatory light chain of Myosin II. Expression of a non-phosphorylatable, and therefore inactive, form of MRLC (UAS-sqh^{AA}) results in a loss of Myosin II

from the tissue. The opposite phenotype was acheived by expressing a phosphomimetic form of MRLC that is constitutively active (UAS-sqh^{EE}).

8.1 The frequency of neighbour exchange events is inversely proportional to Myosin II levels

To quantify the frequency of neighbour exchange events, I use the software described in Methods to detect every time a cell changes neighbours. To avoid overcounting from segmentation errors, I manually checked every computationally detected event by looking at the fluorescent time-lapse images and only including clear neighbour exchange events. Figure 8.1 shows the frequency of neighbour exchange events for both Control and mutant phenotypes. Interestingly, the frequency scales inversely with the level of Myosin II in the tissue. Loss of active Myosin II from the tissue, whether by Rok^{RNAi} or sqh^{AA}, increases neighbour exchange and a gain in Myosin II, through either Rok^{CAT} or sqh^{EE}, reduces neighbour exchange in the tissue. The differences are striking with neighbour exchange events being 3.6 times as common in Rok^{RNAi} than Rok^{CAT}. This is opposite to what is observed in germ band elongation, where a decrease in Myosin II - by expression of sqh^{AA} - results in fewer neighbour exchange events [57].

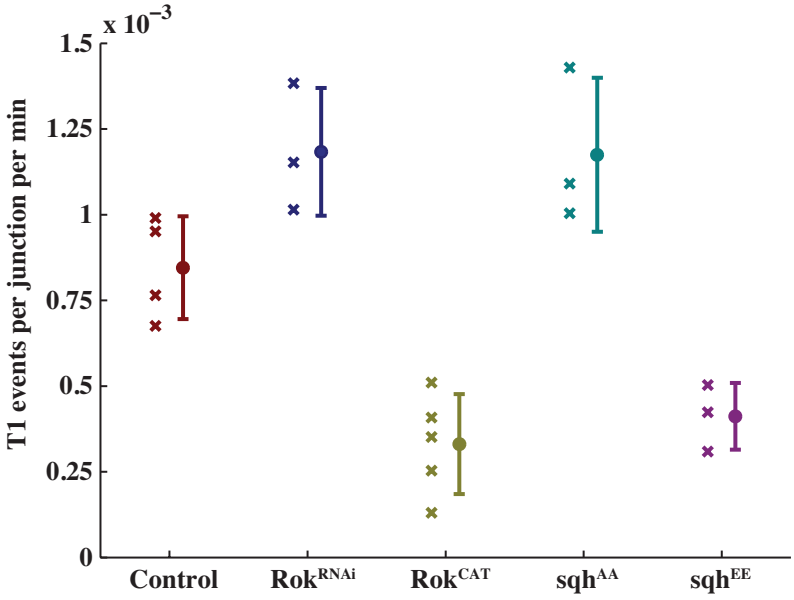

Figure 8.1: Frequency of neighbour exchange events

Frequency of neighbour exchange events. The neighbour exchange events have been detected computationally, with the settings set to include all potential events. Each event was then checked manually, by looking at the fluorescent images, using the criterion that the extension of the junction, following a four-way vertex configuration, should be stable and clearly visible from the images. To calculate the frequency, the number of neighbour exchange events has been normalized by the total number of junctions in each tissue (excluding border junctions) and the length of the movie in minutes. The figure includes data from Control ($N = 4$ nota), Rok RNAi ($N = 3$ nota), Rok CAT ($N = 5$ nota), SqhEE ($N = 3$ nota), and SqhAA ($N = 3$ nota). The errorbars indicate the standard deviation among nota. The mean values are: $0.85 \pm 0.150 \times 10^{-3}$ (Control), $1.18 \pm 0.186 \times 10^{-3}$ (Rok RNAi), and $0.33 \pm 0.146 \times 10^{-3}$ (Rok CAT).

8.2 A reduction in Myosin II makes neighbour exchange events more reversible

We are also interested in how Myosin II affects the reversibility of neighbour exchange events. As in section 4, we calculate the Kaplan-Meier survival curves to quantify the probability that the configuration created by a neighbour exchange event persists, without reverting back, for at least a time t. The advantage of this approach is that it allows us to combine data from movies of different lengths and take into account that a neighbour exchange at the start of a movie is observed for longer than one occuring towards the end. To help build intuition for what the data looks like, Figure 8.2 includes bar charts showing the proportion of neighbour exchange configurations that persists for the duration of each movie versus those that reverse. We class neighbour exchange events where the configuration persists as unidirectional. It is interesting that in Rok RNAi we occasionally observe the same junction undergoing up to four consecutive neighbour exchange events. The bar charts suggest that Myosin II reduces reversibility and this is borne out by the Kaplan-Meier analysis.

From the survival curves, we can extract the probability that a neighbour exchange configuration persists for at least 150 min in each tissue type. That probability is 69% in Control, 26% in Rok RNAi embryos, where Myosin activity is low, and 82% in Rok CAT embryos, where Myosin activity is high. The appropriate statistical test for comparing the survival curves of two samples is the log-rank test. It is a nonparametric hypothesis test that deals with censored data and considers the null hypothesis that there is no difference between the survival curves - i.e. at any time point the probability of reversing is the same for each tissue type. The log-rank test shows that the difference is statistically significant for Control and Rok RNAi ($p = 0.00041$), but not for Control and Rok CAT ($p = 0.27399$). Although, with the frequency of neighbour exchange events being lower in Rok CAT, there is considerably less data available for this analysis. The results demonstrate that an increase in junctional levels of Myosin II makes neighbour exchange events less reversible.

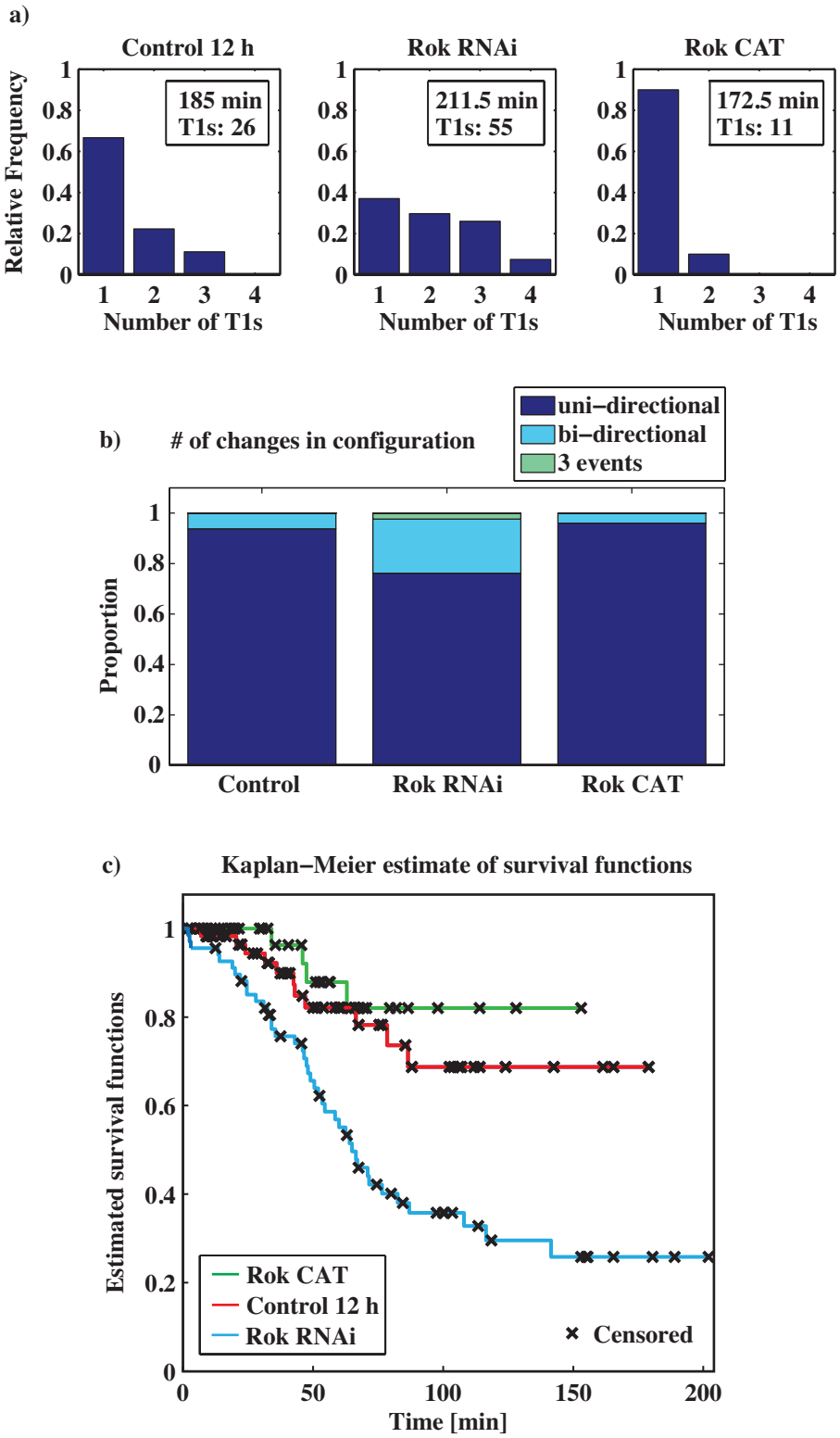

Figure 8.2: Reversibility of neighbour exchange events

a) Bar charts showing what proportion of junctions undergo unidirectional, bidirectional, and multidirectional neighbour exchange events. For each tissue type, the longest available movie was chosen. **b)** Same as in a), but in a stacked bar chart. Each movie has been truncated at 75 min to make a direct comparison possible. $N = 48$ junctions / 51 T1 events, 4 nota (Control). $N = 42$ junctions / 53 T1 events, 3 nota (Rok RNAi). $N = 25$ junctions / 26 T1 events, 5 nota (Rok CAT). **c)** Kaplan-Meier survival curves showing the probability that a neighbour exchange event is unidirectional for a given length of time. From the survival curves, the probability of a configuration persisting for at least 150 min, along with the 95% confidence interval, is: Control 0.687 [0.5175 0.8567], Rok RNAi 0.258 [0.1250 0.3915], Rok CAT 0.821 [0.6572 0.9841]. A log-rank test is used to determine if differences between the survival curves are statistically significant. Control vs Rok RNAi $p = 0.00041$ (*), Control vs Rok CAT $p = 0.27399$ (ns). In addition, for Rok RNAi, there is sufficient data to calculate a median time for the persistence of a neighbour exchange configuration: 64.8 min.

8.3 Regulation of the frequency of neighbour exchange events

There are two possible hypotheses for explaining the observed differences in the frequency of neighbour exchange events. The requirements for a neighbour exchange event to occur are that a junction contracts to a four-way vertex configuration and that the four-way vertex is resolved to give a change in cell neighbours. So either (i) Myosin II changes the fluctuation of junctions and affects how frequently junctions reach a four-way vertex configuration or (ii) Myosin II affects the probability of successfully going through a neighbour exchange once at a four-way vertex.

We start by exploring the first hypothesis. As we established in section 5 and 7, neighbour exchange events are indistinguishable from stochastic junction fluctuations and those fluctuations are regulated by Myosin II. Hence, a change in the level of Myosin II in the tissue could alter junction fluctuations. In the following sections I quantify junction fluctuations, using various statistical measures, and compare Control and mutant phenotypes.

8.3.1 The variation of junction lengths is similar in Control, Rok^{RNAi}, and Rok^{CAT}

To start with, we simply consider the variation of junction lengths, both within the tissue and over time, as shown in Figure 8.3. The temporal variation is quantified by calculating the standard deviation over the mean for individual junctions and grouping the data by tissue type. The median value is slightly higher for Rok CAT. However, two things are worth noting about the Rok CAT phenotype. Firstly, increasing Myosin II levels induces discontinuities in the adherens junctions with DE-cadherin missing, particularly at vertices. In addition, DE-cadherin was seen to be lost from the four-way vertex during neighbour exchange events. The same effect was observed in sqh^{EE} and appears to be phenotypical of increased Myosin II activity [Curran 2015]. The discontinuties makes segmentation more difficult and, hence, the junction fluctuation analysis for Rok CAT is more impacted by segmentation errors than either of the other tissue types. Secondly, in three of the

five Rok CAT embryos, we saw significant local deformations of the tissue[1]. Such deformations cause junctions to undergo directed contraction and expansion, making the fluctuations appear ballistic. This increases the standard deviation of individual junctions and, as we shall see in the next section, affects the mean square displacement. It is not clear what induces deformation of the tissue.

For the spatial variation, calculated as the standard deviation of junction lengths divided by the population mean at a single time point, the difference between tissue types is not statistically significant and there is no significant change over a period of 75 min. The results demonstrate that the variation in junction lengths are not able to explain differences in the frequency of neighbour exchange events. Nonetheless, even if the overall variation is the same, differences in junction dynamics might be important.

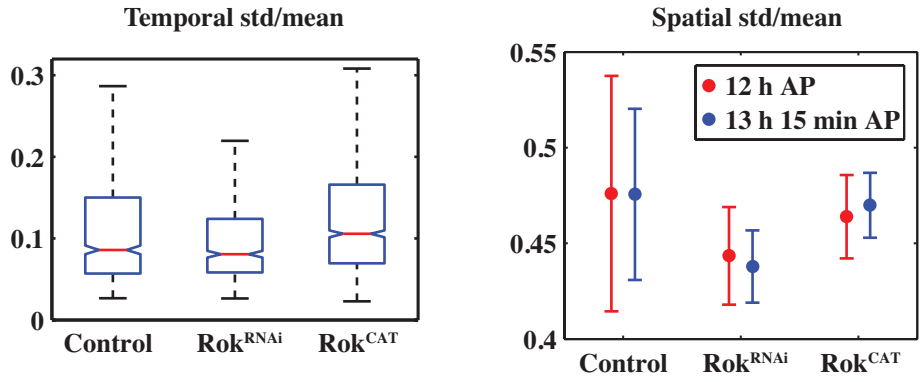

Figure 8.3: Standard deviation of junctions

a) Boxplots of the standard deviation for the lengths of junctions over time. For each junction, $\sigma/\langle l \rangle$ is calculated from the junction length time series. Since the standard deviation varies with the length of the movie, all time series are truncated at 75 min. The data shown is for Control ($N = 4$ nota), Rok RNAi ($N = 3$ nota), Rok CAT ($N = 5$ nota). **b)** Standard deviation over population mean for junction lengths within the tissue at two different time points, 12h AP and 13h 15min AP. The errorbars indicate the standard deviation among embryos.

8.3.2 The mean square displacement curves are similar for Control and mutants

The dynamics of junction fluctuations can be quantified used mean square displacement (MDS) analysis. The method is described in section 5. Our model

[1]The deformations within the tissue were quantified using Optical Flow Analysis. See Chapter 3

for the dynamics of junction length changes, resembles an Ornstein-Uhlenbeck process (with an additional coupling term from tension generated by Myosin). The mean square displacement for an Ornstein-Uhlenbeck process is given by

$$f(\Delta t) = 2D\tau^*(1 - \exp^{\left(-\frac{\Delta t}{\tau^*}\right)}) \tag{8.1}$$

where the time scale $\tau*$ is defined by the ratio of the viscous damping term and the elastic restoring force α/K. The term D is the diffusion coefficent and represents the magnitude of the stochastic input to the system. From this, the mean square displacement saturates at a value of $2D\tau^*$ and this value scales inversely with the elastic restoring force, or stiffness, of the tissue. Hence, based on tension measurements (see [Curran 2015]), we expect Rok RNAi to saturate at a higher value than Control and Rok CAT to saturate at a lower value.

Figure 8.4 shows the ensemble-averaged mean square displacement curves for Rok RNAi and Rok CAT, with Control on the same graph for comparison. The initial jump at the first time point is from segmentation errors and is, as expected, larger for Rok CAT. Both Control and Rok RNAi display subdiffusive behaviour, with Rok RNAi approaching a higher saturation value. Surprisingly, the curve for Rok CAT is almost linear and, contrary to our expectation, placed above Control. Visual inspection of the MSD curves for individual junctions reveal that they display a wide range of behaviours - some saturate, some are ballistic, and some have other more complicated dynamics. It is therefore not the case that the majority of junctions in Rok CAT tissue have linear mean square displacement curves, but rather that a few ballistic junctions bias the ensemble-average. As discussed in the previous section, this could be related to the local deformation of the tissue observed in Rok CAT.

Separating the fluctuations caused by local deformations from the fluctuations intrinsic to the junction has proved to be highly non-trivial. Documenting the various approaches I have tried are beyond the scope of this thesis, but have included subtracting the local deformation (using the velocity field extracted from Optical Flow Analysis) before calculating the mean square displacement and looking at the correlated and uncorrelated components of the time series of

neighbouring junctions. Overall, there are indications that, without the pertubing effect of local deformations, the mean square displacement curve for Rok CAT might saturate at a lower value than Control. However, in the absence of either data free from tissue deformations or a rigourous method for separating the components of fluctuations, this will have to remain an open question.

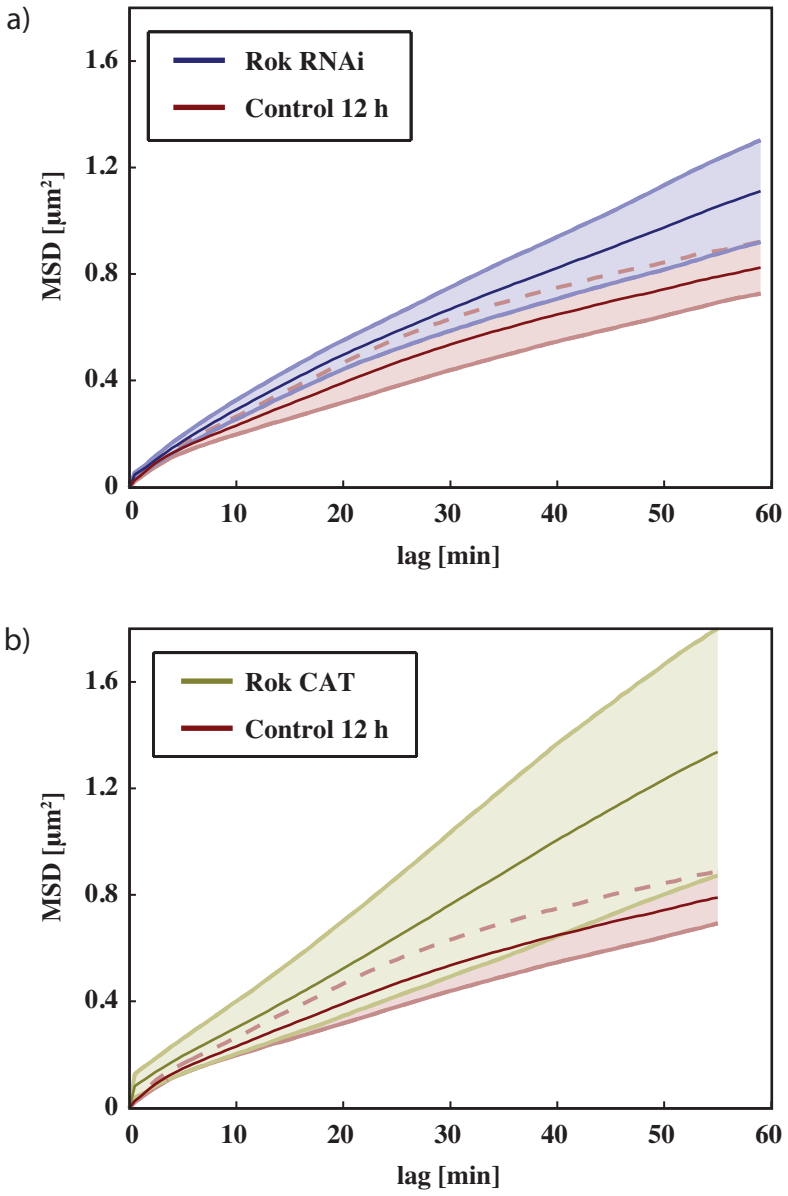

Figure 8.4: Mean square displacement curves

Ensemble-averaged MSD curves for **a)** Rok RNAi ($N = 3$ nota), **b)** Rok CAT ($N = 5$ nota). The ensemble-average is calculated for each notum separately, then the average for each tissue type is calculated. The errorbars shown are the standard deviation for the ensemble-averages for nota of the same type, and therefore reflects the embryo-to-embryo variability rather then the within-embryo variability. The MSD curve for Control ($N = 4$ nota) is included in each figure for comparison.

8.3.3 Myosin II slightly reduces the diffusion coefficient of junction fluctuations

Even though the MSD curves for individual junctions display a complicated range of behaviours, they all start out linear. This makes it possible to extract the diffusion coefficient by fitting a straight line to the initial slope. The number of datapoints used for the fit can affect the diffusion coefficient (see [95, 96]). I use the first 5 min / 10 frames.

Figure 8.5 shows the diffusion coefficients for different tissue types. For each junction, the MSD curve is calculated and the diffusion coefficient is extracted. As shown in panel (a, right), a straight line provides a good fit to the data. The resulting diffusion coefficients are then combined by tissue type to give the distributions shown in panels (b-e). This approach provides stronger statistical support than a single fit to the ensemble-averaged MSD curve. Particularly for Control 25 h and Rok CAT, the distributions are heavily left-skewed, I therefore use the median value to get a more representative estimate for the diffusion coefficient. Figures 8.5(f) shows the median values with errorbars given by the 95 % confidence interval, which for every data set is larger than the standard error on the median.

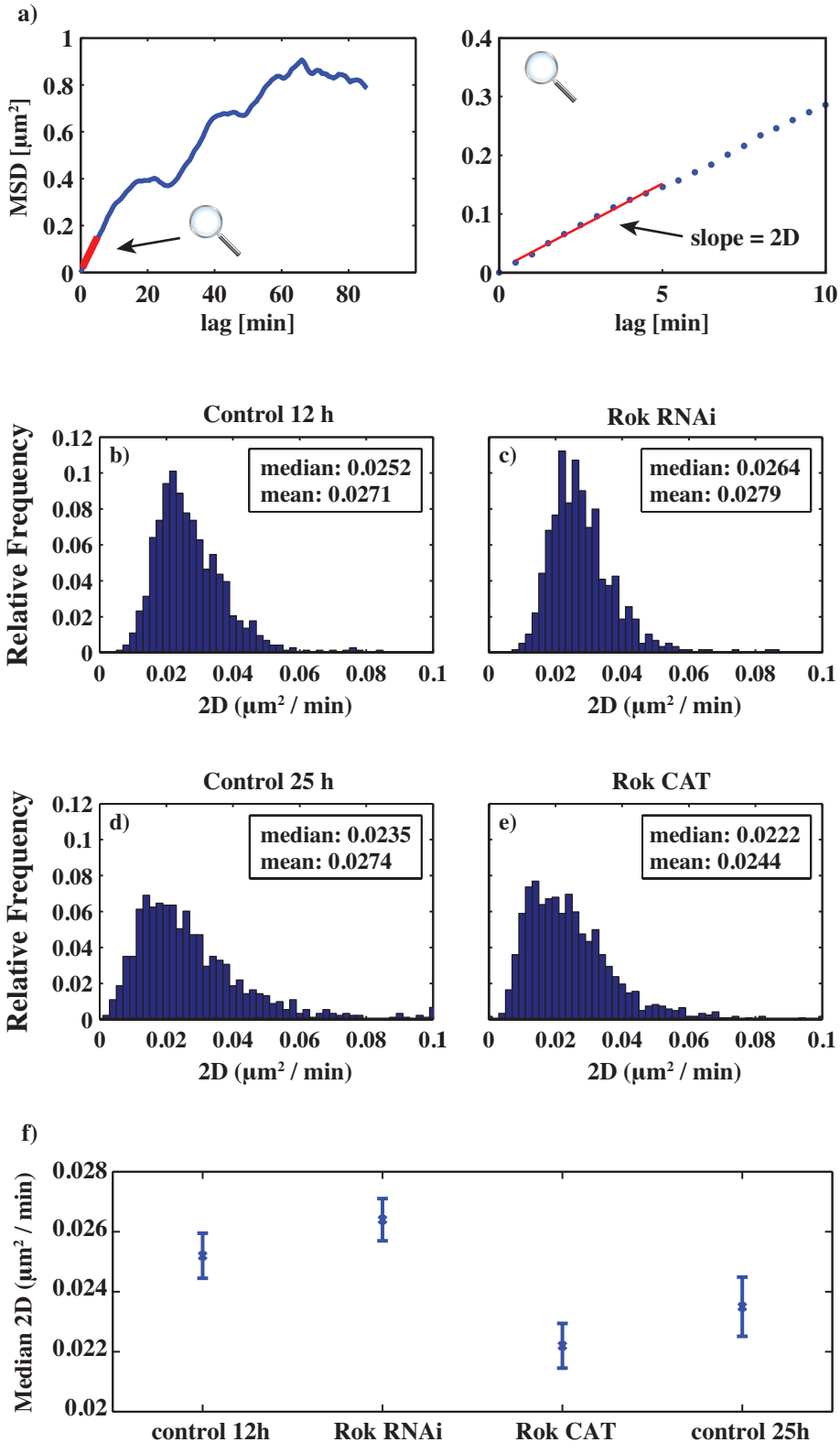

Figure 8.5: Diffusion coefficients estimated from MSD curves

a) (left) Example of an MSD curve for a single junction. The diffusion coefficient is determined by fitting a straight line - shown in red, to the first 10 frames / 5 min of the curve. (right) Zoom on the first part of the MSD curve, showing the goodness of fit. **b) - e)** The resulting distributions of diffusion coefficients, with the data grouped by tissue type for Control ($N = 733$ junctions, 4 nota.), Rok RNAi ($N = 588$ junctions, 3 nota.), Control 25 h ($N = 913$ junctions, 3 nota.), and Rok CAT ($N = 1222$ junctions, 5 nota.). **f)** Plot of the median diffusion coefficient, from the distributions shown. The errorbars are the 95% confidence interval for the median. All data is for the actual junction length, as oppose to the vertex-vertex distance.

Errorbars on the median:

For large samples from normal distributions, the standard error of the median is:

$$\sigma_{median} = 1.253 * \frac{\sigma_{mean}}{\sqrt{N}} \tag{8.2}$$

However, this is not accurate for non-normal distributions. For such distributions the standard error of the median is difficult to compute [Sokal, 1995]. Instead, appropriate errorbars may be calculated from the interquartile range (R) of the data, as this is a robust measure of the spread, and the number of observations (N). The 95 % confidence interval for the median is given by

$$\pm 1.57 * \frac{Q75 - Q25}{\sqrt{N}} \tag{8.3}$$

where $Q25$ and $Q75$ are the 25th and 75th percentiles respectively. The value of 1.57 was emperically selected as the appropriate value for non-normal distributions [108].

We can test whether the differences between the medians are statistically significant. The Wilcoxon rank-sum test is nonparametric and tests the null hypothesis that data in, say, $y1$ and $y2$ are samples from continuous distributions with equal medians, against the alternative that they are not. Table 8.1 shows outcomes at the $p = 0.01$ significance level - H_1 indicates that the null hypothesis of equal medians has been rejected.

Table 8.1

	Control	Rok RNAi	Rok CAT	late
Control	..	p = 0.0346 , H_0	p < 0.00001 , H_1	p = 0.0014 , H_1
Rok RNAi	..	..	p < 0.00001 , H_1	p < 0.00001 , H_1
Rok CAT	..	..	..	p = 0.0014 , H_1
late	..	..	..	..

The medians of Control and Rok RNAi are significantly different from Rok CAT. For Control and Rok RNAi the difference is significant at 5% significance level, but not 1%. However, the diffusion coefficient of Rok CAT is only around

15% lower than Rok RNAi. While this could contribute to a decrease in the rate of neighbour exchange events, it is not clear that it would be sufficient to give the observed threefold reduction.

8.3.4 Junction fluctuations are mean-reverting, but the degree does not depend on Myosin II

Another way we can attempt to capture differences in the dynamics of junctions, is to look directly at mean reversion. If an increase in Myosin II causes junction fluctuations to be more mean reverting it would reduce the likelihood of reaching a four-way vertex configuration and could explain differences in the frequency of neighbour exchange events.

Unlike a random walk, where the position is unbounded, a mean-reverting process tends towards some equilibrium value. The Ornstein-Uhlenbeck process is an example of such a process that consists of random fluctuations with a bias that depends on its current value - above the (long term) mean the bias is negative and below it is positive, causing the process to revert towards its (long term) mean. Simply based on spatial constraints (cells cannot become arbitrarily large), we would expect junctions to be mean-reverting. From the mean square displacement curves it is not clear whether junctions in Rok RNAi and Rok CAT nota display mean-reverting behaviour[2]. Instead, we can analyse the mean reverting behaviour directly by looking at how the length change at a given point in time depends on the current length of the junction, as shown in Figure 8.6. The figure is based on the method described in section 5. The time series for each junction is split into segments where the junction length is monotonically increasing/decreasing and the persistence length is defined as the signed change in length for each segment - i.e. contraction corresponds to a negative persistence length. The figure shows a clear bias in the persistence length with longer junctions being more likely to contract and shorter junctions being more likely to expand than predicted by the baseline expection of a random walk[3]. Hence, junctions display clear mean

[2]For a random walk, the mean absolute displacement is $\langle|\delta l|\rangle = \sqrt{2Dt}$. Given the measured diffusion coefficient of $0.01\ \mu m^2/min$ and an average junction length of $4\ \mu m$, the expected time for a junction to double in length is 800 min or around 13 hours. Hence, it is not unexpected that the spatial constraints become evident in the mean square displacement curves only on time scales longer than the duration of these movies.

[3]It would be interesting to use exact shape of the mean reversion to elucidate nature of the

reverting behaviour. Interstingly, there does not appear to be a difference in the degree of mean reversion for Control, Rok RNAi, and Rok CAT.

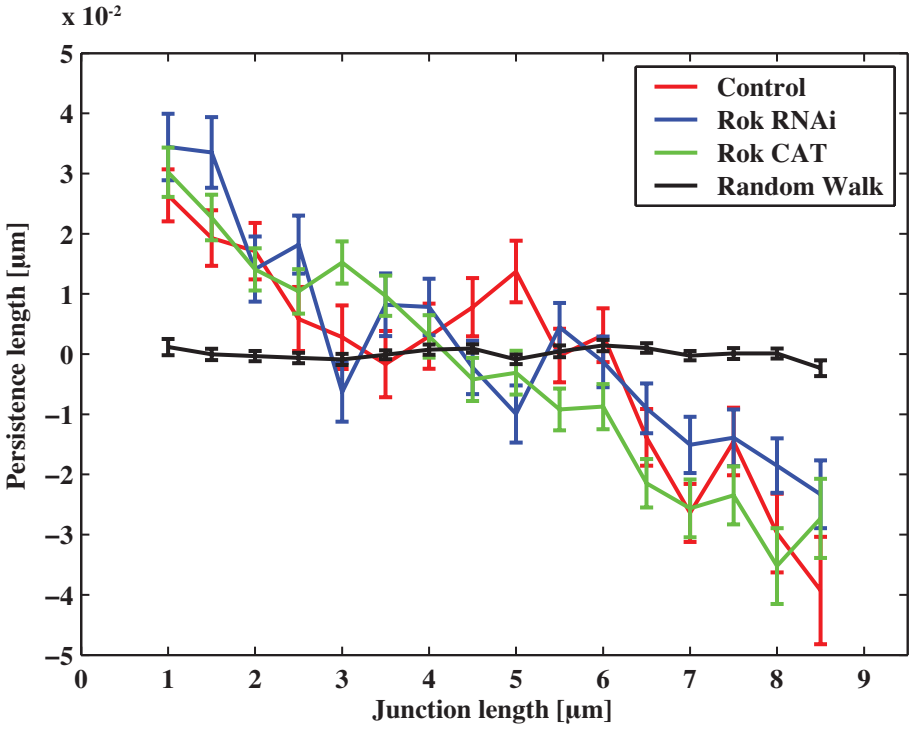

Figure 8.6: Mean reversion of junction length fluctuations

The figure shows the persistence length as a function of junction length. The persistence length is calculated, as described in section 5, by splitting the time series into segments where the junction length is monotonically increasing/decreasing and taking the the change in length for that segment. The corresponding junction length is the length at the start of each segment. The filter is a moving average Hanning window with a width of 5. Carrying out the analysis for filters with width 10 and 20 gave the same dependence on junction length, as did calculting the length change for a time window of set size. Data from Control ($N = 60737$ segments, 1519 junctions, 4 nota), Rok RNAi ($N = 83152$ segments, 1187 junctions, 3 nota), and Rok CAT ($N = 116439$ segments, 1960 junctions, 5 nota), are shown. The data has been binned and errorbars are the standard error on the mean. In addition, the result is shown for 300 realizations of a simulated random walk, with a diffusion coefficient of $D = 0.01$ µm^2/min and a time series length of 250 min.

'attractive force'. I.e. is it greater when the process is further away from the equilibrium value, as would be the case for a spring, or is it uniform with a strong boundary effect at some value? However, we will not be investigating this further in this thesis.

8.4 The frequency of neighbour exchange events can be explained by the probability of successful junction remodelling once at a four-way vertex

The methods for quantifying junction fluctuations, described in the previous section, show little difference between Control and the mutants with increased/decreased p-Myosin II levels. We observed a small, but significant, difference in the diffusion coefficients, indicating that - at least on short time scales - Myosin II inhibits junction fluctuations. However, it is not clear whether such differences are functionally important. Instead, we turn to the second hypothesis and investigate the probability of successfully going through a neighbour exchange event once a four-way vertex configuration has been reached.

We will refer to events where a junction shrinks to a four-way vertex, regardless of the eventual outcome, as 'attempted' neighbour exchange events. These events are detected computationally and, as in section 5, I set the threshold at which a four-way vertex is reached at 0.5 μm. When a junction shrinks down to a four-way vertex it is counted as a single event regardless of how long the configuration persists for. Figure 8.7 shows the ratio of successful and attempted neighbour exchange events, as well as the frequency of attempted events, for each tissue type. In addition, the total counts and frequencies are shown in Table 8.2.

Strikingly, the frequency with which junctions reach four-way vertex configurations is the same in each of the three tissue types. Consequently, differences in junction fluctuations cannot explain the observed differences in the rate of neighbour exchange events. This is consistent with the previous section where we found only small differences in the junction fluctuations of Control and mutant embryos.

Instead, the frequency of neighbour exchange can be explained entirely by the probability of successful junction remodelling at the four way vertex. Specifically, in Control 28% of four-way vertex configurations are resolved by neighbour exchange, whereas the numbers for Rok RNAi and Rok CAT are 42% and 12%, respectively. So the probability of successfully going through a four-way vertex is 3.6 times higher in Rok RNAi than in Rok CAT - the same as the ratio of the rates

of neighbour exchange in these tissues.

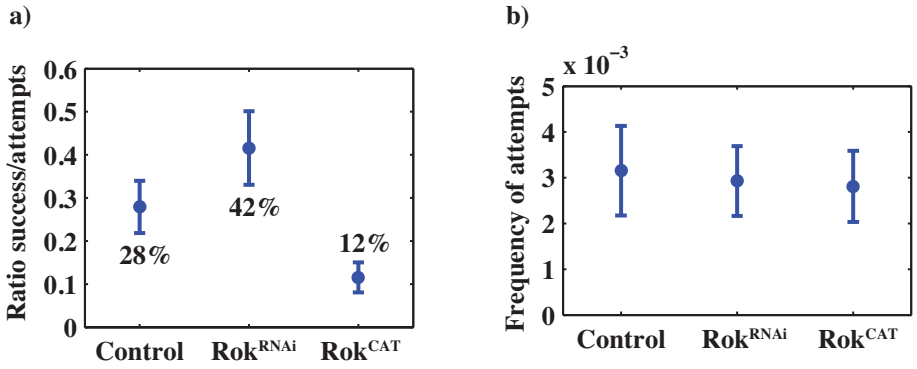

Figure 8.7: Frequency of attempted neighbour exchange events

a) The percentage of four-way vertex configurations that result in a neighbour exchange event. **b)** Frequency of all events where a junction shrinks to a four-way vertex, irrespective of whether the configuration is resolved by neighbour exchange. The frequency is normalized by the total number of junctions in the tissue and the length of the movie, giving units of events/(junction*min). Based on a two-sample t-test, there is no statistical difference between the means: Control vs Rok RNAi $p = 0.7525$ (ns), Control vs Rok CAT $p = 0.5740$ (ns), Rok RNAi vs Rok CAT $p = 0.8450$. The data is for $N = 4$ nota (Control), $N = 3$ nota (Rok RNAi), and $N = 5$ nota (Rok CAT). The numbers from the figures are shown in Table 8.2.

	Control	Rok RNAi	Rok CAT
Full T1s	74	131	49
Attempted T1s	273	329	400
Ratio full/attempted	0.279 ± 0.0605	0.416 ± 0.0854	0.116 ± 0.0347
Full T1 frequency $\times 10^{-3}$	0.845 ± 0.1499	1.183 ± 0.1864	0.331 ± 0.1457
Attempted T1 frequency $\times 10^{-3}$	3.154 ± 0.9782	2.926 ± 0.7626	2.811 ± 0.7767

Table 8.2: Total counts and frequencies for full and attempted neigbhour exchange events in Control, Rok RNAi and Rok CAT. The frequency is normalized by the total number of junctions in the tissue and the length of the movie, giving units of events/(junction*min). Note that the ratio, T1 frequency and attempted T1 frequency are calculated as the mean of the values for the individual nota. Hence, the mean ratio differs slightly from taking the ratio of the total number of full T1s and attempted T1s. Errorbars are the standard deviation between individual nota. Since the data for each nota differs with respect to the duration of imaging and the size of the tissue within the frame, the total numbers for full T1s and attempted T1s cannot be directly compared.

8.5 Myosin II regulates neighbour exchange events late in development

As we saw in Chapter 6, tissue packing in the notum becomes more regular over the course of development. Post division, the proportion of hexagonal cells in the

tissue increases and the variance of the polygon distribution decreases.

The previous results on neighbour exchange in mutant phenotypes, showed that Myosin II significantly inhibits junction remodelling. This suggests the hypothesis that the gradual increase in junctional Myosin II over developmental time is regulated to drive the ordering of the tissue to its hexagonally packed configuration. To address this, I analyzed unperturbed neighbour exchange events and junction fluctuations in the notum at a later point in development.

Figure 8.8 compares junction remodelling at 12 h and 25 h AP. The frequency of neighbour exchange events is reduced by a factor 2.7 and events are less reversible; the probability that a neighbour exchange configuration persists for at least 65 minutes increases from 0.82 [0.707 0.936] at 12h to 0.93 [6.807 1] at 25 h AP. We note that the results for the notum at 25h AP and Rok CAT at 12h AP are similar. In fact, there is no statistical difference between the frequencies ($p = 0.8485$) or Kaplan-Meier survival curves ($p = 0.1765$) for Control 25h and Rok CAT. As shown in Figure 8.5, for both Rok CAT and the unperturbed notum at 25 h AP, the distribution of diffusion coefficients is heavily left-skewed with a median value that is significantly lower than Control 12 h.

The similarity in results was expected since overexpression of Myosin II activity in Rok CAT mirrors the developmental increase Myosin II at junctions. The correspondence between the Rok CAT phenotype at 12h and the notum at 25h establishes that Myosin II has a primary role in regulating neighbour exchange.

I also quantified the frequency with which junctions shrink to a four-way vertex and, based on a two-sample t-test, found no statistical difference between the mean frequency early and late in development ($p = 0.1024$). In contrast, the probability of successful junction remodelling once at a four way vertex is significantly lower at 25 h AP (18%) compared to 12 h AP (28%). Again, the results late in development mirror those seen in the Rok CAT mutant phenotype, in which there is also a reduced probability of remodelling at four-way vertices (12%).

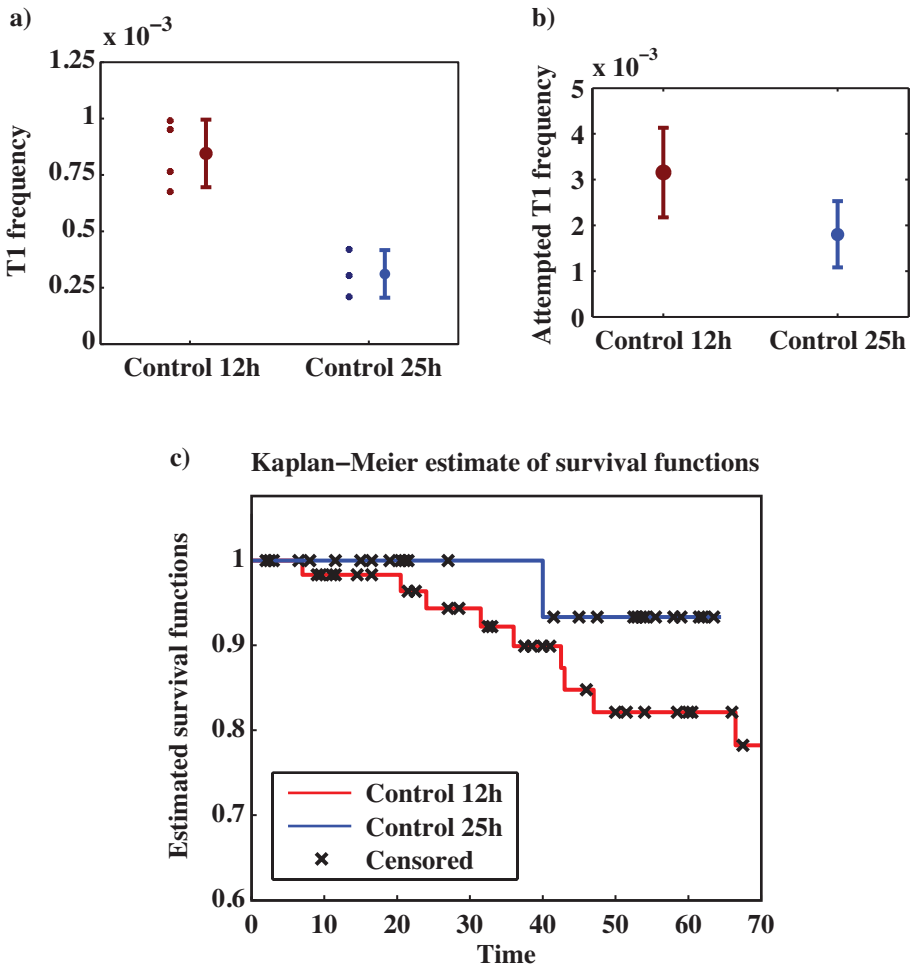

Figure 8.8: Results for Control 25h

a) Frequency of neighbour exchange events for Control 12 h ($N = 4$ embryos) and Control 25 h ($N = 3$ embryos). The neighbour exchange events have been detected computationally then checked manually. To calculate the frequency, the number of neighbour exchange events has been normalized by the total number of junctions in each tissue (excluding border junctions) and the length of the movie in minutes. The errorbars indicate the standard deviation among embryos. The mean values are $0.85 \pm 0.150 \times 10^{-3}$ (Control 12h) and $0.31 \pm 0.11 \times 10^{-3}$ (Control 25 h). **b)** Frequency of all events where a junction shrinks to a four-way vertex, irrespective of whether the configuration is resolved by neighbour exchange. The frequency is normalized by the total number of junctions in the tissue and the length of the movie, giving units of events/(junction*min). The mean frequencies are: $3.2 \pm 0.98 \times 10^{-3}$ (Control 12h) and $1.8 \pm 0.72 \times 10^{-3}$ (Control 25 h). Based on a two-sample t-test, there is no statistical difference between the means, $p = 0.1024$. The probability of successful junction remodelling once at a four way vertex, i.e. the ratio of successful to attempted T1s, is 0.2793 ± 0.0605 for Control 12h and 0.1838 ± 0.0709 for control 25h. **c)** Kaplan-Meier survival curves showing the probability that a neighbour exchange event is unidirectional for a given length of time. From the survival curves, the probability of a configuration persisting for at least 65 min, along with the 95 % confidence interval, is: Control 12 h 0.821 [0.7071 0.9356] and Control 25 h 0.933 [6.8071 1]. A log-rank test is used to determine if differences between the survival curves are statistically significant, giving $p = 0.044$ (1-tailed test) and $p = 0.088$ (2-tailed test).

8.6 Discussion

We started this chapter with the observation that the frequency of neighbour exchange events scales inversely with the level of Myosin II in the tissue. The difference is significant with neighbour exchange events being more than three times as common in Rok RNAi than Rok CAT. In addition to resulting in more neighbour exchange events, we found that a reduction in Myosin II causes neighbour exchange events to be more reversible, with the proportion of neighour exchange configurations that persists for longer than 150 min dropping from 69% in Control to 26% in Rok RNAi. Both these results are opposite to what is observed in the embryonic germ band. Kasza et al. (2014) report a decrease in the frequency of neighbour exchange events in sqhAA embryos, where myosin activity is reduced, with both a lower proportion of junctions contracting to a four-way vertex and a higher rate of vertices failing to resolve by neighbour exchange. For sqhEE embryos, where myosin activity is up, they see an increase in unstable neighbour exchange events that either reverse completely or contract back down to a four-way vertex. So unlike in the notum, in the germ band a decrease in Myosin II leads to fewer neighbour exchanges and an increase in Myosin II causes neighbour exchange events to be more reversible. It is very interesting that the action of Myosin II has such opposite effects in these two systems. A key difference is of course that the Myosin II is planar polarized in the germ band and not in the notum.

Focusing on the difference in the frequency of neighbour exchange events, we put forward two hypotheses. Either Myosin II changes junction fluctuations and this affects how frequently junctions contract to a four-way vertex or Myosin II changes the probability of acheiving neighbour exchange once at a vertex.

We did observe some differences in the junction fluctuations of Control compared to the mutants with altered Myosin II levels. In particular, we saw a small but significant difference in the diffusion coefficients, indicating that an increase in Myosin II dampens junction fluctuations on short time scales. The presence of local tissue deformations in Rok CAT mean that it is difficult to make any definite conclusions about the behaviour on longer time scales. However, we also found that the frequency with which junctions reach a four-way vertex configuration is

the same for Control, Rok RNAi and Rok CAT. Consequently, regardless of how Myosin II affects junction fluctuations, the observed difference in the frequency of neighbour exchange events can be explained entirely by the probability of successful junction remodelling at the four-way vertex.

It is not clear what the molecular mechanism is regulating junction remodelling at the four-way vertex. In all treatments that increased Myosin II activity, we saw a loss of DE-cadherin from the four-way vertex during neighbour exchange, indicating that the flow of DE-cadherin to vertices is disrupted in this phenotype. Since DE-cadherin is required for junction remodelling, this could cause neighbour exchange events to be less permissible in the tissue. Interestingly we also observed discontinuities at vertices, as well as lower rates of neighbour exchange, in the *shibire* mutant line, where endocytosis of DE-cadherin is blocked [Curran 2015]. It has been shown that Myosin II is involved in supporting the integrity of DE-cadherin contacts [109], suggesting a possible mechanism that explains how increasing levels of Myosin II could inhibit junction remodelling. However, more work needs to be done to understand the interaction of the various molecular components involved.

I also examined neighbour exchange events in unperturbed nota later in development. At 25h AP, the frequency of neighbour exchange events is reduced and junction remodelling is less reversible. The correspondence between the notum late in development and the Rok CAT mutant phenotype at 12h AP suggests that the level of Myosin II in the tissue is indeed the key factor regulating neighbour exchange. It follows that the gradual increase in Myosin II during development could be functionally important for ordering in the tissue. Early in development, Myosin II levels are low, junction fluctuations are ubiquitous, and neighbour exchange events are frequent and reversible, allowing the tissue to explore a large set of possible configurations. As ordering proceeds and junctional Myosin II increases, neighbour exchange events are inhibited and cell-cell contacts eventually become locked in place.

This narrowing of the space of accesible configurations over time is reminiscent of simulated annealing, as described in section 2.3. Recall that simulated annealing is an algorithm for robustly finding the global minimum of an energy

function. It does so by gradually lowering the temperature or noise in the system. If the process of epithelial ordering can be cast as the minimization of some energy function, as in most existing models [64, 66, 70], our results directly propose that the tissue implements a form of simulated annealing to perform this minimization. Here the increase in junctional Myosin II is analogous to the reduction in temperature as it has the effect of restricting the configurations the system can access. The decrease in the probability of going through a neighbour exchange once at a four-way vertex corresponds to an increase in the energy barrier for that transition. This annealing schedule could be implemented in any of the equilibrum models described in section 2.3. We should note that epithelial tissues are in fact active systems, characterized turnover of junctional material and dissipation of energy, and as such the framework of energy minimization might not be applicable. In this case the equivalence with simulated annealing would not hold.

Irrespective of the modelling viewpoint, our results outline how the tissue transitions from a disordered to an ordered state. Stochastic junction fluctuations facilitate neighbour exchange events, but the primary regulation of these events occurs at four-way vertices. Myosin II both generates junction fluctuations and inhibits junction remodelling. We speculate that inhibition specifically at four-way vertices could allow the tissue to accomodate mechanical pertubations without disrupting tissue topology. How homeostatic tissues are able to respond to local pertubations while maintaining tissue integrity is an important question. Further work on the regulation of neighbour exchange in mature epithelia could determine whether vertex-specific inhibition is a more general mechanism for maintaining tissue integrity.

Chapter 9

Spatial correlations in the tissue

9.1 The effect of junction fluctuations does not spread beyond first neighbours

A somewhat separate aspect of tissue mechanics is how junction fluctuations are correlated between neighbouring junctions and how far such correlations spread in the tissue. Figure 9.1 shows that changes in the length of neighbouring junctions tend to be anti-correlated, whereas the correlation between junctions separated by one or more junctions averages to zero. The minimum of the mean crosscorrelation is at a lag of zero, indicating that there is no temporal delay in the force transmission between neighbouring junctions.

Another way to visualize how the effect of fluctuations spread, is to generate a spatial map of correlations in the tissue. For Figure 9.2, I calculated the cross-correlation between a single junction and every other junction in the tissue. This was then repeated for all junctions and the resulting spatial maps were aligned and averaged. The map shows how the crosscorrelation varies with distance and angle. In particular, the region corresponding to the typical position of 1st neighbour junctions is negatively correlated and beyond that correlations average to zero.

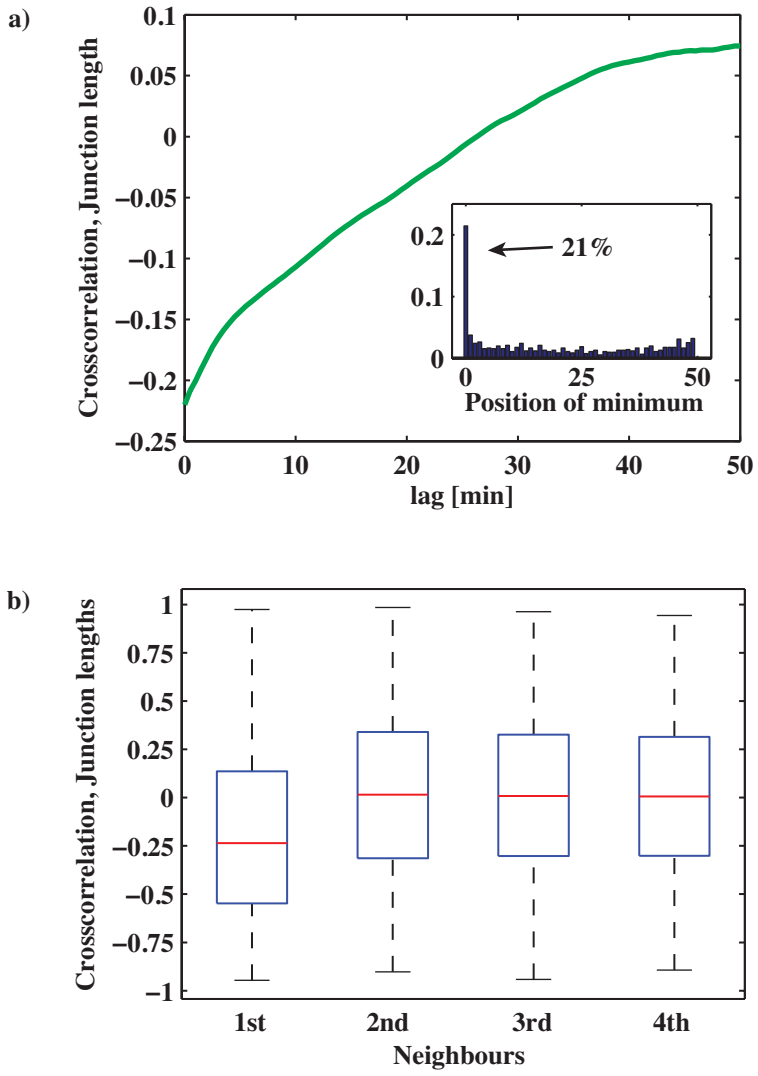

Figure 9.1: Crosscorrelation for neighbouring junctions

a) Crosscorrelation for the junction length time series of neighbouring junctions ($N = 1042$ junction pairings, 4 nota). The mean and standard error at zero lag is $= -0.22 \pm 0.0087$. **(inset)** Histogram of the lag time where the crosscorrelation function for individual junction pairs has its minimum ($N = 905$ pairings, 4 nota). Some junctions (137) are positively correlated and the crosscorrelation function decreases to reach its minimum value at the maximum lag. In this case it is not meaningful to talk about the minimum of the crosscorrelation function and the junction pairings are not included in the histogram.**b)** Boxplot of the crosscorrelation (at zero lag) for the junction lengths for 1st, 2nd, 3rd, and 4th neighbours.

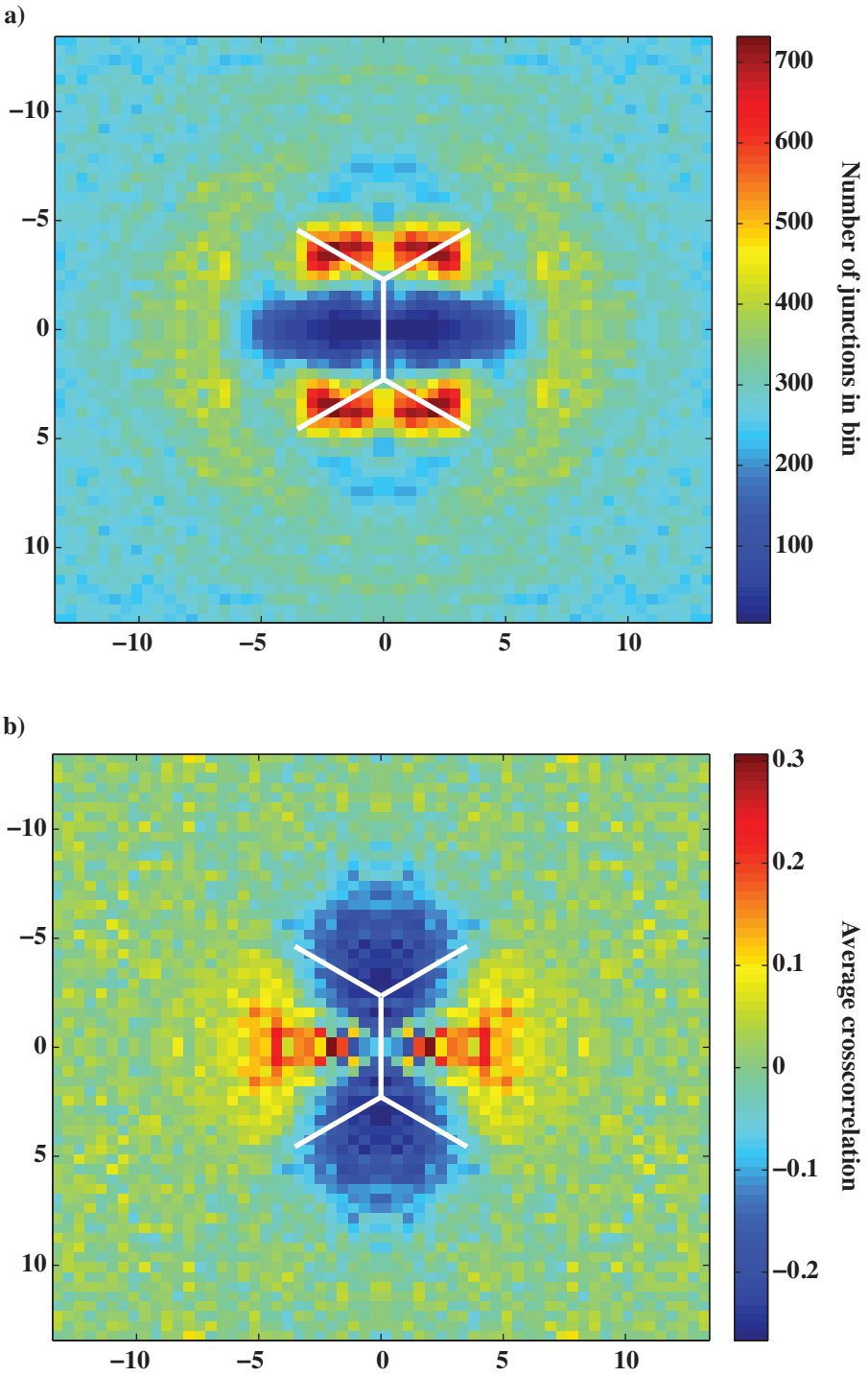

Figure 9.2: Crosscorrelations across the tissue

The figures contain data from time-lapse imaging of four wildtype pupae. **a)** The figure is generated by considering each pair of junctions in the tissue and determining the distance between their midpoints and their relative angle. This information is then used to generate a spatial map of the density of junction midpoints. The position of nearest neighbour junctions is restricted to a specific region, but beyond that there is very little structure in the distribution. Note that information about the absolute orientation of junctions is removed and it is only meaningful to consider relative angles between 0 and 90°. Hence the analysis generates a plot for the upper right quadrant with the junction midpoint in origo. For illustration purposes, this plot has been mirrored, to create the four-fold symmetry seen in the figure. A schematic of five junctions, of average length and with angles of 120° have added to the figure. **b)** Spatial map of cross-correlations in the tissue. The map is generated by calculating cross-correlations for each junction with every other junction in the tissue and binning this data according to relative angle and distance. The region of 1st neighbour junctions are anti-correlated, in accordance with the results in Figure 9.1, but correlations do not extend beyond this. The binsize is 5 pixels.

9.2 The angle-dependence of cross-correlations can be explained by a simple analytical model

Figure 9.2, suggests that the correlation between neighbouring junctions depends on angle. In particular, junctions are most strongly anti-correlated if they are close to being parallel and almost uncorrelated if they are perpendicular. We can develop a simple model to get some intuition for this angle-dependence. Start by considering a simple example of three junctions joined at a vertex (see figure 9.3). Say we are interested in the cross-correlation between the length of junction J_1 and J_2, and denote the inner angle between these junctions by α.

In $a)$, the junctions are almost parallel ($\alpha \sim 180^\circ$). Consequently, when the length of junction J_1 decreases by δ, the change in the length of junction J_2 is also of the order δ. By contrast, in $b)$, the junctions are perpendicular ($\alpha \sim 90^\circ$). In this case, there is no first order change in the length of J_2. for small δ,

$$\alpha \sim 180^\circ \quad \Rightarrow \quad \Delta J_2 \sim \delta \tag{9.1}$$

$$\alpha \sim 90^\circ \quad \Rightarrow \quad \Delta J_2 \sim 0 \tag{9.2}$$

If the change in length of J_1 and J_2 are of the same order of magnitude (but opposite sign), the junctions are strongly anti-correlated (cross-correlation is negative). From this 'geometric' argument we would therefore expect the cross-correlation to be zero at 90° and decrease monotonically with the angle α.

Now, let us construct an analytical model. With the arrangement of junctions in figure 9.3, consider the movement of the vertex joining junctions J_1 and J_2 and assume that the movement all other vertices is uncorrelated (such that contraction/expansion affects 1st neighbours only). We can find the new length $J_2^{'}$, after a length change δ in junction J_1, from the cosine rule.

$$J_2^{'} = \sqrt{J_2^2 + \delta^2 - 2J_2\delta\cos(\alpha)} \tag{9.3}$$

This is exact. The quantity we are interested in is the length change $J_2^{'} - J_2$. Since $\delta << J_2$, we can make a few simplifying approximations.

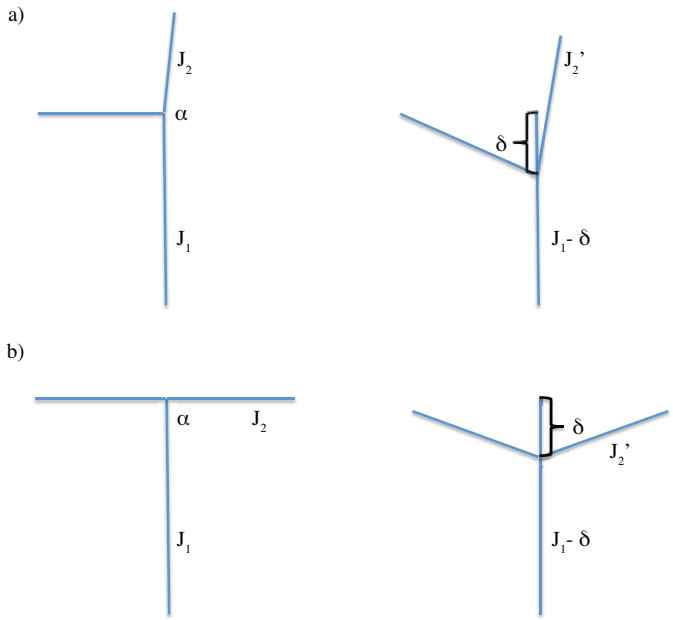

Figure 9.3: Schematic for crosscorrelation as a function of angle

Schematic of three junctions showing the configuration and notation used to develop the model. **a)** The junctions are almost parallel ($\alpha \sim 180°$). When the length of junction $J1$ decreases by δ, the vertex shared between junction $J1$ and $J2$ moves δ, and the change in the length of junction $J2$ is also of the order δ. **b)** The junctions are perpendicular ($\alpha \sim 90°$). In this case, there is no first order change in the length of J_2. for small δ.

$$
\begin{aligned}
J_2^{'} - J_2 &= \sqrt{J_2^2 + \delta^2 - 2J_2\delta\cos(\alpha)} - J_2 && (9.4)\\
&\cong \sqrt{J_2^2 - 2J_2\delta\cos(\alpha)} - J_2 && (9.5)\\
&= J_2\sqrt{1 - \frac{2\delta\cos(\alpha)}{J_2}} - J_2 && (9.6)\\
&\cong J_2(1 - \frac{\delta\cos(\alpha)}{J_2}) - J_2 && (9.7)\\
&= -\delta\cos(\alpha) && (9.8)
\end{aligned}
$$

A length-change $-\delta$ in junction J_1 thus corresponds to a change $-\delta\cos(\alpha)$ in junction J_2 (note that $cos(\alpha)$ is negative for $\alpha > 90$ degrees). As a result the unnormalized crosscorrelation (for lag zero) is given by:

$$R_{xy}(0) = \sum_t J_1(t) * J_2(t) = \cos(\alpha)\langle\delta(t)^2\rangle_t \qquad (9.9)$$

Using the assumption that the vertices at either end of a junction are moving

independently of each other (say by amounts δ and ϵ), the variance of a junction is given by:

$$\sigma^2 = \langle (J_1 - \langle J_1 \rangle)^2 \rangle = \langle \delta(t)^2 \rangle + \langle \epsilon(t)^2 \rangle = 2\langle \delta(t)^2 \rangle \tag{9.10}$$

Consequently, the crosscorrelation goes as $(\sigma^2/2)\cos(\alpha)$[1]. The junctions are anti-correlated for $\alpha > 90°$ and is zero when the junctions are perpendicular to each other. The model prediction of the angle-dependence of the cross-correlation is shown in Figure 9.3 alongside the experimental result. In addition, a fit to the data that includes a free parameter β is shown and this yields the function $3.26\cos(\alpha)$, which is in good agreement with the prediction from the parameter-free model.

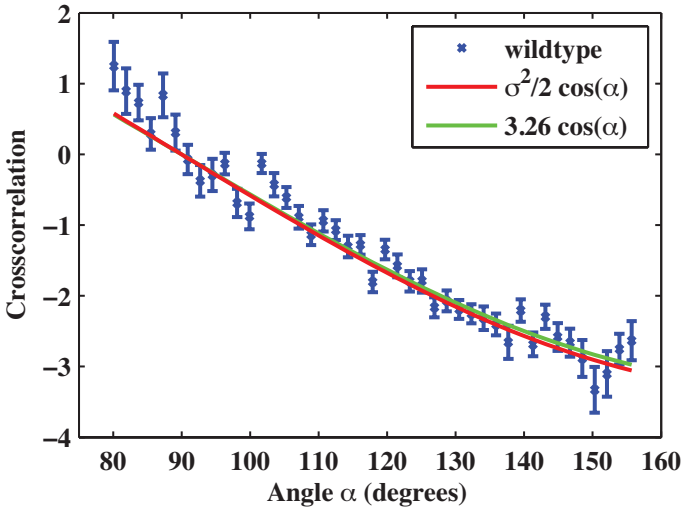

Figure 9.4: Crosscorrelation as a function of angle

(blue) Experimental data for the cross-correlation as a function of the angle between junctions. (red) The prediction from the analytical model, $(\sigma^2/2)\cos(\alpha)$. The experimentally measured variance for junction lengths is 6.70 μm^2. (green) Best fit using $\beta\cos(\alpha)$, where β is a free parameter. The same calculation for Rok RNAi and Rok CAT yields values for β of 3.87 and 3.61, respectively.

The key assumptions of the model are:

- Fluctuations are accommodated locally, i.e. the effect does not extend

[1]Note that including the uncorrelated movement of the second vertex would not change the calculation of the crosscorrelation since the change in junction J_1 would be $\delta + \delta$ for half the time points and $\delta - \delta$ for the other half.

beyond nearest-neighbour junctions. In particular, the movement of vertices connected by a junction is uncorrelated.

- Fluctuations in the position of vertices cause the total length of junctions to change. Even if most of this change comes from the exchange of length between junctions by the sliding of a shared vertex, the model would require that junctions have some degree of elasticity or that addition and removal of junctional material is able to accommodate length changes.

Chapter 10

Conclusion

In this thesis we set out to examine how order emerges in epithelial tissue during development in an effective and robust manner. Specifically, we wanted to investigate what heuristic the tissue implements to evolve from a disordered to an ordered state. I studied this using data from live imaging of the *Drosophila* notum - a tissue that develops hexagonal order without undergoing substantial growth or directed morphogenesis.

I developed a custom software package to process and analyse the live imaging data. The code is written using class-based object oriented programming with each junction and cell in the tissue stored as an object. In addition, the code tracks junctions and cells over time, assigning each a unique ID, and determines cell-cell connectivity within the tissue. The format makes it possible to query the properties of any junction or cell. The code made the analysis in this part of the thesis possible and will be of value for future projects in the lab.

I first characterized the properties of neighbour exchange events in the notum and showed that they differ in several ways from junction remodelling during germband elongation. In the notum, neighbour exchange events are often reversible, with the same junction undergoing several consecutive transitions. By contrast, junction remodelling during germband elongation is strictly irreversible. I then examined how neighbour exchange events in the notum can occur without causing large-scale deformation of the tissue, when such events drive morphogenesis in the embryonic germband. I found that, even though junction remodelling is associated with internal rearrangement and a resdistribution of apical area in the four cells involved, the aspect ratio of the four-cell cluster is unchanged. Hence, even if neighbour exchange events were oriented along the same axis, the cumulative effect would not reshape the tissue. I also studied the temporal

distribution of neighbour exchange events and found that they occur somewhat randomly in time. In particular, I could not decisively reject the hypothesis that the temporal distribution of events is consistent with a Poisson process. This suggests that neighbour exchange events in the notum are not highly coordinated and stereotyped processes, the way they are in germband elongation.

To investigate the hypothesis that neighbour exchange events are generated by a stochastic process in the tissue, I examined junction fluctuations and how they relate to neighbour exchange events. An analysis of the mean square displacement curve and the distribution of persistence lengths demonstrated that, on average, junction fluctuations are subdiffusive and resemble a constrained or mean-reverting random walk. We had anecdotal evidence that the magnitude of junction fluctuations are similar to the contraction and expansion observed during neighbour exchange. This was borne out by statistical analysis demonstrating that there is no difference in the persistence length of junction fluctuations and neighbour exchange events. Furthermore, I found no significant difference in the rate of contraction and expansion, going into and coming out of a four-way vertex configuration. Hence, phenomenologically junction remodelling in the notum is symmetric. The results suggest a model where neighbour exchange events are an epiphenomenon of stochastic fluctuations present in the tissue, rather than directed singular processes.

I then investigated how junction fluctuations originate and are regulated within the tissue. I used data from live imaging of transgenic *Drosophila* strains expressing Sqh-GFP to extract temporal information about Myosin II dynamics. From this analysis, I found that Myosin II intensity and junction lengths are anticorrelated, with changes in Myosin II preceeding changes in junction length by 35s. This suggests that Myosin II has a causal role in regulating junction fluctuations. To investigate this, I extended the mathematical model by Dierkes et al. [103] to incorporate stochastic turnover of myosin. This model was able to reproduce several features of Myosin II and junction dynamics, including the asymmetry in the anticorrelation and lagtime.

Having established a role for Myosin II both in generating and regulating junction fluctuations, I turned to how Myosin II affects neighbour exchange

events. For this, I used data from transgenic *Drosophila* strains with altered levels of Myosin II. I found that, across several mutant phenotypes, the frequency of neighbour exchange events scales inversely with the level of active Myosin II in the tissue. The effect was striking with neighbour exchange events being more than three times as frequent in Rok RNAi than in Rok CAT. In addition, changes in the level of Myosin II also affected the reversibility of neighbour exchange events. In Control at 12h AP, the probability that a cell neighbour configuration persists for longer than 150 min, following junction remodelling, is 69% and this drops to 26% in Rok RNAi. Notably, the results for both the frequency and reversibility of neighbour exchange events are opposite to what is reported in germband elongation, where a reduction in Myosin II activity is associated with a decrease in the frequency and overexpression of Myosin II increases reversibility [57].

To attempt to explain the observed differences in the frequency of neighbour exchange events across phenotypes, I quantified how frequently junctions reach a four-way vertex configuration, regardless of the eventual outcome. Interestingly, I found that the frequency is the same in Control 12h, Rok RNAi and Rok CAT. Consequently, the frequency of neigbhour exchange events can be explained by the likelihood of going through once at a four-way vertex. The molecular mechanism for such vertex-specific regulation is not known. However, we did observe that mutant phenotypes with increased Myosin activity displayed a loss of DE-cadherin from four-way vertices during neighbour exchange. In addition, we found that the frequency of neighbour exchange events is reduced in the *shibire* mutant line, where endocytosis of DE-cadherin is blocked [Curran 2015]. Since DE-cadherin is required for junction remodelling and Myosin II is known to affect the stability of DE-cadherin cell-cell contacts [109], this suggests a possible mechanism. However, more work is needed to determine the role of the various molecular components involved.

To investigate the role of neighbour exchange in ordering, I examined junction remodelling and junction fluctuations in unperturbed nota later in development. From 12h AP to 25h AP, the frequency of neighbour exchange events decreases by a factor 2.7 and events become less reversible. The observed correspondence

between the notum at 25h AP and the Rok CAT mutant phenotype at 12h AP demonstrates that Myosin II has a primary role in regulating neighbour exchange in the tissue.

Taken together, our results provide a heuristic for how the tissue transitions from a disordered to and ordered state during development. The data supports the hypothesis that the gradual developmental increase in Myosin II drives ordering in the tissue by generating junction fluctuations and regulating junction remodelling. Early in development, stochastic fluctuations of junctions allow the tissue to explore different configurations. They also facilitate neighbour exchange events, which are frequent and reversible at this stage. As the density of junctional Myosin II increases, junction remodelling is inhibited and cell-cell contacts are eventually locked in place.

Within the framework of equilibrium models this heuristic corresponds to a form of simulated annealing. Specifically, one where the annealing schedule involves an increase in the energy barrier at four-way vertices rather than a lowering of the temperature for the entire system.

We speculate that inhibition of junction remodelling specifically at four-way vertices could have advantages for the tissue. Such inhibition might enable the tissue to retain a certain degree of fluidity and responsivity to mechanical pertubations, while preventing changes in cell-cell connectivity. Further work is needed to address whether vertex-specific inhibition is a more general mechanism.

Bibliography

[1] S. Krens and C.-P. Heisenberg. "Cell sorting in development". In: *Curr Top Dev Biol* 95 (2011), pp. 189–213.

[2] D. A. Beysens, G Forgacs, and J. A. Glazier. "Cell sorting is analogous to phase ordering in fluids." In: *Proceedings of the National Academy of Sciences* 97.17 (Aug. 2000), pp. 9467–71.

[3] M Krieg, Y Arboleda-Estudillo, P.-H. Puech, J Käfer, F Graner, D. J. Müller, and C.-P. Heisenberg. "Tensile forces govern germ-layer organization in zebrafish." In: *Nature cell biology* 10.4 (Apr. 2008), pp. 429–36.

[4] P. L. Townes and J. Holtfreter. "Directed movements and selective adhesion of embryonic amphibian cells". In: *Journal of Experimental Zoology* 128.1 (1955), pp. 53–120. ISSN: 1097-010X. DOI: 10.1002/jez.1401280105.

[5] J. P. Rieu, N. Kataoka, and Y. Sawada. "Quantitative analysis of cell motion during sorting in two-dimensional aggregates of dissociated hydra cells". In: *Phys. Rev. E* 57 (1 1998), pp. 924–931.

[6] R. Foty, C. Pfleger, G. Forgacs, and M. Steinberg. "Surface tensions of embryonic tissues predict their mutual envelopment behavior". In: *Development* 122.5 (1996), pp. 1611–1620.

[7] R. A. Foty and M. S. Steinberg. "The differential adhesion hypothesis: a direct evaluation". In: *Developmental Biology* 278.1 (2005), pp. 255 –263. ISSN: 0012-1606. DOI: http://dx.doi.org/10.1016/j.ydbio.2004.11.012.

[8] E. Méhes, E. Mones, V. Németh, and T. Vicsek. "Collective Motion of Cells Mediates Segregation and Pattern Formation in Co-Cultures." In: *PloS one* 7.2 (Jan. 2012), e31711.

[9] R. A. Foty and M. S. Steinberg. "Cadherin-mediated cell-cell adhesion and tissue segregation in relation to malignancy." In: *The International journal of developmental biology* 48.5-6 (Jan. 2004), pp. 397–409.

[10] C. Strandkvist, J. Juul, B. Baum, A. J. Kabla, and T. Duke. "A kinetic mechanism for cell sorting based on local variations in cell motility". In: *Interface focus* 4.6 (2014), p. 20140013.

[11] A. V. Nielsen, A. L. Gade, J. Juul, and C. Strandkvist. "Schelling model of cell segregation based only on local information". In: *Physical Review E* 92.5 (2015), p. 052705.

[12] M. S. Steinberg. "On the mechanism of tissue reconstruction by dissociated cells, III. Free energy relations and the reorganization of fused, heteronomic tissue fragments". In: *Proceedings of the National Academy of Sciences* 48.10 (1962), pp. 1769–1776.

[13] M. S. Steinberg. "On the mechanism of tissue reconstruction by dissociated cells, I. Population kinetics, differential adhesiveness, and the absence of directed migration". In: *Proceedings of the National Academy of Sciences* 48.9 (1962), pp. 1577–1582.

[14] M. S. Steinberg. "Mechanism of Tissue Reconstruction by Dissociated Cells, II: Time-Course of Events". In: *Science* 137.3532 (1962), pp. 762–763. DOI: 10.1126/science.137.3532.762.

[15] M. S. Steinberg. "Reconstruction of Tissues by Dissociated Cells". In: *Science* 141.3579 (1963), pp. 401–408. DOI: 10.1126/science.141.3579.401.

[16] F. Graner and J. A. Glazier. "Simulation of biological cell sorting using a two-dimensional extended Potts model". In: *Phys. Rev. Lett.* 69.13 (1992), p. 2013.

[17] J. A. Glazier and F. Graner. "Simulation of the differential adhesion driven rearrangement of biological cells". In: *Phys. Rev. E* 47 (3 1993), pp. 2128–2154.

[18] J. C. M. Mombach, J. A. Glazier, R. C. Raphael, and M. Zajac. "Quantitative Comparison between Differential Adhesion Models and Cell Sorting in the Presence and Absence of Fluctuations". In: *Phys. Rev. Lett.* 75 (11 1995), pp. 2244–2247.

[19] A. F. Marée and P. Hogeweg. "How amoeboids self-organize into a fruiting body: multicellular coordination in Dictyostelium discoideum". In: *Proceedings of the National Academy of Sciences* 98.7 (2001), pp. 3879–3883.

[20] N. B. Ouchi, J. A. Glazier, J.-P. Rieu, A. Upadhyaya, and Y. Sawada. "Improving the realism of the cellular Potts model in simulations of biological cells". In: *Physica A: Statistical Mechanics and its Applications* 329.3-4 (Nov. 2003), pp. 451–458.

[21] Y. Zhang, G. L. Thomas, M. Swat, A. Shirinifard, and J. A. Glazier. "Computer simulations of cell sorting due to differential adhesion". In: *PloS one* 6.10 (2011), e24999.

[22] A. Nakajima and S. Ishihara. "Kinetics of the cellular Potts model revisited". In: *New Journal of Physics* 13.3 (Mar. 2011), p. 033035.

[23] E.-M. Schötz, R. D. Burdine, F. Jülicher, M. S. Steinberg, C.-P. Heisenberg, and R. A. Foty. "Quantitative differences in tissue surface tension influence zebrafish germ layer positioning". In: *HFSP journal* 2.1 (2008), pp. 42–56.

[24] A. Voss-Böhme. "Multi-scale modeling in morphogenesis: a critical analysis of the cellular Potts model". In: *PloS one* 7.9 (2012), e42852.

[25] J. Belmonte, G. Thomas, L. Brunnet, R. de Almeida, and H. Chaté. "Self-Propelled Particle Model for Cell-Sorting Phenomena". In: *Phys. Rev. Lett.* 100.24 (June 2008), pp. 20–23.

[26] C. P. Beatrici and L. G. Brunnet. "Cell sorting based on motility differences". In: *Physical Review E* 84.3 (Sept. 2011), pp. 1–5.

[27] S. R. Mccandlish, A. Baskaran, and M. F. Hagan. "Spontaneous Segregation of Self-Propelled Particles with Different Motilities". In: *Soft Matter* 8.c (2012), pp. 2527–2534.

[28] A. J. Kabla. "Collective cell migration: leadership, invasion and segregation". In: *Journal of The Royal Society Interface* 9.77 (2012), pp. 3268–3278.

[29] J. P. Rieu, A Upadhyaya, J. A. Glazier, N. B. Ouchi, and Y Sawada. "Diffusion and deformations of single hydra cells in cellular aggregates." In: *Biophysical journal* 79.4 (Oct. 2000), pp. 1903–14.

[30] A. Upadhyaya, J.-P. Rieu, J. A. Glazier, and Y. Sawada. "Anomalous diffusion and non-Gaussian velocity distribution of Hydra cells in cellular aggregates". In: *Physica A: Statistical Mechanics and its Applications* 293.3 (2001), pp. 549–558.

[31] L. Diambra, L. Cintra, Q. Chen, D. Schubert, and L. D. F. Costa. "Cell adhesion protein decreases cell motion: Statistical characterization of locomotion activity". In: *Physica A: Statistical Mechanics and its Applications* 365.2 (June 2006), pp. 481–490.

[32] T. C. Schelling. "Models of Segregation". English. In: *The American Economic Review* 59.2 (1969), pp. 488–493.

[33] T. C. Schelling. "Dynamic models of segregation?" In: *The Journal of Mathematical Sociology* 1.2 (1971), pp. 143–186.

[34] T. C. Schelling. "Micromotives and Macrobehavior". In: *Norton, New York* (1978).

[35] L. Gauvin, J. Vannimenus, and J.-P. Nadal. "Phase diagram of a Schelling segregation model". In: *The European Physical Journal B* 70.2 (July 2009), pp. 293–304. ISSN: 1434-6028.

[36] D. Vinkovic and A. Kirman. "A physical analogue of the Schelling model." In: *Proceedings of the National Academy of Sciences* 103.51 (Dec. 2006), pp. 19261–5. ISSN: 0027-8424.

[37] T. Rogers and A. J. McKane. "A unified framework for Schelling's model of segregation". In: *Journal of Statistical Mechanics: Theory and Experiment* 2011.07 (July 2011), P07006. DOI: 10.1088/1742-5468/2011/07/P07006.

[38] S. Grauwin, E. Bertin, R. Lemoy, and P. Jensen. "Competition between collective and individual dynamics". In: *Proceedings of the National Academy of Sciences* 106.49 (2009), pp. 20622–20626.

[39] L. Dall'Asta, C. Castellano, and M. Marsili. "Statistical physics of the Schelling model of segregation". In: *Journal of Statistical Mechanics: Theory and Experiment* 2008.07 (2008), p. L07002.

[40] D. Stauffer and S. Solomon. "Ising, Schelling and self-organising segregation". In: *The European Physical Journal B* 57.4 (2007), pp. 473–479.

[41] E. Méhes and T. Vicsek. "Segregation mechanisms of tissue cells: from experimental data to models". In: *Complex Adaptive Systems Modeling* 1.1 (2013), p. 4.

[42] D. Duguay, R. A. Foty, and M. S. Steinberg. "Cadherin-mediated cell adhesion and tissue segregation: qualitative and quantitative determinants". In: *Developmental biology* 253.2 (2003), pp. 309–323.

[43] J.-P. Rieu and Y. Sawada. "Hydrodynamics and cell motion during the rounding of two dimensional hydra cell aggregates". In: *The European Physical Journal B - Condensed Matter* 27.1 (May 2002), pp. 167–172.

[44] M. Sarris, J.-B. Masson, D. Maurin, L. M. Van der Aa, P. Boudinot, H. Lortat-Jacob, and P. Herbomel. "Inflammatory chemokines direct and restrict leukocyte migration within live tissues as glycan-bound gradients". In: *Current Biology* 22.24 (2012), pp. 2375–2382.

[45] R. Nagpal, A. Patel, and M. C. Gibson. "Epithelial topology". In: *BioEssays* 30.3 (2008), pp. 260–266.

[46] M. C. Gibson, A. B. Patel, R. Nagpal, and N. Perrimon. "The emergence of geometric order in proliferating metazoan epithelia". In: *Nature* 442.7106 (2006), pp. 1038–1041.

[47] A.-K. Classen, K. I. Anderson, E. Marois, and S. Eaton. "Hexagonal packing of *Drosophila* wing epithelial cells by the planar cell polarity pathway". In: *Developmental cell* 9.6 (2005), pp. 805–817.

[48] T. Hayashi and R. W. Carthew. "Surface mechanics mediate pattern formation in the developing retina". In: *Nature* 431.7009 (2004), pp. 647–652.

[49] M. Cohen, M. Georgiou, N. L. Stevenson, M. Miodownik, and B. Baum. "Dynamic filopodia transmit intermittent Delta-Notch signaling to drive pattern refinement during lateral inhibition". In: *Developmental cell* 19.1 (2010), pp. 78–89.

[50] M. Cohen, B. Baum, and M. Miodownik. "The importance of structured noise in the generation of self-organizing tissue patterns through contact-mediated cell–cell signalling". In: *Journal of The Royal Society Interface* 8.59 (2011), pp. 787–798.

[51] H. H. Chang, M. Hemberg, M. Barahona, D. E. Ingber, and S. Huang. "Transcriptome-wide noise controls lineage choice in mammalian progenitor cells". In: *Nature* 453.7194 (2008), pp. 544–547.

[52] S. L. Spencer, S. Gaudet, J. G. Albeck, J. M. Burke, and P. K. Sorger. "Non-genetic origins of cell-to-cell variability in TRAIL-induced apoptosis". In: *Nature* 459.7245 (2009), pp. 428–432.

[53] C. Bertet, L. Sulak, and T. Lecuit. "Myosin-dependent junction remodelling controls planar cell intercalation and axis elongation". In: *Nature* 429.6992 (2004), pp. 667–671.

[54] M. Rauzi, P.-F. Lenne, and T. Lecuit. "Planar polarized actomyosin contractile flows control epithelial junction remodelling". In: *Nature* 468.7327 (2010), pp. 1110–1114.

[55] R. Fernandez-Gonzalez, S. d. M. Simoes, J.-C. Röper, S. Eaton, and J. A. Zallen. "Myosin II dynamics are regulated by tension in intercalating cells". In: *Developmental cell* 17.5 (2009), pp. 736–743.

[56] M. Rauzi, P. Verant, T. Lecuit, and P.-F. Lenne. "Nature and anisotropy of cortical forces orienting *Drosophila* tissue morphogenesis". In: *Nature Cell Biology* 10.12 (2008), pp. 1401–1410.

[57] K. E. Kasza, D. L. Farrell, and J. A. Zallen. "Spatiotemporal control of epithelial remodeling by regulated myosin phosphorylation". In: *Proceedings of the National Academy of Sciences* 111.32 (2014), pp. 11732–11737.

[58] J. A. Zallen and R. Zallen. "Cell-pattern disordering during convergent extension in *Drosophila*". In: *Journal of Physics: Condensed Matter* 16.44 (2004), S5073.

[59] E. Batlle and D. G. Wilkinson. "Molecular mechanisms of cell segregation and boundary formation in development and tumorigenesis". In: *Cold Spring Harbor perspectives in biology* 4.1 (2012), a008227.

[60] G. Solanas and E. Batlle. "Control of cell adhesion and compartmentalization in the intestinal epithelium". In: *Experimental cell research* 317.19 (2011), pp. 2695–2701.

[61] D. W. Thompson et al. "On growth and form." In: *On growth and form.* (1942).

[62] D Weaire and N Rivier. "Soap, cells and statistics—random patterns in two dimensions". In: *Contemporary Physics* 25.1 (1984), pp. 59–99.

[63] S. T. Browne. "The Garden of Cyrus (1658)". In: *Browne, The Major Works, CA* ().

[64] J. Käfer, T. Hayashi, A. F. Marée, R. W. Carthew, and F. Graner. "Cell adhesion and cortex contractility determine cell patterning in the *Drosophila* retina". In: *Proceedings of the National Academy of Sciences* 104.47 (2007), pp. 18549–18554.

[65] A. Szabó and R. M. Merks. "Cellular potts modeling of tumor growth, tumor invasion, and tumor evolution". In: *Front Oncol* 3.87.10 (2013), p. 3389.

[66] R. Farhadifar, J.-C. Röper, B. Aigouy, S. Eaton, and F. Jülicher. "The influence of cell mechanics, cell-cell interactions, and proliferation on epithelial packing". In: *Current Biology* 17.24 (2007), pp. 2095–2104.

[67] L. Hufnagel, A. A. Teleman, H. Rouault, S. M. Cohen, and B. I. Shraiman. "On the mechanism of wing size determination in fly development". In: *Proceedings of the National Academy of Sciences* 104.10 (2007), pp. 3835–3840.

[68] H. Honda, T. Nagai, and M. Tanemura. "Two different mechanisms of planar cell intercalation leading to tissue elongation". In: *Developmental Dynamics* 237.7 (2008), pp. 1826–1836.

[69] P. Spahn and R. Reuter. "A vertex model of *Drosophila* ventral furrow formation". In: *PloS one* 8.9 (2013), e75051.

[70] S. Hilgenfeldt, S. Erisken, and R. W. Carthew. "Physical modeling of cell geometric order in an epithelial tissue". In: *Proceedings of the National Academy of Sciences* 105.3 (2008), pp. 907–911.

[71] A. G. Fletcher, M. Osterfield, R. E. Baker, and S. Y. Shvartsman. "Vertex models of epithelial morphogenesis". In: *Biophysical journal* 106.11 (2014), pp. 2291–2304.

[72] S. Kirkpatrick, M. P. Vecchi, et al. "Optimization by simmulated annealing". In: *science* 220.4598 (1983), pp. 671–680.

[73] M Locatelli. "Convergence of a simulated annealing algorithm for continuous global optimization". In: *Journal of Global Optimization* 18.3 (2000), pp. 219–233.

[74] S. Curran. "The changing role of junctional actomyosin in epithelial cell packing during *Drosophila* notum development". PhD thesis. UCL (University College London), 2015.

[75] J. Huang, W. Zhou, W. Dong, A. M. Watson, and Y. Hong. "Directed, efficient, and versatile modifications of the *Drosophila* genome by genomic engineering". In: *Proceedings of the National Academy of Sciences* 106.20 (2009), pp. 8284–8289.

[76] A. H. Brand and N. Perrimon. "Targeted gene expression as a means of altering cell fates and generating dominant phenotypes". In: *development* 118.2 (1993), pp. 401–415.

[77] S. d. M. Simões, J. T. Blankenship, O. Weitz, D. L. Farrell, M. Tamada, R. Fernandez-Gonzalez, and J. A. Zallen. "Rho-Kinase Directs Bazooka/Par-3 Planar Polarity during *Drosophila* Axis Elongation". In: *Developmental cell* 19.3 (2010), pp. 377–388.

[78] V. Verdier, J. Settleman, et al. "Rho-kinase regulates tissue morphogenesis via non-muscle myosin and LIM-kinase during *Drosophila* development". In: *BMC developmental biology* 6.1 (2006), p. 38.

[79] J. N. Dorsten, P. A. Kolodziej, and M. F. VanBerkum. "Frazzled regulation of myosin II activity in the *Drosophila* embryonic CNS". In: *Developmental biology* 308.1 (2007), pp. 120–132.

[80] C. Bertet, M. Rauzi, and T. Lecuit. "Repression of Wasp by JAK/STAT signalling inhibits medial actomyosin network assembly and apical cell constriction in intercalating epithelial cells". In: *Development* 136.24 (2009), pp. 4199–4212.

[81] B. Aigouy, R. Farhadifar, D. B. Staple, A. Sagner, J.-C. Röper, F. Jülicher, and S. Eaton. "Cell Flow Reorients the Axis of Planar Polarity in the Wing Epithelium of *Drosophila*". In: *Cell* 142.5 (2010), pp. 773–786.

[82] D. Sun, S. Roth, and M. J. Black. "Secrets of optical flow estimation and their principles". In: *Computer Vision and Pattern Recognition (CVPR), 2010 IEEE Conference on*. IEEE. 2010, pp. 2432–2439.

[83] F. Bosveld, I. Bonnet, B. Guirao, S. Tlili, Z. Wang, A. Petitalot, R. Marchand, P.-L. Bardet, P. Marcq, F. Graner, et al. "Mechanical control of morphogenesis by Fat/Dachsous/Four-jointed planar cell polarity pathway". In: *Science* 336.6082 (2012), pp. 724–727.

[84] A. Royou, C. Field, J. C. Sisson, W. Sullivan, and R. Karess. "Reassessing the role and dynamics of nonmuscle myosin II during furrow formation in early *Drosophila* embryos". In: *Molecular biology of the cell* 15.2 (2004), pp. 838–850.

[85] C. Guillot and T. Lecuit. "Mechanics of epithelial tissue homeostasis and morphogenesis". In: *Science* 340.6137 (2013), pp. 1185–1189.

[86] M. Takeichi. "Dynamic contacts: rearranging adherens junctions to drive epithelial remodelling". In: *Nature Reviews Molecular Cell Biology* 15.6 (2014), pp. 397–410.

[87] M. Cavey, M. Rauzi, P.-F. Lenne, and T. Lecuit. "A two-tiered mechanism for stabilization and immobilization of E-cadherin". In: *Nature* 453.7196 (2008), pp. 751–756.

[88] J. Solon, A. Kaya-Copur, J. Colombelli, and D. Brunner. "Pulsed forces timed by a ratchet-like mechanism drive directed tissue movement during dorsal closure". In: *Cell* 137.7 (2009), pp. 1331–1342.

[89] E. Marinari, A. Mehonic, S. Curran, J. Gale, T. Duke, and B. Baum. "Live-cell delamination counterbalances epithelial growth to limit tissue overcrowding." In: *Nature* 484.7395 (Apr. 2012), pp. 542–5.

[90] J. T. Rich, J. G. Neely, R. C. Paniello, C. C. Voelker, B. Nussenbaum, and E. W. Wang. "A practical guide to understanding Kaplan-Meier curves". In: *Otolaryngology-Head and Neck Surgery* 143.3 (2010), pp. 331–336.

[91] R. Levayer, A. Pelissier-Monier, and T. Lecuit. "Spatial regulation of Dia and Myosin-II by RhoGEF2 controls initiation of E-cadherin endocytosis during epithelial morphogenesis". In: *Nature cell biology* 13.5 (2011), pp. 529–540.

[92] L. C. Butler, G. B. Blanchard, A. J. Kabla, N. J. Lawrence, D. P. Welchman, L Mahadevan, R. J. Adams, and B. Sanson. "Cell shape changes indicate a role for extrinsic tensile forces in *Drosophila* germ-band extension". In: *Nature Cell Biology* 11.7 (2009), pp. 859–864.

[93] E. A. Codling, M. J. Plank, and S. Benhamou. "Random walk models in biology". In: *Journal of the Royal Society Interface* 5.25 (2008), pp. 813–834.

[94] G. Weiss. *Aspects and Applications of the Random Walk, 1994*.

[95] X. Michalet. "Mean square displacement analysis of single-particle trajectories with localization error: Brownian motion in an isotropic medium". In: *Physical Review E* 82.4 (2010), p. 041914.

[96] X. Michalet and A. J. Berglund. "Optimal diffusion coefficient estimation in single-particle tracking". In: *Physical Review E* 85.6 (2012), p. 061916.

[97] M. F. Serag, M. Abadi, and S. Habuchi. "Single-molecule diffusion and conformational dynamics by spatial integration of temporal fluctuations". In: *Nature communications* 5 (2014).

[98] E. D. Protonotarios, B. Baum, A. Johnston, G. L. Hunter, and L. D. Griffin. "An absolute interval scale of order for point patterns". In: *Journal of The Royal Society Interface* 11.99 (2014), p. 20140342.

[99] D. Furman and T. Bukharina. "Morphogenesis of *Drosophila* melanogaster macrochaetes: cell fate determination for bristle organ". In: *Journal of stem cells* 7.1 (2012), p. 19.

[100] K. Usui and K.-i. Kimura. "Sequential emergence of the evenly spaced microchaetes on the notum of *Drosophila*". In: *Roux's archives of developmental biology* 203.3 (1993), pp. 151–158.

[101] F. T. Lewis. "The effect of cell division on the shape and size of hexagonal cells". In: *The Anatomical Record* 33.5 (1926), pp. 331–355.

[102] F. T. Lewis. "The correlation between cell division and the shapes and sizes of prismatic cells in the epidermis of Cucumis". In: *The anatomical record* 38.3 (1928), pp. 341–376.

[103] K. Dierkes, A. Sumi, J. Solon, and G. Salbreux. "Spontaneous oscillations of elastic contractile materials with turnover". In: *Physical review letters* 113.14 (2014), p. 148102.

[104] C. Collinet, M. Rauzi, P.-F. Lenne, and T. Lecuit. "Local and tissue-scale forces drive oriented junction growth during tissue extension". In: *Nature cell biology* (2015).

[105] D. P. Kiehart, C. G. Galbraith, K. A. Edwards, W. L. Rickoll, and R. A. Montague. "Multiple forces contribute to cell sheet morphogenesis for dorsal closure in *Drosophila*". In: *The Journal of cell biology* 149.2 (2000), pp. 471–490.

[106] M. Mak, M. H. Zaman, R. D. Kamm, and T. Kim. "Interplay of active processes modulates tension and drives phase transition in self-renewing, motor-driven cytoskeletal networks". In: *Nature communications* 7 (2016).

[107] B. Chen and H. Gao. "Motor force homeostasis in skeletal muscle contraction". In: *Biophysical journal* 101.2 (2011), pp. 396–403.

[108] R. McGill, J. W. Tukey, and W. A. Larsen. "Variations of box plots". In: *The American Statistician* 32.1 (1978), pp. 12–16.

[109] M. Smutny, H. L. Cox, J. M. Leerberg, E. M. Kovacs, M. A. Conti, C. Ferguson, N. A. Hamilton, R. G. Parton, R. S. Adelstein, A. S. Yap, et al. "Myosin II isoforms identify distinct functional modules that support integrity of the epithelial zonula adherens". In: *Nature cell biology* 12.7 (2010), pp. 696–702.